CONFIDENTIAL





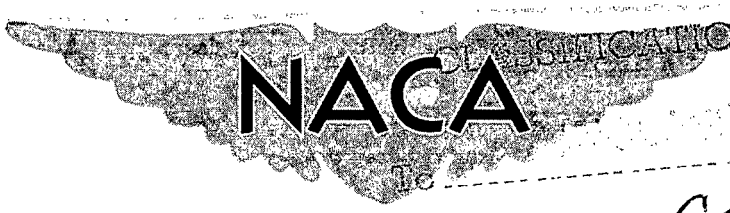




# RESEARCH MEMORANDUM

for the

U. S. Air Force

## A TRANSONIC WIND-TUNNEL INVESTIGATION OF THE STATIC LATERAL, DIRECTIONAL, AND LONGITUDINAL STABILITY CHARACTERISTICS OF THE MARTIN B-61A MISSILE (MATADOR)

By Arvo A. Luoma

Langley Aeronautical Laboratory
Langley Field, Va.



NATIONAL ADVISORY COMMITTEE
FOR AERONAUTICS
WASHINGTON

CONFIDENTIAL

NACA RM SL54D07

NATIONAL ADVISORY COMMITTEE FOR AERONAUTICS



RESEARCH MEMORANDUM



# A TRANSONIC WIND-TUNNEL INVESTIGATION OF THE STATIC LATERAL, DIRECTIONAL, AND LONGITUDINAL STABILITY CHARACTERISTICS OF THE MARTIN B-61A MISSILE (MATADOR)

By Arvo A. Luoma

## SUMMARY

The static lateral, directional, and longitudinal stability characteristics of a 0.06-scale model of the Martin B-61A missile (Matador) were investigated in the Langley 8-foot transonic tunnel at Mach numbers from 0.80 to 1.12. Six-component force and moment data were obtained from strain-gage measurements. The characteristics of a spoiler and of wing-tip end plates were also investigated. The Reynolds number of the tests based on the mean aerodynamic chord of the wing was approximately $1.6 \times 10^6$.

The longitudinal and directional stability appeared satisfactory, except for a loss in directional stability near sonic velocity at small angles of yaw. Spoiler power appeared adequate. End plates were ineffective in reducing the dihedral effect at Mach numbers near 0.96 but were effective at the other Mach numbers. At such Mach numbers, the effectiveness was approximately proportional to the area of the plates. Langley and Wright Air Development Center results on this model showed good agreement for the most part.

## INTRODUCTION

A wind-tunnel investigation of a 0.06-scale model of the operational production configuration of the Martin B-61A missile (Matador) was made at the Wright Air Development Center, Wright-Patterson Air Force Base, Ohio, and is reported in reference 1. The tests, however,

did not include the part of the Mach number range from 0.97 to 1.08 in which the missile will fly. At the time of the investigation of reference 1, flight tests had been made of the developmental configurations but none had been made of the operational production configuration.

At the request of the U. S. Air Force, an investigation was therefore made in the Langley 8-foot transonic tunnel to provide additional information at transonic speeds on the static lateral, directional, and longitudinal stability characteristics of the 0.06-scale model of the operational production configuration of the Martin B-61A missile (Matador). The lateral control characteristics of a spoiler, the effect of wing-tip end plates on the effective dihedral of the complete model, and the variation with Mach number of the static pressure at several orifices on the fuselage and on a static tube located ahead of the fuselage nose were also investigated.

## SYMBOLS

The aerodynamic force and moment data are referred to the stability axes, which are shown in figure 1. The origin of the stability axes for the present tests was the center-of-gravity location shown in figure 2. The symbols used in this paper are defined as follows:

Aerodynamic

| | |
|---|---|
| $b$ | span of wing [1] |
| $C_D$ | drag coefficient, $D/qS$ |
| $C_{D_{min}}$ | minimum drag coefficient |
| $\Delta C_D$ | rise in drag coefficient above minimum value, $C_D - C_{D_{min}}$ |
| $C_L$ | lift coefficient, $L/qS$ |
| $C_{L_{C_{D_{min}}}}$ | lift coefficient corresponding to minimum drag coefficient |
| $\Delta C_L$ | change in lift coefficient from value corresponding to minimum drag coefficient, $C_L - C_{L_{C_{D_{min}}}}$ |
| $\frac{\Delta C_D}{(\Delta C_L)^2}$ | drag-rise factor |

| | |
|---|---|
| $(\Delta C_L)_s$, $(\Delta C_D)_s$, $(\Delta C_m)_s$, $(\Delta C_n)_s$, $(\Delta C_l)_s$, $(\Delta C_Y)_s$ | incremental coefficients due to spoiler deflection |
| $C_{L_\alpha}$ | derivative of lift coefficient with respect to angle of attack, $\frac{dC_L}{d\alpha}$ |
| $C_X$ | longitudinal-force coefficient, $X/qS$ |
| $C_Y$ | lateral-force coefficient, $Y/qS$ |
| $C_{Y_\psi}$ | derivative of lateral-force coefficient with respect to angle of yaw, $\frac{dC_Y}{d\psi}$ |
| $C_l$ | rolling-moment coefficient, $L'/qSb$ |
| $C_{l_\psi}$ | derivative of rolling-moment coefficient with respect to angle of yaw, $\frac{dC_l}{d\psi}$ |
| $C_m$ | pitching-moment coefficient, $M'/qS\bar{c}$ |
| $C_{m_{C_L}}$ | derivative of pitching-moment coefficient with respect to lift coefficient, $\frac{dC_m}{dC_L}$ |
| $C_n$ | yawing-moment coefficient, $N'/qSb$ |
| $C_{n_\psi}$ | derivative of yawing-moment coefficient with respect to angle of yaw, $\frac{dC_n}{d\psi}$ |
| $c$ | local chord of wing, measured parallel to plane of symmetry of model |
| $\bar{c}$ | mean aerodynamic chord of wing $W^1$ |
| $\bar{c}'$ | mean aerodynamic chord of wing $W^{1A}$ |
| $c_t$ | tip chord of wing |

| | |
|---|---|
| $D$ | drag, $D = -X$ when $\psi = 0^\circ$ ($C_D$ data presented herein only for $\psi = 0^\circ$) |
| $h$ | height of end plates for wing tips, measured from chord line of tip section (see fig. 3) |
| $i_t$ | incidence of horizontal tail, measured by angle between root chord of horizontal tail and center line of body |
| $L$ | lift, $L = -Z$ |
| $L'$ | rolling moment about X-axis |
| $(L/D)_{max}$ | maximum value of lift-drag ratio |
| $M$ | Mach number in undisturbed stream |
| $M'$ | pitching moment about Y-axis |
| $N'$ | yawing moment about Z-axis |
| $P$ | pressure coefficient, $\frac{p_l - p}{q}$ |
| $p$ | static pressure in undisturbed stream |
| $p_l$ | local value of static pressure on surface of model |
| $q$ | dynamic pressure in undisturbed stream |
| $R$ | Reynolds number based on $\bar{c}$ |
| $S$ | projected area of wing $W^1$ (including portion within fuselage) on plane passing through root chord of wing and perpendicular to plane of symmetry of model |
| $S_e$ | lateral area of two end plates for wing tips, $2c_t h$ |
| $X$ | longitudinal force along X-axis, $D = -X$ when $\psi = 0^\circ$ |
| $Y$ | lateral force along Y-axis |
| $Z$ | force along Z-axis, $L = -Z$ |

| | |
|---|---|
| $\alpha$ | angle of attack of model, based on center line of body |
| $\psi$ | angle of yaw |

Configuration Notation

| | |
|---|---|
| $N^1$ | ogival nose |
| $N^3$ | ogival nose and static tube ($N^1$ plus static tube) |
| $B^1$ | center body and tail cone |
| $B^2$ | center body, tail cone, and radar housing ($B^1$ plus radar housing) |
| $B^3$ | center body, tail cone, radar housing, and control-cable housing ($B^2$ plus control-cable housing) |
| $W^1$ | wing with $-5^\circ$ of dihedral and rounded tips (tips formed by rotating airfoil section at tip about tip chord) |
| $W^{1A}$ | wing with $-5^\circ$ of dihedral and with rounded tips cut off |
| V | vertical tail |
| $H_o{}^1$ | horizontal tail with $15^\circ$ of dihedral and $i_t = 0^\circ$ |
| $S^1$ | production spoiler |
| $E^1$ | small end plates for wing tips |
| $E^2$ | large end plates for wing tips |
| $N^1B^3W^{1A}H_o{}^1V$ | combination designated in this paper as the "complete model" |

## APPARATUS AND METHODS

### Tunnel

The tests were made in the Langley 8-foot transonic tunnel. This tunnel operates at a stagnation pressure approximately equal to atmospheric pressure. The tunnel throat is of dodecagonal cross section with axial slots located at the vertices of the twelve wall panels. The

slotted design permits model testing at speeds through sonic velocity. Information on the design of this slotted tunnel is given in reference 2 and on the calibration of the flow in reference 3.

## Model, Sting, and Balance

Model.- The 0.06-scale model of the Martin B-61A missile (Matador) investigated in the Langley 8-foot transonic tunnel was the same model used in the WADC 10-foot wind-tunnel tests of reference 1. The Matador is a turbojet-powered missile with a submerged-type air inlet on the bottom of the fuselage. No provision was made on the model for internal flow, and the fuselage cross sections on the missile in the region of the air inlet were replaced on the model by plain circular cross sections. The complete configuration tested in the Langley tunnel is shown in figure 2 and included a wing with cut-off tips ($W^{1A}$), a radar housing, and a control-cable housing. Most of the WADC tests were made with the original version of the wing, which had rounded tips ($W^{1}$), and without the radar housing and the control-cable housing on the model.

The geometric characteristics of the model, including the wing with rounded tips ($W^{1}$) and the wing with the rounded tips cut off ($W^{1A}$), are given in table I. The model was constructed of steel except for the fuselage nose piece, which was of aluminum alloy.

The dimensions and location of two sizes of wing-tip end plates are shown in figure 3. The ratios of end-plate area to wing area $S_e/S$ were 0.053 and 0.106. The details of construction and the location of a simulated production spoiler are shown in figure 4. The spoiler height was $0.077\bar{c}$ and the spoiler span extended from $0.24\frac{b}{2}$ to $0.67\frac{b}{2}$. Figure 5 shows the dimensions of a static tube, which was attached to the fuselage nose, and the locations on the static tube and on the fuselage of static-pressure orifices at which data were obtained in the present tests.

Sting.- The section of the model sting rearward of the fuselage was of constant diameter, with a ratio of sting diameter to fuselage-base diameter of 0.82 (fig. 2); this sting diameter was the same as that used in the tests of reference 1. The extent of the constant-diameter section behind the fuselage was 6.7 fuselage-base diameters in the present tests and 2.0 fuselage-base diameters in the tests of reference 1. At the end of the constant-diameter section, the stings were enlarged in a conical taper, with semiangle values of 5.5° in the present tests and 3.0° in those of reference 1.

Balance.- A six-component strain-gage balance available at the Langley Laboratory was adapted to the Martin model. The balance was

positioned in the fuselage so that the moment center of the balance was on the center line of the fuselage and 5.36 inches rearward of the center-of-gravity location designated in figure 2. A closer location of the moment center of this balance to the center-of-gravity location was not possible without considerable and undesirable modification of the fuselage.

## Test Procedure

The model was tested in pitch and yaw. In the present investigation, only a horizontal-tail incidence $i_t$ of $0^\circ$ was tested; pitch data at other horizontal-tail incidences may be found in reference 1.

Model setup in tunnel for pitch and yaw tests.- The pitch tests were made with the model horizontal in the tunnel (fig. 6(a)), and the angle of attack of the model was varied by pivoting the sting in a vertical plane. The pivot axis of the sting was located approximately 79 inches downstream of the quarter-chord point of the mean aerodynamic chord of the wing. The yaw tests were made with the model vertical (model rotated $90^\circ$ about fuselage center line from horizontal position in pitch tests) in the tunnel (fig. 6(b)), and the angle of yaw was varied by pivoting the sting in the same vertical plane as in the pitch tests.

In the pitch tests and in all the yaw tests except those of the complete model, the center line of the model at angles of attack and yaw of $0^\circ$ was displaced approximately 4 inches below the center line of the tunnel. In the yaw tests of the complete model, the center line of the model at angles of yaw and attack of $0^\circ$ coincided with that of the tunnel.

Determination of angles of attack and yaw.- The no-load angle of attack in the pitch tests (or the no-load angle of yaw in the yaw tests) was obtained with a pendulum-type accelerometer, which was calibrated against inclination (in a vertical plane). The accelerometer was housed in the extension of the model sting and was located approximately 60 inches downstream of the quarter-chord point of the mean aerodynamic chord of the wing. Flexibility of the balance, model sting, and sting extension between the model and the accelerometer location required a correction to the accelerometer reading to obtain the model angle of attack in the pitch tests (or the model angle of yaw in the yaw tests). The angle of yaw in the pitch tests was $0^\circ$. Angles of attack of $0^\circ$ and $2^\circ$ (no-load values) were included in the yaw tests, and these values were obtained by the use of couplings of $0^\circ$ and $2^\circ$ at the rearward end of the model sting. Deflection of the balance and sting support system under aerodynamic load also necessitated corrections to the angle of attack in the yaw tests.

Force and moment tests.- Lift, longitudinal force, pitching moment, rolling moment, yawing moment, and lateral force were determined from strain-gage readings. The Mach number range was from 0.80 to approximately 1.12. The average Reynolds number (based on the mean aerodynamic chord of wing $W^1$) of the present investigation is shown plotted against Mach number in figure 7. At a given Mach number, the model was pivoted through either the angle-of-attack range or the angle-of-yaw range.

The configurations tested and the angles of attack, angles of yaw, and Mach numbers at which data were taken are given in table II. The configuration with the wing-tip end plates was tested in yaw in an attempt to reduce the effective dihedral of the complete model. The spoiler was tested on the upper surface of the left semispan of the wing. All the tests except one were made with the model in the smooth condition. Surface-roughness tests were made, in addition to the model-smooth tests, on the complete configuration through the angle-of-yaw range at an angle of attack of $-0.1^\circ$. For the roughness tests, 1/8-inch-wide strips of No. 60 carborundum grains were shellacked on the upper and lower surfaces of the wing and the horizontal tail at 10 percent chord and on the fuselage at 10 percent length.

The static pressure on the upper and lower surfaces of the sting at the base of the fuselage was measured for all test conditions.

Static-pressure measurements and schlieren studies.- Static-pressure measurements were made at various orifices on the static tube and on the fuselage of the wing—fuselage—static-tube configuration $N^3B^2W^1A$. In the pressure tests, the center line of the model at an angle of attack of $0^\circ$ coincided with that of the tunnel. The pressure data were obtained at angles of attack of $-1^\circ$, $0^\circ$, and $1^\circ$ and at Mach numbers from 0.90 to 1.12. No force and moment data were taken during these pressure tests. Additional static-pressure data at other orifice locations on the fuselage can be found in reference 1.

Schlieren photographs of the flow field in the region of the nose and base of the model were taken when shock phenomena were evident.

## ACCURACY

### Base-Pressure Correction

The axial force of the model was adjusted for the difference between the actual static pressure at the base of the fuselage and that in the undisturbed stream, so that the data presented herein correspond to a static pressure at the base of the fuselage equal to that of the undisturbed stream.

## Tunnel-Boundary Interference

Subsonic Mach numbers.- At subsonic Mach numbers, the interference effects of a tunnel boundary on the flow over a model in the test region near the center line of the tunnel have been made negligible by means of a slotted test section (ref. 3).

Supersonic Mach numbers.- At supersonic Mach numbers, reflections from the tunnel boundary of compression and expansion disturbances originating at the model impinge on the model and produce an interference of the flow over the model. With increases in Mach number, the reflected disturbances generally increase in intensity and are swept downstream, and at sufficiently high Mach numbers the disturbances clear the model. When the disturbances have cleared the model, the flow over the model is then free of tunnel-boundary interference. The effect of the boundary-reflected disturbances on the overall forces and moments of a fuselage-alone configuration and of a wing-fuselage configuration was generally of small practical significance (refs. 3 and 4), even though the effect of the boundary interference was conspicuous on model pressure distributions (ref. 3). The model of the present investigation may have been more susceptible to the effects of reflected disturbances than those of references 3 and 4 because of a blunter fuselage-nose angle and the inclusion of tail surfaces.

In the present tests, the schlieren photographs indicated that the flow over the model was free of boundary interference at a Mach number of 1.12 for all test angles of attack and yaw, and at a Mach number of 1.10 probably for angles of attack and yaw near $0^{\circ}$. At higher angles of attack and yaw at a Mach number of 1.10, however, the flow over the tail portion of the model appeared to have been affected by the reflected shock from the fuselage nose, although the force and moment data for these conditions showed no irregularities and were generally consistent with the WADC results of reference 1. All the data of the present investigation at a Mach number of 1.10 are included herein. Also presented herein are test data at Mach numbers of 1.02, 1.03, and 1.04, which were in the range of Mach numbers where the model was subject to tunnel-boundary interference. The intensity of the boundary-reflected disturbances at Mach numbers less than approximately 1.03 has been found to be weak, so that the effect of boundary interference on the data of the present tests at a Mach number of 1.02 was probably small. The influence of boundary interference on the data shown herein at Mach numbers of 1.03 and 1.04 has not been established, but it is believed that, even though the magnitudes and slopes may have been modified by boundary interference, the general trends shown by the data in this Mach number region are correct. No data are presented herein between Mach numbers of 1.04 and 1.10, where the effects of boundary interference may be large.

Corrections for tunnel-boundary interferences.- No corrections have been made to the data presented herein for the effects of tunnel-boundary interference.

## Sting-Interference Corrections

No sting-interference corrections have been determined for the configurations of the present tests, and the results are therefore presented uncorrected. In the investigation of reference 1, tests were made with two stings of smaller diameter; the ratios of these diameters to the fuselage-base diameter were 0.72 and 0.61. The effect of the reduction in sting diameter in the tests of reference 1 was found to have been generally negligible on lift, drag, and pitching moment. Recently published summary information on sting interference (ref. 5), however, indicates that the minimum diameter of the stings used in the tests of reference 1 may have been too large and that the length of the constant-diameter portion of the sting may have been too short to conclude that sting interference in the present tests was negligible.

## Precision of Data

The accuracy of the angle of attack in the pitch tests and the angle of yaw in the yaw tests was approximately $\pm 0.1^{\circ}$. Because of looseness in a horizontal plane of the pivot of the sting arm, however, the accuracy of the angle of yaw in the pitch tests and the angle of attack in the yaw tests was poorer and was approximately $\pm 0.2^{\circ}$.

An indication of the accuracy of the aerodynamic coefficients may be obtained from the repeatability and scatter of the test points.

The average stream Mach number in the model test region was accurate within $\pm 0.005$. Local deviations from the average stream Mach number in the model test region (tunnel empty) generally increased with Mach number and were as large as 0.01 at supersonic speeds (ref. 3). The accuracy of the model pressure coefficients was approximately $\pm 0.005$ at subsonic speeds and decreased at supersonic speeds to approximately $\pm 0.015$ at the highest supersonic speeds.

# RESULTS AND DISCUSSION

## Computation of Coefficients

The present tests were made by using the wing with the rounded tips cut off (wing $W^{1A}$); whereas most of the WADC tests of reference 1 were made by using the wing with rounded tips (wing $W^{1}$). A few tests in the

WADC investigation were made with wing $W^{1A}$, and it was found that the change in tip shape had negligible effect on lift, drag, and pitching-moment coefficients. To conform to the results of reference 1, the aerodynamic coefficients presented herein were based on the plan-form dimensions of wing $W^{1}$, and the aerodynamic moment coefficients were referred to the 25-percent point of the mean aerodynamic chord of this wing. The center-of-gravity location coicident with the 25-percent point of the mean aerodynamic chord of wing $W^{1}$ is shown in figure 2; this center-of-gravity location corresponded to the 25.6-percent point of the mean aerodynamic chord of wing $W^{1A}$.

The yaw data presented herein are given in terms of the angle of yaw $\psi$ to conform to the presentation of reference 1, even though the angle of sideslip $\beta$ is currently the preferred angle designation for yaw tests at the Langley Laboratory.

## Basic and Summary Force and Moment Data

Presentation of data.- The basic force and moment data for the various configurations are presented in figures 8 to 17, inclusive. An index of these figures is presented in table II. Summary plots derived from the basic force and moment data are shown in figures 18 to 30, inclusive. In addition, comparisons are made in many of the summary plots between the results of the present tests and the WADC results given in reference 1. The Reynolds number of the WADC data shown herein was $1.66 \times 10^{6}$.

WADC and Langley configurations.- The WADC and Langley configurations for which comparisons are made were not identical, but the differences were essentially minor. In addition to the difference in wing tip (discussed in "Computation of Coefficients"), the complete configuration of the present tests also included radar and control-cable housings (see fig. 2) which were not included on the WADC configuration used for comparison. At a model angle of attack of approximately $0^{\circ}$, the radar housing was shown in reference 1 to have had negligible effect on pitching moment and increased the drag coefficient by less than 0.001. The sting supports used in the two investigations were also somewhat different (see "Apparatus and Methods" section), so that the support interference may have been different.

## Lift Characteristics

Figure 18 presents lift-curve-slope data for the various configurations. Where the curves of lift against angle of attack were nonlinear, the slopes shown are the average values for angles of attack from $-1^{\circ}$

to 1°. The lift-curve slopes obtained in the WADC investigation were generally 4 to 8 percent greater for the various configurations investigated than those obtained in the Langley investigation. The reason for the differences is not evident. As mentioned previously in "Computation of Coefficients," the effect of the wing-tip modification on lift was negligible. The radar and control-cable housings had negligible effect on lift coefficient at an angle of attack of 0° (figs. 12 and 14). The Reynolds numbers in the two investigations were essentially the same.

The maximum value of lift-curve slope occurred at a Mach number somewhat greater than 0.90 for the various configurations (fig. 18). The spoiler had generally small effect on the magnitude and variation with Mach number of the lift-curve slope of the complete model at an angle of attack of approximately 0° (fig. 18). With increase in angle of attack, the lift-curve slope of the complete model generally decreased (fig. 11(a)), whereas that of the spoiler configuration generally increased (fig. 17(a)).

## Pitching-Moment Characteristics

The variation with Mach number of the static longitudinal-stability derivative $C_{m_{C_L}}$ for the various configurations is presented in figure 19; the slopes shown are the average values for lift coefficients from -0.1 to 0.1. The derivative $C_{m_{C_L}}$ as obtained from the Langley and WADC tests showed good agreement for all the configurations investigated. The usual rearward movement of the aerodynamic center with increase in Mach number at subsonic speeds was shown by the data. The complete model less tail became longitudinally stable at Mach numbers greater than 0.89 (fig. 19). The results of reference 1 showed that the spoiler had small effect on the longitudinal-stability derivative of the complete model less tail. The main effect of the spoiler on the longitudinal-stability derivative of the complete model occurred at high subsonic Mach numbers, where the spoiler somewhat reduced the rearward movement of the aerodynamic center of the complete model (fig. 19); this effect was probably associated with a modification of the downwash by the spoiler.

No pitch-up difficulties were evident in the variation of pitching-moment coefficient with lift coefficient for lift coefficients up to the maximum test value of approximately 0.6 for the complete model (fig. 11) and for the complete model plus spoiler (fig. 17).

The pitching-moment coefficient was essentially insensitive to change in angle of yaw for all configurations tested in yaw (figs. 8(b), 9(b), 10(b), 12(b), 13(b), 14(b), and 15(b)).

## Drag Characteristics

The zero-lift drag of the various configurations obtained from the Langley and WADC tests agreed well for the most part (fig. 20). The drag force-break Mach number was approximately 0.90 for each of the configurations. The transonic drag-rise incremental coefficient was large and was approximately 0.05 for the complete model and approximately 0.045 for the complete model less tail and for the complete model plus spoiler. The incremental drag coefficient of the tail was approximately 0.004 at subcritical speeds and 0.01 at the maximum supersonic speeds, and that of the spoiler was 0.02 at subcritical speeds and 0.015 at the highest supersonic speeds (fig. 20).

The addition of a transition strip to the complete model increased the drag coefficient considerably more than might be expected from previous tests (fig. 21). The increase in drag coefficient was approximately 0.007 throughout the Mach number range of the tests.

The addition of the small end plates to the complete model increased the drag coefficient by 0.002 at an angle of attack of $0^\circ$ at a Mach number of 0.90 and by 0.005 at the highest supersonic Mach numbers (fig. 22). The larger end plates further increased the drag coefficient by about 0.002 throughout the Mach number range.

The radar and control-cable housings increased the drag coefficient by approximately 0.002 at an angle of attack of $0^\circ$ at high subsonic Mach numbers (figs. 12 and 14).

## Drag-Rise Factor

The drag-rise factor $\Delta C_D/(\Delta C_L)^2$ shown in figure 23 is an average value applicable up to a lift coefficient of approximately 0.3. Also shown in figure 23 is the theoretical variation with Mach number of the drag-rise factor for zero leading-edge suction $1/57.3C_{l_\alpha}$, where $C_{l_\alpha}$ was the experimental value of lift-curve slope obtained in the Langley 8-foot transonic tunnel tests (fig. 18).

The drag-rise factor $\Delta C_D/(\Delta C_L)^2$ for the various configurations varied from 0.1 at the lower subsonic speeds to 0.2 at the highest supersonic speeds (fig. 23). Changes in configuration had small effect on the value of the factor. The greater scatter shown by the Langley data was probably a result of larger angle-of-attack increments at which the drag data were taken in the Langley tests. At the higher transonic speeds, the drag-rise factor nearly equaled the value for zero leading-edge suction.

## Maximum Lift-Drag Ratio

The maximum lift-drag ratio of the complete model reached a maximum value of approximately 12.5 at a Mach number of approximately 0.85, as shown by the WADC results in figure 24. The value for the complete model at supersonic speeds was 4.4. The addition of a spoiler to the complete model decreased the maximum lift-drag ratio considerably at subsonic speeds; the decrease at the highest supersonic speeds was 14 percent.

The lift coefficient corresponding to the maximum lift-drag ratio for the complete model was approximately 0.35 at the lower subsonic test Mach numbers, and the value increased by approximately 0.2 at transonic speeds (fig. 25).

## Directional Stability

The directional- and lateral-stability derivatives presented in figures 26 to 29, inclusive, are average values for angles of yaw from $-1^\circ$ to $1^\circ$.

The directional-stability derivative $C_{n_\psi}$ of the complete model as obtained from the Langley and WADC tests generally agreed well at an angle of attack of $0^\circ$ (fig. 26(a)), but the Langley data showed a greater stability at subsonic Mach numbers at an angle of attack of approximately $2.5^\circ$ (fig. 26(b)). A decrease in directional stability occurred at Mach numbers near 1 (fig. 26), but this decrease was limited only to small angles of yaw (see figs. 8 and 10).

The addition of a transition strip increased the directional stability of the complete model at an angle of attack of $0^\circ$ at Mach numbers less than 0.95 and showed small effect at the higher test Mach numbers (fig. 26(a)). The decrease in directional stability at small angles of yaw near Mach numbers of 1 observed for the smooth configuration also occurred for the model with the transition strip.

The complete model less tail was directionally unstable throughout the Mach number range with an approximately constant value of the derivative $C_{n_\psi}$ of 0.002 (fig. 27). Good agreement was shown between the results from the two test facilities.

The addition of the small and large end plates to the wing increased the directional stability of the complete model throughout the Mach number range, although the effect of the end plates was very small at Mach numbers near 0.97, and prevented the large loss in directional stability which occurred at small angles of yaw at Mach numbers near 1 for the

complete model (figs. 28 and 29). The small end plates were relatively more effective than the large end plates in increasing the directional stability except at the highest Mach numbers.

The radar and control-cable housings had no effect on the directional stability in the test Mach number range covered (fig. 28).

## Lateral Stability

The effective-dihedral derivative $C_{l_\psi}$ for the complete model at an angle of attack of $0^\circ$ gradually increased with Mach number at subsonic speeds and attained a maximum subsonic value of 0.0023 at a Mach number of approximately 0.98 (fig. 26(a)). The supersonic value was generally slightly less than the maximum subsonic value. At an angle of attack of approximately $2.5^\circ$, the effective-dihedral derivative attained a maximum value of 0.0030 at a Mach number of 0.90 (fig. 26(b)). The dihedral-effect data from the two test facilities showed good agreement except at supersonic speeds at an angle of attack of approximately $2.5^\circ$ (fig. 26).

The transition strip had a variable effect on the dihedral effect of the complete model at an angle of attack of $0^\circ$ at subsonic speeds. The transition strip increased the maximum value of $C_{l_\psi}$ to 0.0027 at a Mach number of approximately 0.96 (fig. 26(a)).

The dihedral effect for the complete model less tail at an angle of attack of $0^\circ$ was small throughout the Mach number range, with a maximum value of 0.0006 at a Mach number of 0.96 (fig. 27).

The wing-tip end plates were tested in an attempt to reduce the dihedral effect of the complete model (ref. 6) at transonic speeds, but the end plates actually increased the dihedral effect in a small range of Mach numbers centered about a Mach number of approximately 0.96 (figs. 28 and 29). Outside this small range of Mach numbers, however, the end plates proved to be effective and the increment of reduction in dihedral effect was approximately proportional to the area of the plates.

The radar and control-cable housings had no effect on the effective-dihedral derivative $C_{l_\psi}$ (fig. 28).

## Lateral-Force Characteristics

The agreement in the lateral-force derivative $C_{Y_\psi}$ determined from the Langley and WADC tests was satisfactory for the complete model

(fig. 26) and was excellent for the complete model less tail (fig. 27). The derivative $C_{Y_\psi}$ was only slightly sensitive to change in Mach number. The incremental lateral-force derivative of the tail was approximately 0.01 throughout the Mach number range (figs. 26(a) and 27).

The transition strip generally had negligible effect on the lateral-force derivative (fig. 26(a)).

The end plates had small effect on the derivative $C_{Y_\psi}$ at Mach numbers near 0.96, but at other Mach numbers the end plates noticeably increased the derivative (figs. 28 and 29). This increase was approximately proportional to the area of the end plates.

The radar and control-cable housings had small effect on the lateral-force derivative (fig. 28).

## Incremental Spoiler Characteristics

The incremental force and moment coefficients due to spoiler deflection are shown in figure 30 for several values of angle of attack. The agreement in incremental spoiler characteristics between the Langley and WADC tests was generally satisfactory. The spoiler rolling-moment effectiveness increased with increase in Mach number up to a Mach number of 0.92 and then generally decreased with increase in Mach number (fig. 30(a)). Despite this decrease the spoiler still developed large rolling moments at the higher Mach numbers. The angle of attack for spoiler maximum rolling-moment effectiveness generally decreased with increase in Mach number (fig. 17(c)).

The yawing-moment increment developed by the spoiler was favorable throughout the Mach number range at all angles of attack (fig. 30(a)).

The pitching-moment increment developed by the spoiler was positive throughout the Mach number range at all angles of attack (fig. 30(b)). The maximum increment was approximately 0.08, and this occurred at transonic speeds.

## Pressure Data and Schlieren Photographs

Static-pressure data for the static-tube and fuselage orifices are shown in figure 31 and are also tabulated in table III. As a matter of general interest, a few of the schlieren photographs taken during the tests are presented herein. Photographs of the flow in the regions of the static tube and model base are shown in figures 32 and 33, respectively.

Static-tube pressures and shock patterns in region of static tube.- Small angle-of-attack changes had essentially no effect on the pressure coefficient of the static-tube orifices throughout the Mach number range (fig. 31(a)). The pressure coefficient of the static-tube orifices decreased abruptly at low supersonic Mach numbers; the decrease began at a Mach number of approximately 1 for orifice 1P, at approximately 1.01 for orifice 2P, and at approximately 1.03 for orifice 3P. This decrease in pressure coefficient was associated with the rearward movement of the model bow wave past the orifice with increase in Mach number, as shown by the schlieren photographs of figure 32 where shock (a) is the model bow wave.

At Mach numbers lower than those corresponding to the beginning of the abrupt decrease in pressure coefficient of the static-tube orifices, the static-tube pressures were positive due to the influence of the pressure field of the body. At these lower Mach numbers, the pressure coefficient of orifices 1P and 2P was essentially invariant with Mach number and that for orifice 3P, which was closest to the body, increased with Mach number.

When the model bow wave has moved to the rear of a static-tube orifice, the static pressure at the orifice would be expected to correspond closely at small values of angle of attack to the free-stream static pressure. As figure 31(a) shows, the pressure coefficient deviated from a near-zero value at Mach numbers of 1.01 and 1.02 for orifice 1P and at the highest supersonic Mach numbers for all static-tube orifices. Part of this deviation from the free-stream value may be explained by the poorer accuracy in determining pressure coefficient at supersonic speeds as a result of the decrease in uniformity of the test-section flow at supersonic speeds (see "Accuracy" section).

Some of the other shocks on the static tube were weak and do not show up well in the photographs. A shock (b) at the nose of the static tube and a shock (c) at the enlargement in diameter of the static tube are faintly seen in figure 32(b). The shock (b) is also discernible in the negatives of figure 32 at Mach numbers of 1.01, 1.02, and 1.04 and the shock (c) at a Mach number of 1.04, but these shocks are very difficult to see in the photographs.

Fuselage pressures.- Orifices 1 through 5, and orifice 6 at Mach numbers above 0.96, exhibited an approximately linear variation of pressure coefficient with angle of attack (figs. 31(b) to 31(d); see fig. 5 for orifice locations). The pressure coefficient for orifices 1 through 4, and orifices 5 and 6 at Mach numbers above 0.96, generally increased considerably with increase in Mach number. The pressure coefficient of orifice 21, which was located on the side of the fuselage nose in a region of flow expansion, was insensitive to angle-of-attack changes but showed large variations with change in Mach number (fig. 31(e)).

Orifice 28 was also insensitive to angle-of-attack changes, although the adjacent orifices 27 and 36 were affected by angle-of-attack changes at transonic speeds (fig. 31(f)). The abrupt decrease in pressure coefficient with increase in Mach number for orifices 27, 28, and 36 at Mach numbers beginning at approximately 0.95 was associated with the rearward movement past the orifices of the shock arising from the compression of the flow field of the wing-body configuration and the development of supersonic flow in the region of the orifices. The extent of the decrease in pressure coefficient was somewhat less for orifice 36 than for orifices 27 and 28.

Shock patterns in region of model base.- The shock formations characteristic of the flow in the region of the base of a fuselage-alone configuration and of a wing-fuselage configuration at transonic speeds (see ref. 3, for example) were modified and complicated in the present tests by the presence of the horizontal tail, the vertical tail, and the "bullet" on which the horizontal tail was supported (fig. 33). Shock (a) in figure 33 appears to have originated from the leading edge of the root chord of the horizontal tail. Shock (b) was associated with the deceleration or compression of the flow over the rear portions of the horizontal and vertical tails and the bullet. The position of this shock was probably influenced by the presence of the rear portion of the fuselage and the forward portion of the sting. Shock (c) in figure 33(b) was the reflection off the tunnel boundary of the bow wave from the wing. Shock (d) in figures 33(b) and 33(c), at Mach numbers of 1 and above, was a combined shock formed by the merging of the shock from the juncture of the vertical tail and fuselage and the bow wave ahead of the bullet. At Mach numbers less than 1, an individual bow wave ahead of the bullet is faintly evident in the schlieren photographs. Shock (e) in figure 33(c) was the reflection off the tunnel boundary of the fuselage bow wave (shock (a) in fig. 32). The reflected shock (e) tended to become a normal shock as it approached the field of flow downstream of the model in the vicinity of the sting, in a manner similar to that shown by the data of reference 3. Multiple shocks which were essentially normal to the center line of the model and extended across the entire schlieren view are seen in figure 33(b) at Mach numbers of 1.00 and 1.02; these shocks are believed to be primarily shock manifestations at the tunnel windows, and not at the model.

## CONCLUSIONS

An investigation was made in the Langley 8-foot transonic tunnel of the static lateral, directional, and longitudinal stability characteristics of a 0.06-scale model of the Martin B-61A missile (Matador). The lateral control characteristics of a spoiler and the effect of wing-tip end plates on the effective dihedral of the complete model were also

investigated. The tests were made at Mach numbers from 0.80 to 1.12. The Reynolds number based on the mean aerodynamic chord of the wing was approximately $1.6 \times 10^6$. The following conclusions are indicated:

1. No serious difficulties were indicated in longitudinal and directional stability. A decrease in directional stability occurred near sonic velocity but was limited to small angles of yaw.

2. Spoiler power appeared to be adequate throughout the Mach number range.

3. Langley and Wright Air Development Center results on this model generally showed good agreement.

4. End plates on the wing tips proved ineffective in reducing the dihedral effect at Mach numbers near 0.96 but were effective at other Mach numbers. The effectiveness at the latter Mach numbers was approximately proportional to the area of the plates.

Langley Aeronautical Laboratory,
National Advisory Committee for Aeronautics,
Langley Field, Va., March 24, 1954.

Arvo A. Luoma
Aeronautical Research Scientist

Approved: Eugene C. Draley
Eugene C. Draley
Chief of Full-Scale Research Division

MML

## REFERENCES

1. Rose, L. J., and Linkous, G. F., Jr.: Transonic Test of the B-61A (Matador) Pilotless Aircraft in the Wright Air Development Center 10-Foot Wind Tunnel. Part A. Test Results. Eng. Rep. No. 4915 (Contract AF33(038)-18492), The Glenn L. Martin Co., Apr. 15, 1952.

2. Wright, Ray H., and Ritchie, Virgil S.: Characteristics of a Transonic Test Section With Various Slot Shapes in the Langley 8-Foot High-Speed Tunnel. NACA RM L51H10, 1951.

3. Ritchie, Virgil S., and Pearson, Albin O.: Calibration of the Slotted Test Section of the Langley 8-Foot Transonic Tunnel and Preliminary Experimental Investigation of Boundary-Reflected Disturbances. NACA RM L51K14, 1952.

4. Whitcomb, Charles F., and Osborne, Robert S.: An Experimental Investigation of Boundary Interference on Force and Moment Characteristics of Lifting Models Tested in the Langley 16- and 8-Foot Transonic Tunnels. NACA RM L52L29, 1953.

5. Love, Eugene S.: A Summary of Information on Support Interference at Transonic and Supersonic Speeds. NACA RM L53K12, 1954.

6. Riebe, John M., and Watson, James M.: The Effect of End Plates on Swept Wings at Low Speed. NACA TN 2229, 1950.

TABLE I

GEOMETRIC CHARACTERISTICS OF 0.06-SCALE MODEL OF

MARTIN B-61A MISSILE (MATADOR)

| | |
|---|---|
| **Body:** | |
| Length, ft | 2.250 |
| Maximum diameter, ft | 0.270 |
| Frontal area, sq ft | 0.057 |
| Fineness ratio $\left(\text{Length}/\sqrt{\text{Frontal area}}\right)$ | 9.400 |
| Frontal area/Wing area | 0.088 |
| Base area, sq ft | 0.018 |
| **Wing ($W^1$):** | |
| Airfoil section (in plane perpendicular to chord plane and parallel to root chord) | NACA 63A008 |
| Root chord, ft | 0.475 |
| Tip chord, ft | 0.285 |
| Span (projected), ft | 1.713 |
| Area (projected), sq ft | 0.648 |
| Aspect ratio ($(\text{Projected span})^2/(\text{Projected area})$) | 4.53 |
| Taper ratio | 0.60 |
| Mean aerodynamic chord, ft | 0.387 |
| Spanwise location of mean aerodynamic chord, ft | 0.392 |
| Distance (parallel to root chord) from leading edge of root chord to leading edge of mean aerodynamic chord, ft | 0.298 |
| Sweepback (in chord plane) | |
| Leading edge, deg | 37.1 |
| 25-percent-chord line, deg | 35.0 |
| Dihedral, deg | -5.0 |
| Incidence of root chord with respect to body center line, deg | 0 |
| Location of root chord above body center line, ft | 0.102 |
| Location of leading edge of root chord from nose of body, ft | 0.620 |
| Twist, deg | 0 |
| **Wing ($W^{1A}$):** | |
| Airfoil section (in plane perpendicular to chord plane and parallel to root chord) | NACA 63A008 |
| Root chord, ft | 0.475 |
| Tip chord, ft | 0.285 |
| Span (projected), ft | 1.694 |
| Area (projected), sq ft | 0.644 |
| Aspect ratio ($(\text{Projected span})^2/(\text{Projected area})$) | 4.46 |
| Taper ratio | 0.60 |

TABLE I.- Continued

GEOMETRIC CHARACTERISTICS OF 0.06-SCALE MODEL OF

MARTIN B-61A MISSILE (MATADOR)

| | |
|---|---|
| Mean aerodynamic chord, ft | 0.388 |
| Spanwise location of mean aerodynamic chord, ft | 0.388 |
| Distance (parallel to root chord) from leading edge of root chord to leading edge of mean aerodynamic chord, ft | 0.295 |
| Sweepback (in chord plane): | |
| Leading edge, deg | 37.1 |
| 25-percent-chord line, deg | 35.0 |
| Dihedral, deg | -5.0 |
| Incidence of root chord with respect to body center line, deg | 0 |
| Location of root chord above body center line, ft | 0.102 |
| Location of leading edge of root chord from nose of body, ft | 0.620 |
| Twist, deg | 0 |
| Horizontal tail ($H^1$): | |
| Airfoil section (in plane perpendicular to chord plane and parallel to root chord) | NACA 63A006 |
| Root chord, ft | 0.205 |
| Tip chord, ft | 0.103 |
| Span (projected), ft | 0.565 |
| Area (projected), sq ft | 0.087 |
| Aspect ratio ((Projected span)$^2$/(Projected area)) | 3.67 |
| Taper ratio | 0.50 |
| Mean aerodynamic chord, ft | 0.160 |
| Spanwise location of mean aerodynamic chord, ft | 0.125 |
| Distance (parallel to root chord) from leading edge of root chord to leading edge of mean aerodynamic chord, ft | 0.102 |
| Sweepback (in chord plane): | |
| Leading edge, deg | 38.2 |
| 25-percent-chord line, deg | 35.0 |
| Dihedral, deg | 15.00 |
| Location of root chord (at 0° incidence) above body center line, ft | 0.370 |
| Location of leading edge of root chord (at 0° incidence) from nose of body, ft | 2.045 |
| Twist, deg | 0 |

TABLE I.- Concluded

GEOMETRIC CHARACTERISTICS OF 0.06-SCALE MODEL OF

MARTIN B-61A MISSILE (MATADOR)

| | |
|---|---|
| Vertical tail (V): | |
| Airfoil section (in plane perpendicular to chord plane and parallel to body center line) | NACA 66-007 Mod. |
| Area, exposed (from juncture of body and vertical tail to root-chord line of horizontal tail at $0^{\circ}$ incidence), sq ft | 0.090 |
| Span, effective (distance from effective root chord to tip chord), ft | 0.265 |
| Root chord, effective (parallel to body center line and based on exposed area), ft | 0.478 |
| Location of effective root chord from body center line, ft | 0.105 |
| Location of leading edge of effective root chord from nose of body, ft | 1.772 |
| Tip chord (intersection of leading and trailing edges with root-chord line of horizontal tail at $0^{\circ}$ incidence), ft | 0.205 |
| Aspect ratio ((Effective span)$^2$/(Exposed area)) | 0.78 |
| Taper ratio | 0.43 |
| Mean aerodynamic chord, ft | 0.359 |
| Location of mean aerodynamic chord from effective root chord, ft | 0.114 |
| Distance (parallel to body center line) from leading edge of effective root chord to leading edge of mean aerodynamic chord, ft | 0.118 |
| Sweep angle: | |
| Leading edge, deg | 45.9 |
| 25-percent-chord line, deg | 37.8 |

TABLE II

CONFIGURATIONS AND TEST CONDITIONS FOR FORCE TESTS AND INDEX OF BASIC FIGURES

| Configuration | Model condition | Type of test | $\alpha$, deg | $\psi$, deg | M | Figure |
|---|---|---|---|---|---|---|
| $N^1B^3W^1A H_o{}^1V$ (Complete model) | Smooth | Yaw | -0.1 | -5 to 5 (approx.) | 0.80 to 1.12 | 8 |
| | Transition strip | Yaw | -.1 | -4 to 5 (approx.) | .80 to 1.02 | 9 |
| | Smooth | Yaw | 2.7 | -5 to 5 (approx.) | .80 to 1.00 | 10 |
| | | | | -4 to 4 (approx.) | 1.01 to 1.11 | |
| | Smooth | Pitch | -5 to 7.5 (approx.) | 0 | .80 to 1.12 | 11 |
| $N^1B^3W^1A_E{}^1H_o{}^1V$ (Complete model plus small end plates) | Smooth | Yaw | -.2 | -4 to 5 (approx.) | .90 to 1.13 | 12 |
| $N^1B^3W^1A_E{}^2H_o{}^1V$ (Complete model plus large end plates) | Smooth | Yaw | -.2 | -4 to 5 (approx.) | .90 to 1.12 | 13 |
| $N^1B^1W^1A_E{}^1H_o{}^1V$ (Complete model less radar and control-cable housings and plus small end plates) | Smooth | Yaw | -.2 | -4 to 5 (approx.) | .92 to .98 | 14 |
| $N^1B^2W^1A$ (Complete model less tail less control-cable housing) | Smooth | Yaw | -.1 | -4 to 5 (approx.) | .90 to 1.10 | 15 |
| | Smooth | Pitch | -5 to 5 (approx.) | 0 | .90 to 1.02 | 16 |
| | | | 0 | | 1.10 | |
| $N^1B^3W^1A H_o{}^1VS^1$ (Complete model plus spoiler) | Smooth | Pitch | -5.5 to 7.5 (approx.) | 0 | .80 to 1.10 | 17 |

TABLE III

STATIC-PRESSURE-COEFFICIENT VALUES FOR

CONFIGURATION $N^3B^2W^1A$

$[\psi = 0^\circ]$

| M | α, deg | Pressure coefficient, P, for following static-pressure orifices (see fig. 5 for location of orifices) | | | | | | | | | | | | |
|---|---|---|---|---|---|---|---|---|---|---|---|---|---|---|
| | | P1 | P2 | P3 | 1 | 2 | 3 | 4 | 5 | 6 | 21 | 27 | 36 | 28 |
| 0.90 | -1 | 0.008 | 0.016 | 0.042 | 0.451 | 0.258 | 0.009 | -0.088 | -0.149 | -0.136 | -0.148 | 0.012 | -0.002 | -0.020 |
| | 0 | .012 | .019 | .045 | .434 | .235 | -.008 | -.101 | -.159 | -.138 | -.142 | .013 | -.002 | -.019 |
| | 1 | .007 | .015 | .040 | .410 | .210 | -.027 | -.118 | -.173 | -.146 | -.146 | .011 | -.005 | -.021 |
| .95 | -1 | .009 | .017 | .046 | .479 | .283 | .024 | -.086 | -.176 | -.290 | -.166 | .026 | .014 | -.002 |
| | 0 | .010 | .021 | .048 | .465 | .262 | .007 | -.098 | -.182 | -.291 | -.170 | .031 | .016 | -.001 |
| | 1 | .009 | .018 | .048 | .442 | .239 | -.008 | -.113 | -.190 | -.287 | -.168 | .028 | .012 | -.003 |
| .96 | -1 | .009 | .017 | .046 | .486 | .289 | .030 | -.082 | -.171 | -.303 | -.317 | .012 | .011 | 0 |
| | 0 | .008 | .018 | .047 | .471 | .266 | .012 | -.098 | -.181 | -.313 | .338 | .014 | .010 | -.001 |
| | 1 | .008 | .018 | .048 | .448 | .244 | -.005 | -.112 | -.193 | -.319 | -.337 | .015 | .008 | -.003 |
| .97 | -1 | .009 | .019 | .050 | .493 | .297 | .036 | -.077 | -.166 | -.302 | -.375 | -.036 | -.020 | -.019 |
| | 0 | .008 | .018 | .049 | .479 | .274 | .018 | -.093 | -.180 | -.310 | -.375 | -.034 | -.024 | -.024 |
| | 1 | .008 | .018 | .050 | .459 | .253 | .004 | -.105 | -.188 | -.314 | -.374 | -.028 | -.024 | -.025 |
| .98 | -1 | .010 | .021 | .054 | .502 | .305 | .045 | -.069 | -.161 | -.293 | -.368 | -.071 | -.072 | -.102 |
| | 0 | .011 | .021 | .055 | .488 | .283 | .027 | -.084 | -.170 | -.300 | -.366 | -.061 | -.069 | -.101 |
| | 1 | .011 | .021 | .055 | .468 | .262 | .012 | -.096 | -.178 | -.307 | -.364 | -.053 | -.069 | -.108 |
| .99 | -1 | .010 | .022 | .055 | .513 | .315 | .055 | -.059 | -.151 | -.285 | -.360 | -.066 | -.064 | -.107 |
| | 0 | .009 | .021 | .056 | .499 | .293 | .037 | -.074 | -.162 | -.292 | -.359 | -.057 | -.062 | -.109 |
| | 1 | .009 | .022 | .056 | .479 | .270 | .020 | -.087 | -.170 | -.300 | -.357 | -.047 | -.061 | -.111 |
| 1.00 | -1 | .014 | .022 | .060 | .520 | .323 | .065 | -.049 | -.142 | -.275 | -.349 | -.049 | -.048 | -.088 |
| | 0 | .014 | .022 | .061 | .508 | .301 | .045 | -.063 | -.153 | -.282 | -.347 | -.037 | -.045 | -.089 |
| | 1 | .014 | .022 | .061 | .486 | .280 | .031 | -.075 | -.162 | -.288 | -.345 | -.029 | -.043 | -.092 |
| 1.01 | -1 | -.021 | .016 | .069 | .533 | .336 | .078 | -.032 | -.127 | -.259 | -.333 | -.075 | -.052 | -.088 |
| | 0 | -.019 | .022 | .070 | .519 | .295 | .061 | -.047 | -.139 | -.265 | -.330 | -.063 | -.046 | -.087 |
| | 1 | -.018 | .022 | .070 | .497 | .291 | .044 | -.061 | -.150 | -.275 | -.331 | -.055 | -.042 | -.090 |
| 1.02 | -1 | -.013 | -.003 | .081 | .543 | .350 | .091 | -.020 | -.113 | -.246 | -.320 | -.077 | -.050 | -.082 |
| | 0 | -.014 | -.007 | .081 | .528 | .324 | .070 | -.036 | -.129 | -.256 | -.320 | -.073 | -.049 | -.085 |
| | 1 | -.013 | -.001 | .082 | .510 | .306 | .057 | -.044 | -.135 | -.258 | -.316 | -.062 | -.039 | -.081 |
| 1.04 | -1 | .005 | -.003 | -.004 | .566 | .374 | .122 | .016 | -.075 | -.205 | -.278 | -.082 | -.048 | -.071 |
| | 0 | .003 | -.004 | -.005 | .550 | .352 | .104 | -.001 | -.088 | -.214 | -.276 | -.073 | -.042 | -.070 |
| | 1 | .002 | -.006 | -.009 | .530 | .331 | .090 | -.010 | -.099 | -.220 | -.276 | -.065 | -.037 | -.074 |
| 1.10 | -1 | -.038 | -.026 | -.004 | .601 | .390 | .130 | .042 | -.060 | -.183 | -.244 | -.037 | -.002 | -.015 |
| | 0 | -.036 | -.033 | 0 | .596 | .369 | .113 | .031 | -.071 | -.188 | -.243 | -.035 | .004 | -.014 |
| | 1 | -.033 | -.034 | -.004 | .571 | .351 | .104 | .022 | -.078 | -.190 | -.244 | -.027 | .010 | -.015 |
| 1.12 | 0 | -.032 | -.024 | -.023 | .606 | .371 | .120 | .036 | -.057 | -.178 | -.235 | -.038 | .003 | -.007 |

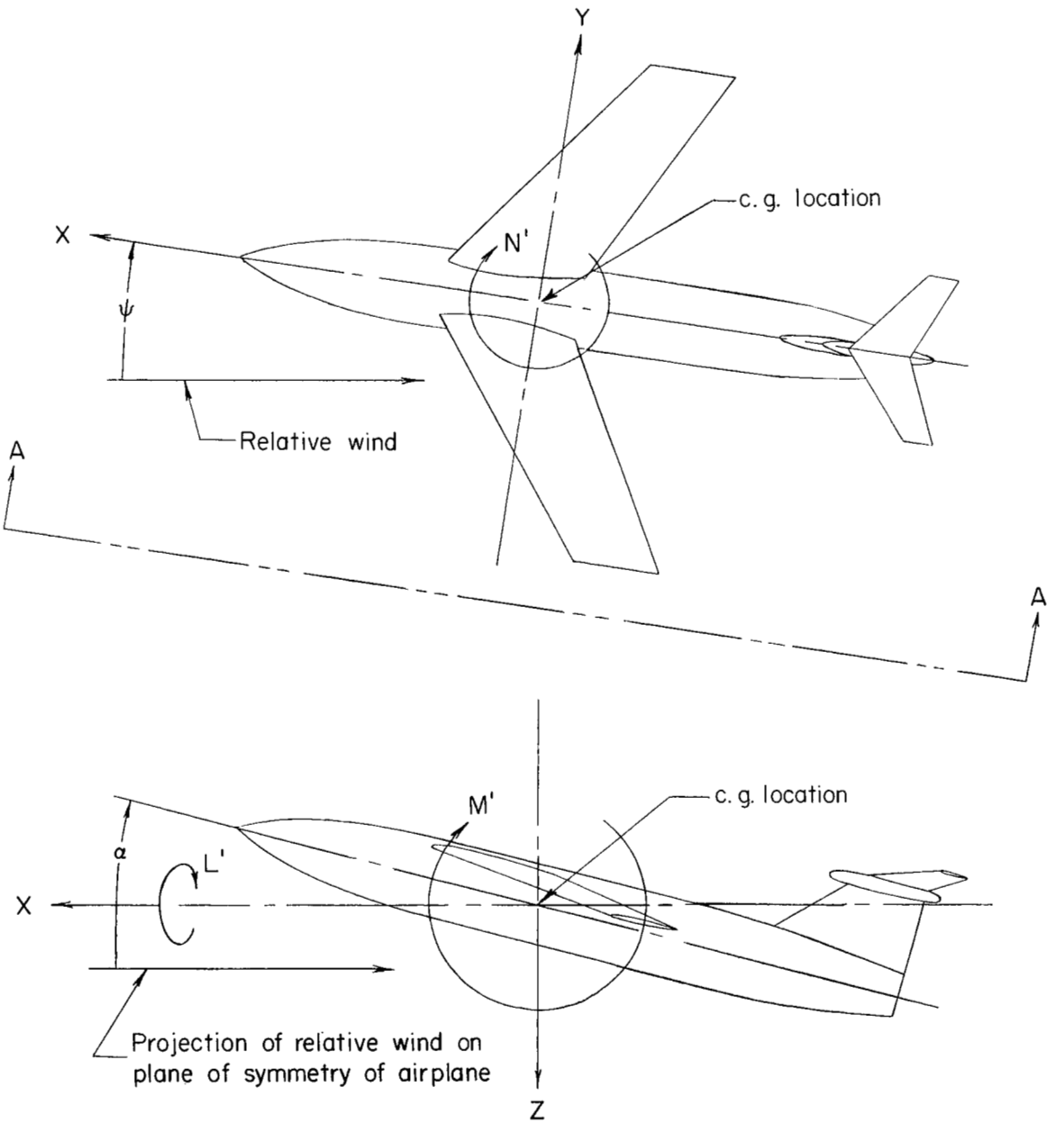


View A-A

Figure 1.- Stability axes. Positive directions of forces, moments, and angles shown.

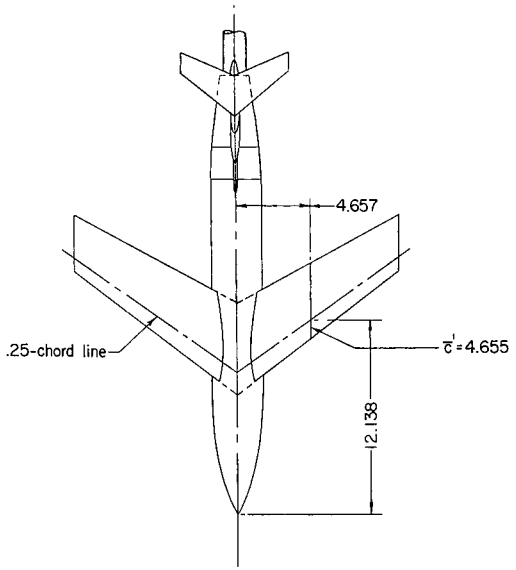


Ogival nose ($N^1$) ordinates

| Station, x | Radius, y |
|---|---|
| 0 | 0 |
| .15 | .107 |
| .30 | .199 |
| .60 | .356 |
| 1.20 | .608 |
| 1.80 | .810 |
| 2.40 | .981 |
| 3.06 | 1.140 |
| 3.60 | 1.262 |
| 4.20 | 1.358 |
| 4.80 | 1.447 |
| 5.40 | 1.519 |
| 6.00 | 1.573 |
| 6.60 | 1.608 |
| 7.102 | 1.620 |
| 7.30 | 1.620 |

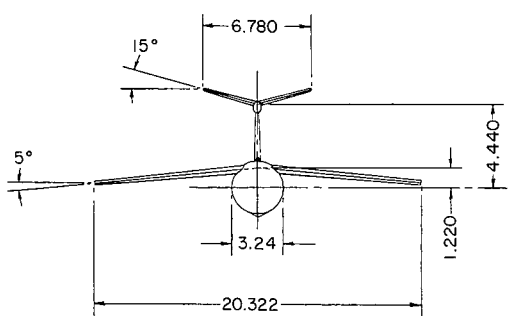


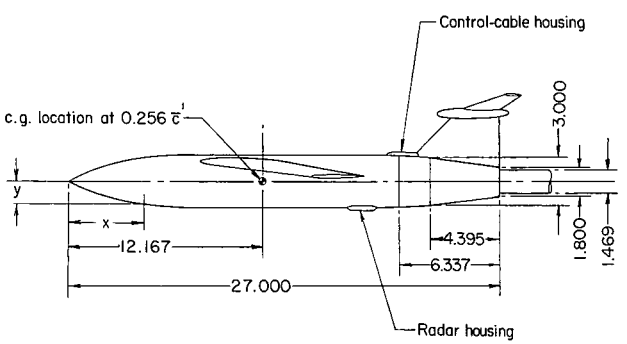


Figure 2.- General arrangement of 0.06-scale model of Martin B-61A missile (Matador); complete model ($N^1B^3W^{1A}H_o{}^1V$). All dimensions in inches except as noted.

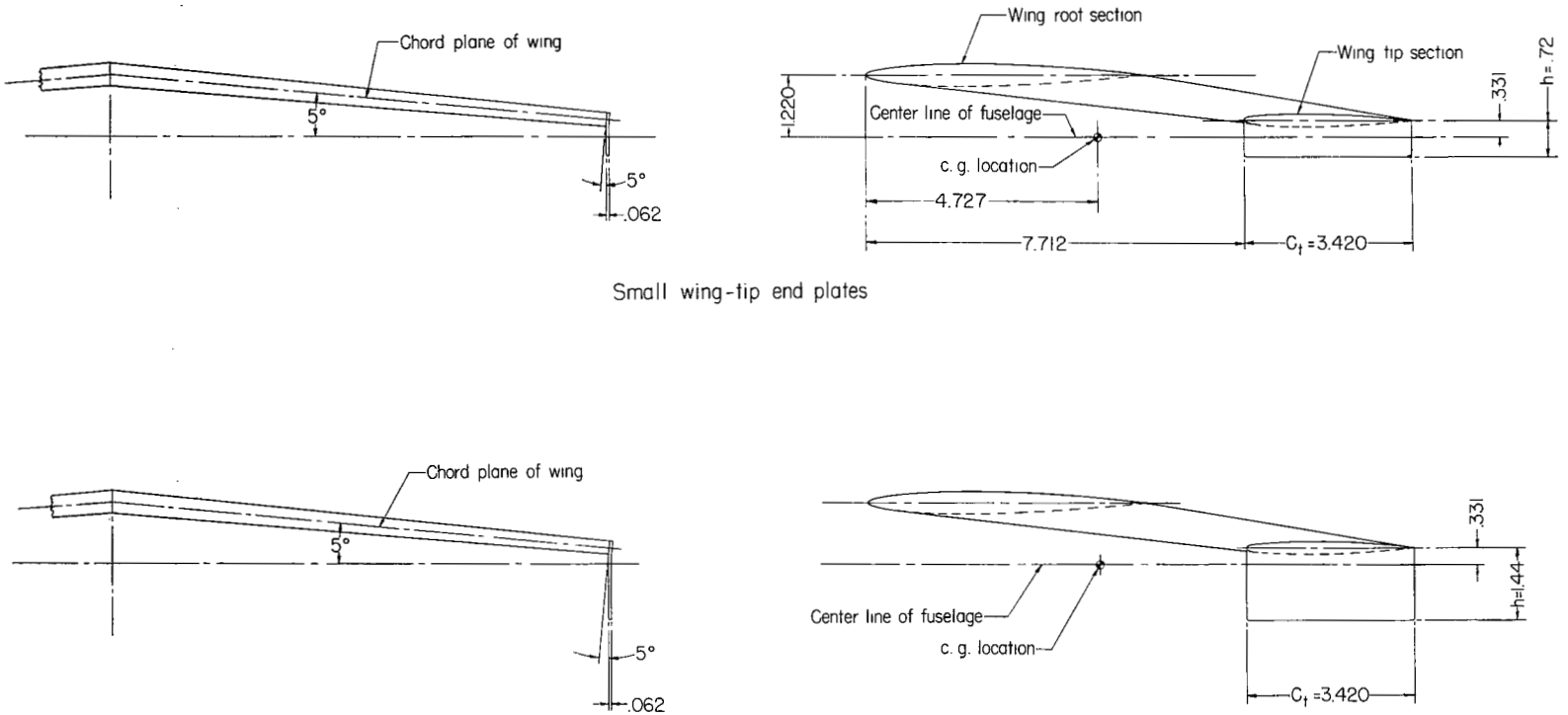


Figure 3.- Dimensions and locations of wing-tip end plates. All dimensions in inches except as noted.

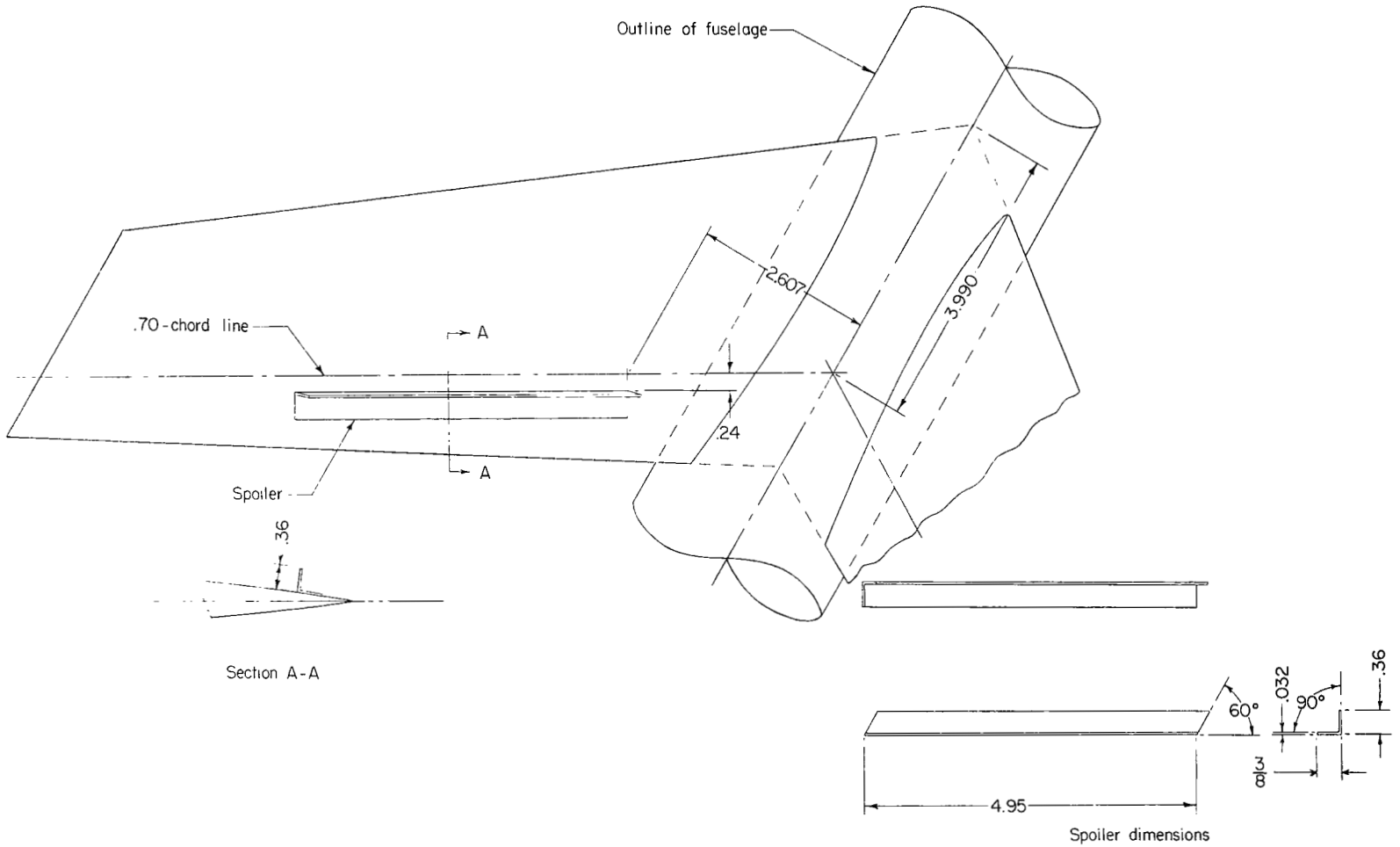


Figure 4.- Dimensions of spoiler and location on upper surface of left semispan of wing. All dimensions in inches except as noted.

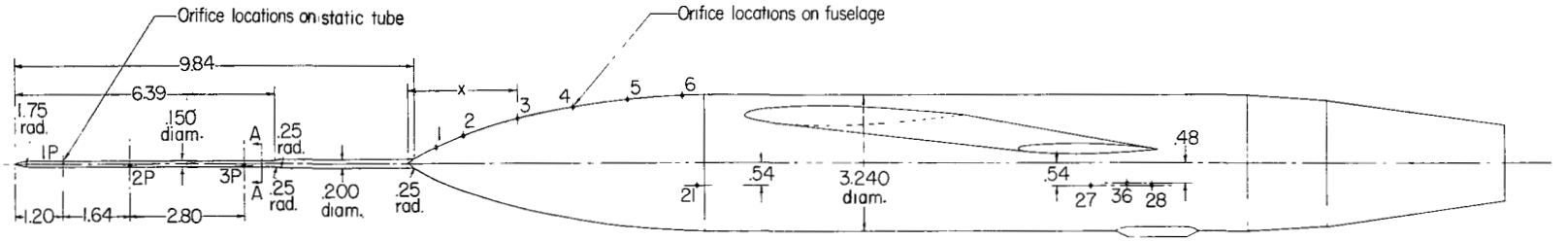


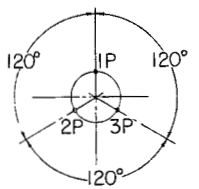


Section A-A (enlarged)

Orifice station locations on fuselage

| Orifice no. | Station, x |
|---|---|
| 1 | 0.68 |
| 2 | 1.35 |
| 3 | 2.70 |
| 4 | 4.05 |
| 5 | 5.40 |
| 6 | 6.75 |
| 21 | 7.10 |
| 27 | 16.80 |
| 36 | 17.70 |
| 28 | 18.30 |

Figure 5.- Static-pressure orifice locations on static tube and fuselage. All dimensions in inches except as noted.

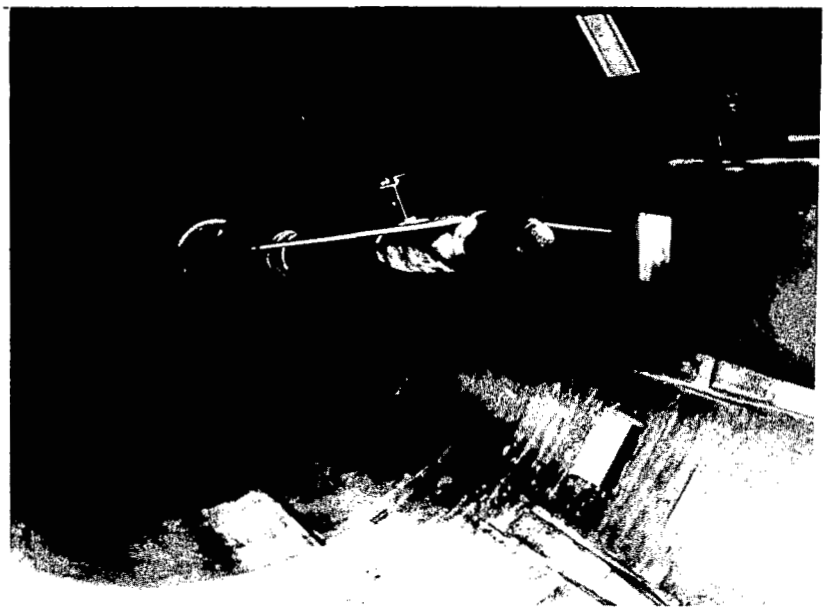

L-77355

(a) Pitch tests (model horizontal).

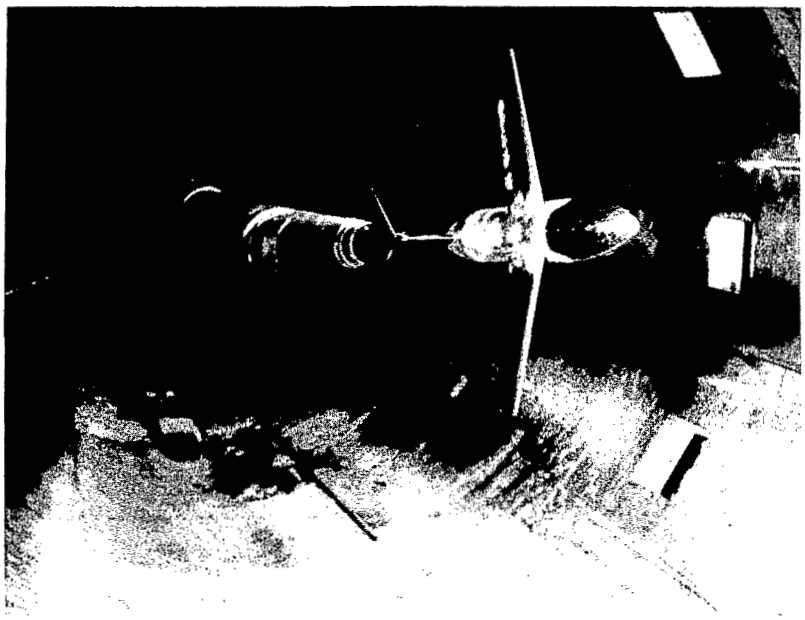

L-77359

(b) Yaw tests (model vertical).

Figure 6.- Installation of 0.06-scale model of Martin B-61A missile (Matador) for pitch and yaw tests in Langley 8-foot transonic tunnel.

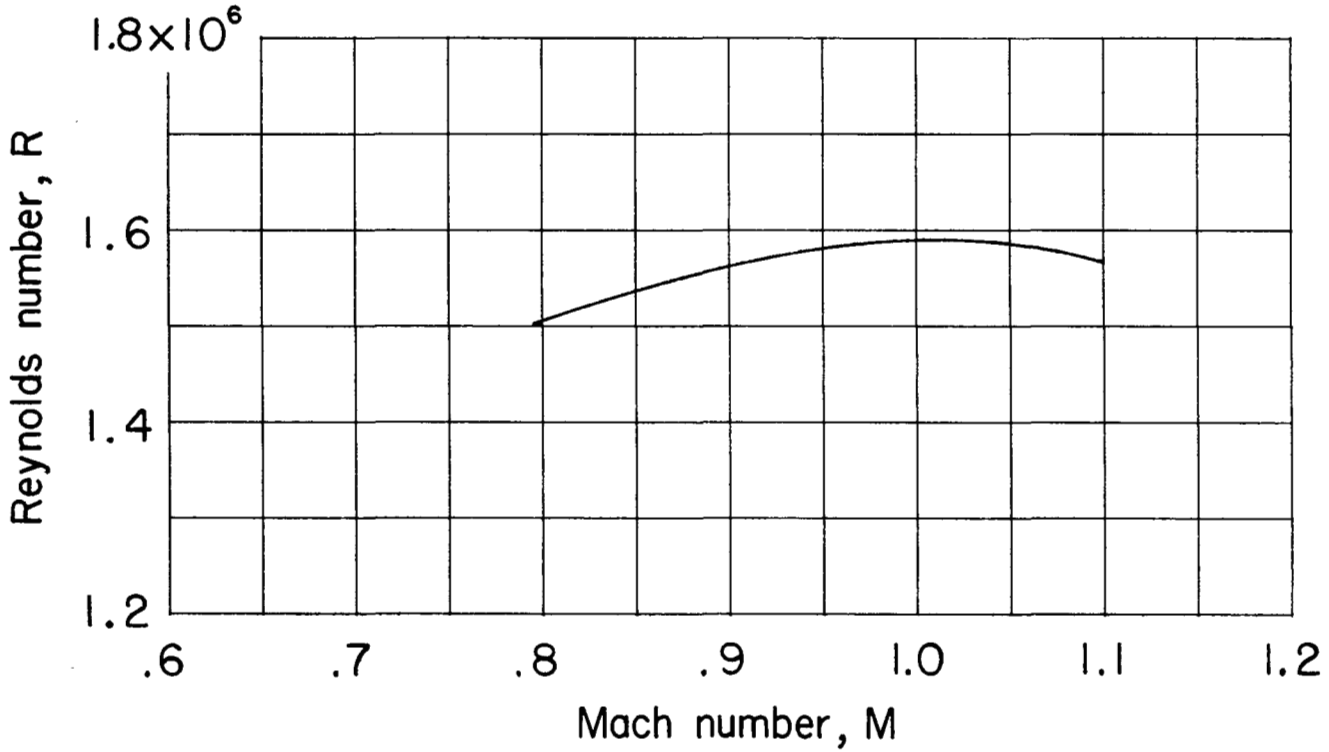


Figure 7.- Variation of average Reynolds number with Mach number in tests of 0.06-scale model of Martin B-61A missile (Matador) in Langley 8-foot transonic tunnel. $\bar{c}$ = 4.646 inches.

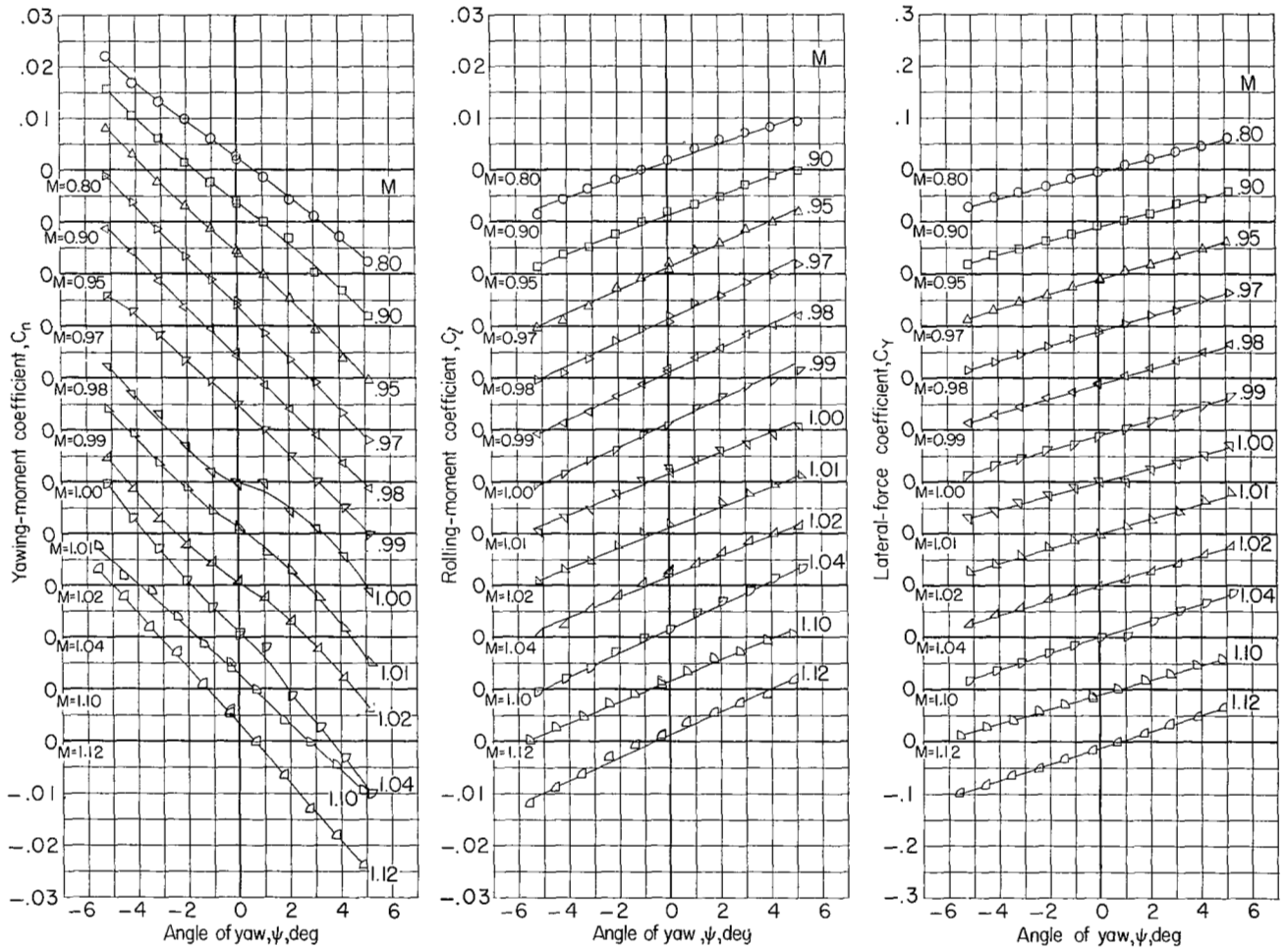


(a) Yawing-moment, rolling-moment, and lateral-force coefficients.

Figure 8.- Variation of aerodynamic characteristics with angle of yaw. Complete model $\left(N^{1}B^{3}W^{1A}H_{o}{}^{1}V\right)$; $\alpha = -0.1^{\circ}$.

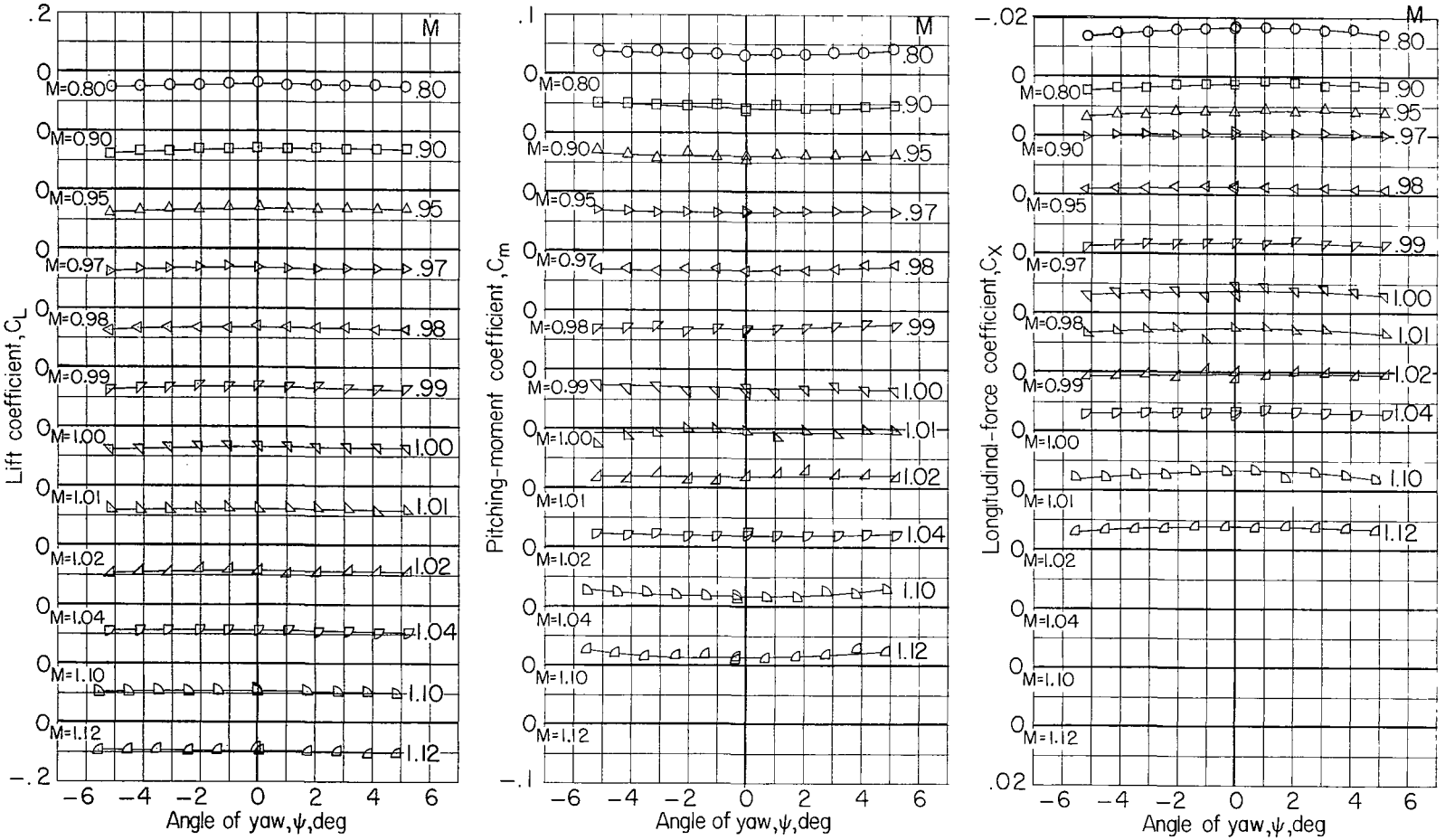


(b) Lift, pitching-moment, and longitudinal-force coefficients.

Figure 8.- Concluded.

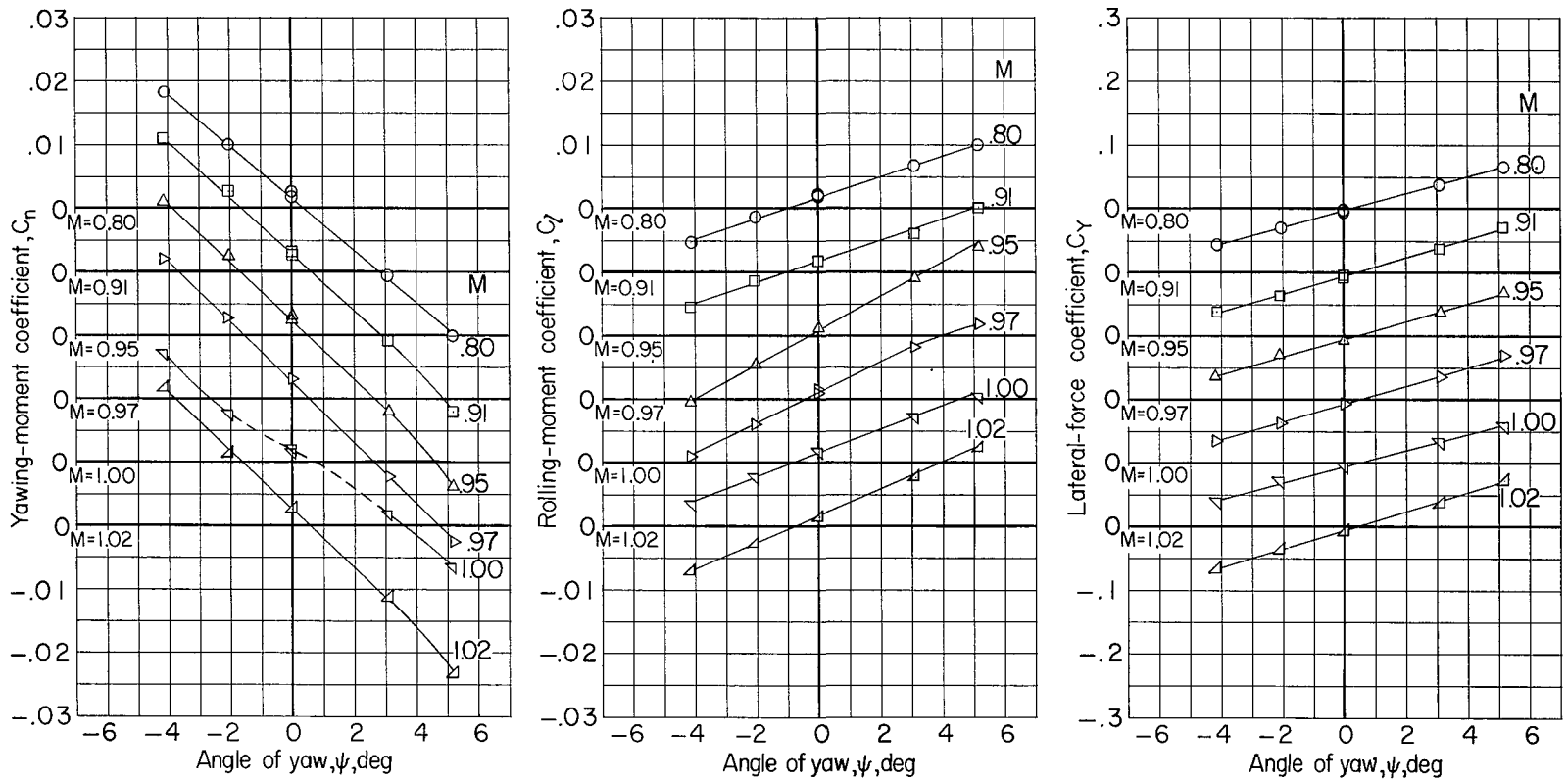


(a) Yawing-moment, rolling-moment, and lateral-force coefficients.

Figure 9.- Variation of aerodynamic characteristics with angle of yaw. Complete model $\left(N^{1}B^{3}W^{1A}H_{o}{}^{1}V\right)$; $\alpha = -0.1^{\circ}$. Transition fixed.

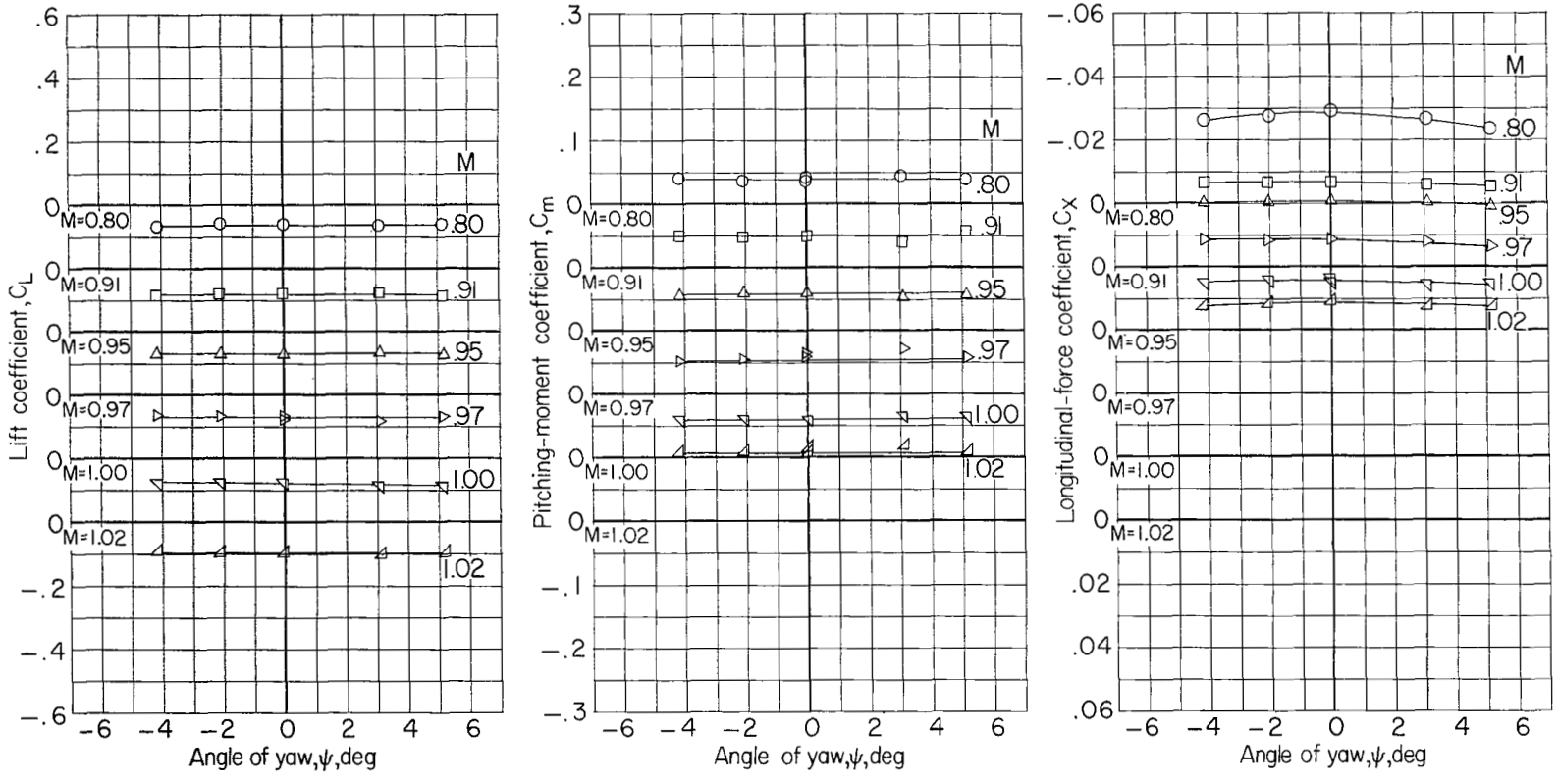


(b) Lift, pitching-moment, and longitudinal-force coefficients.

Figure 9.- Concluded.

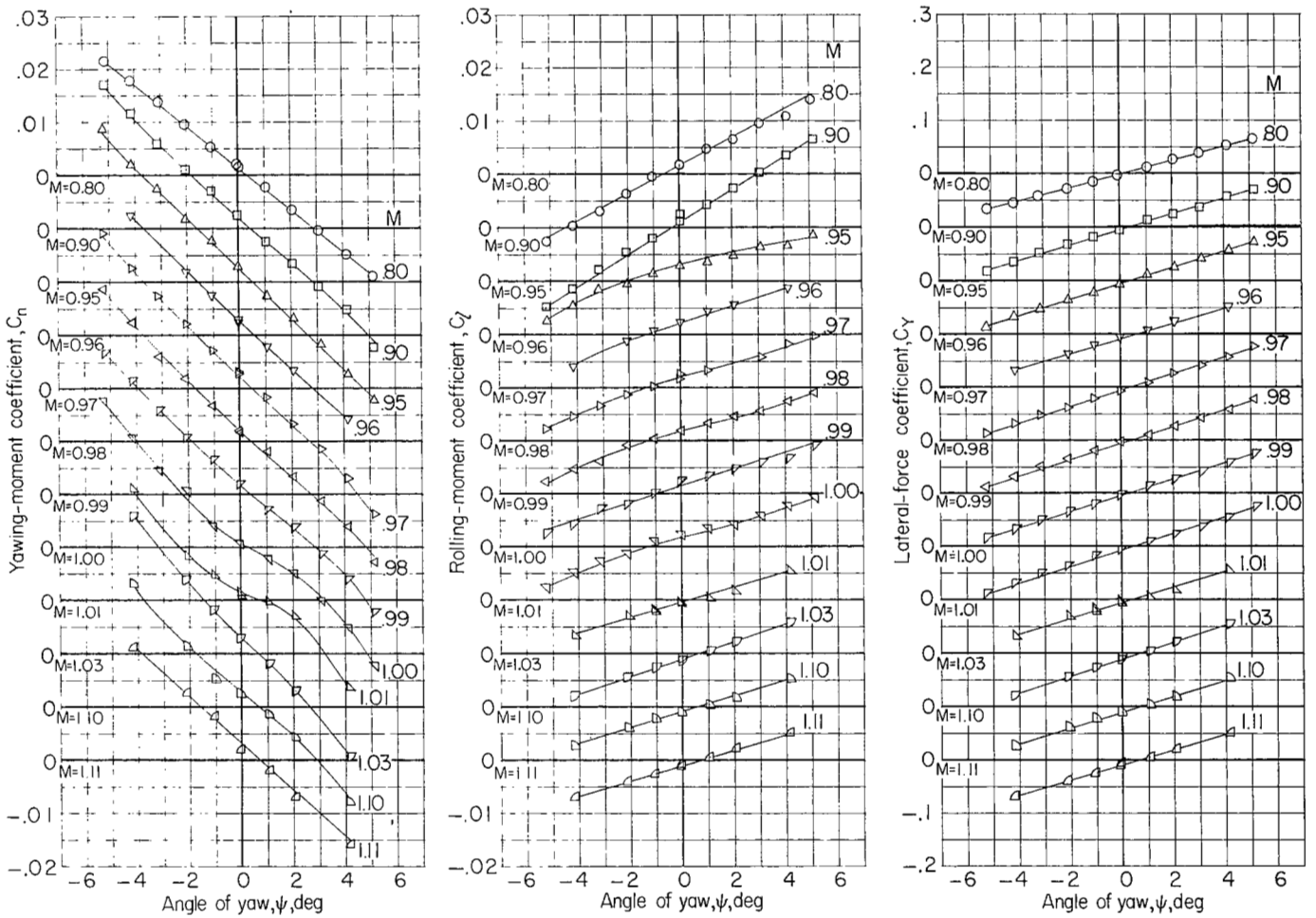


(a) Yawing-moment, rolling-moment, and lateral-force coefficients.

Figure 10.- Variation of aerodynamic characteristics with angle of yaw. Complete model $\left(N^{1}B^{3}W^{1A}H_{o}{}^{1}V\right)$; $\alpha = 2.7^{\circ}$.

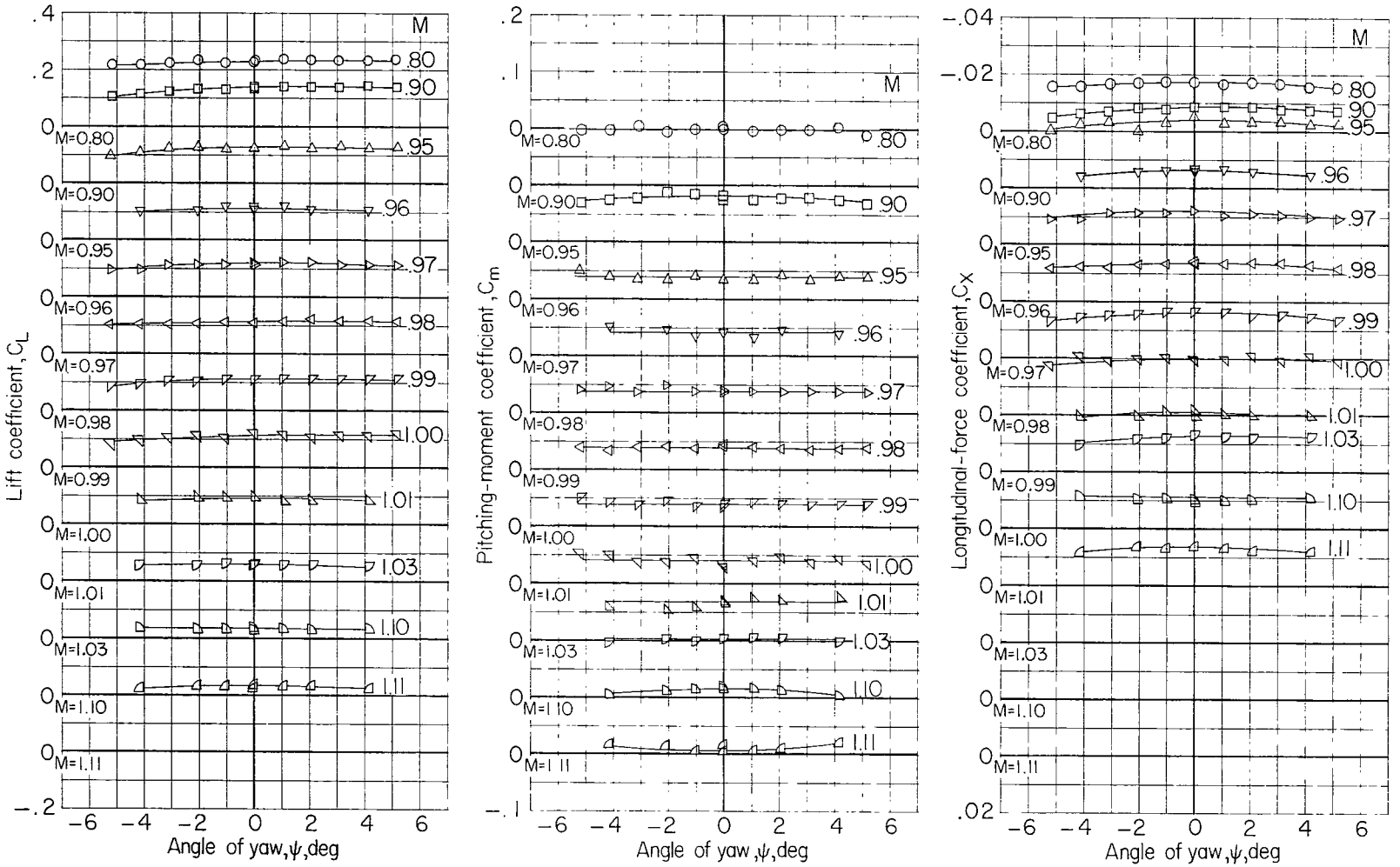


(b) Lift, pitching-moment, and longitudinal-force coefficients.

Figure 10.- Concluded.

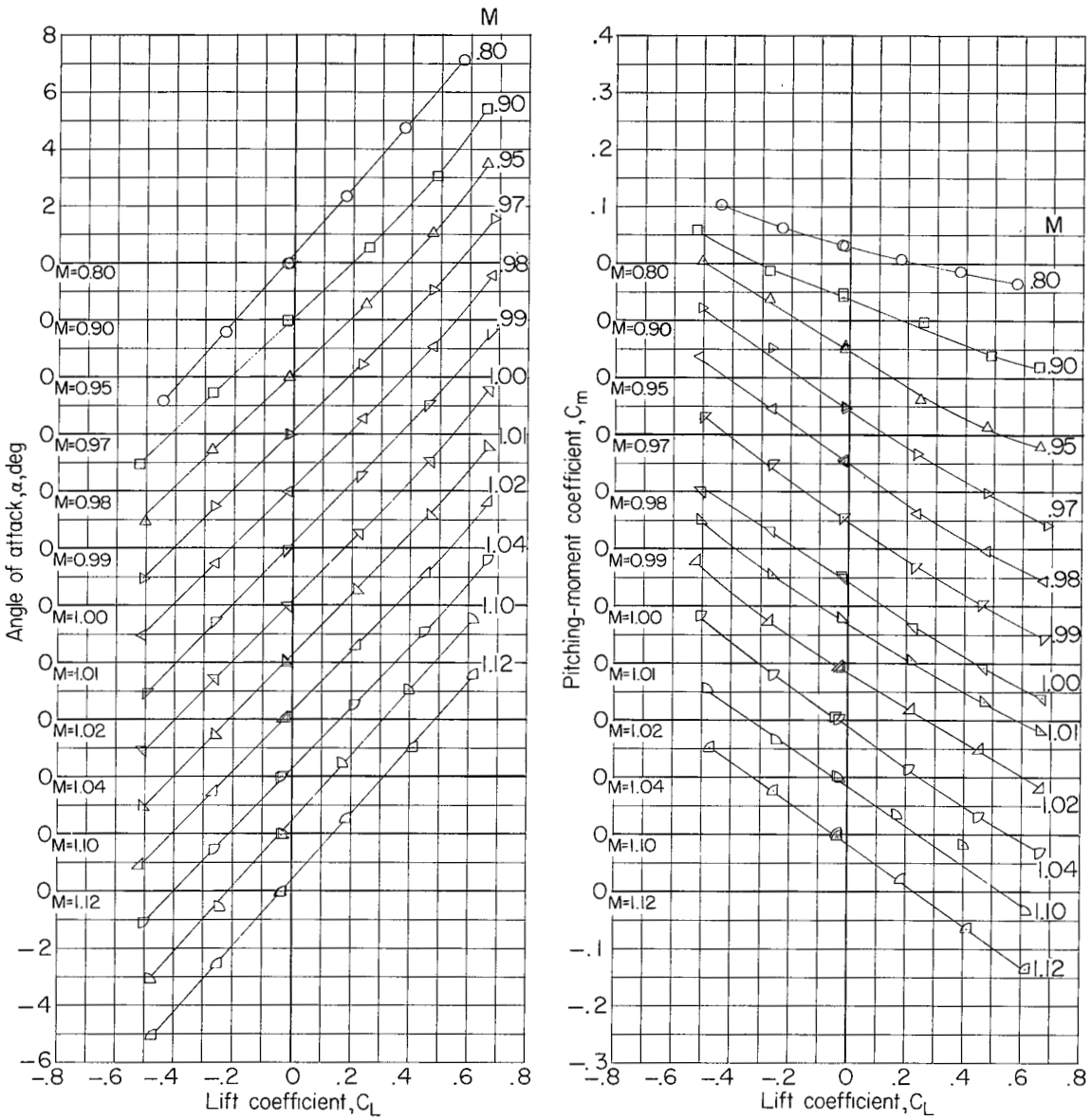


(a) Angle of attack and pitching-moment coefficient.

Figure 11.- Variation of aerodynamic characteristics with lift coefficient (or angle of attack). Complete model $\left(N^1B^3W^{1A}H_O{}^1V\right)$; $\psi = 0^\circ$.

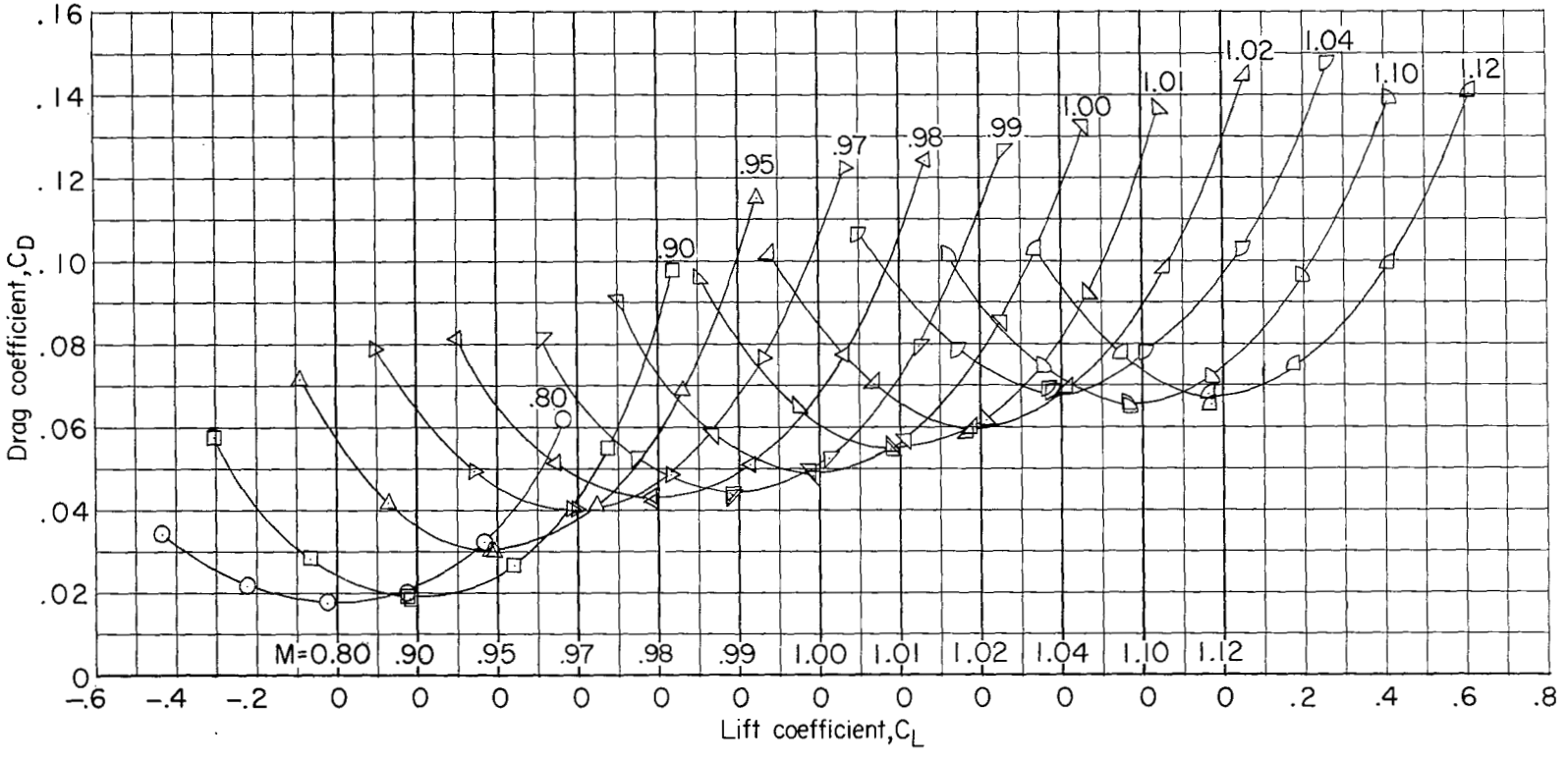


(b) Drag coefficient.

Figure 11.- Continued.

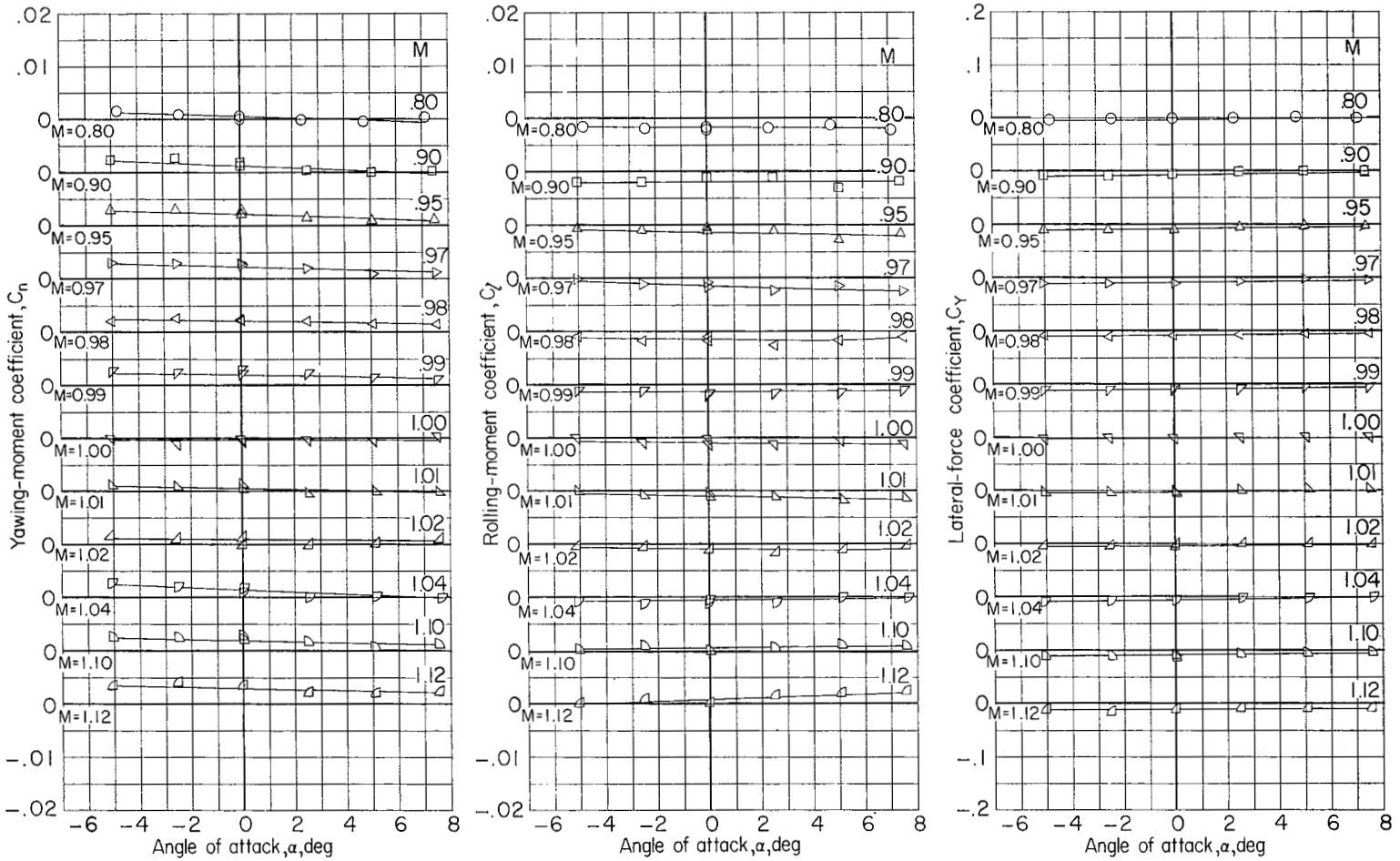


(c) Yawing-moment, rolling-moment, and lateral-force coefficients.

Figure 11.- Concluded.

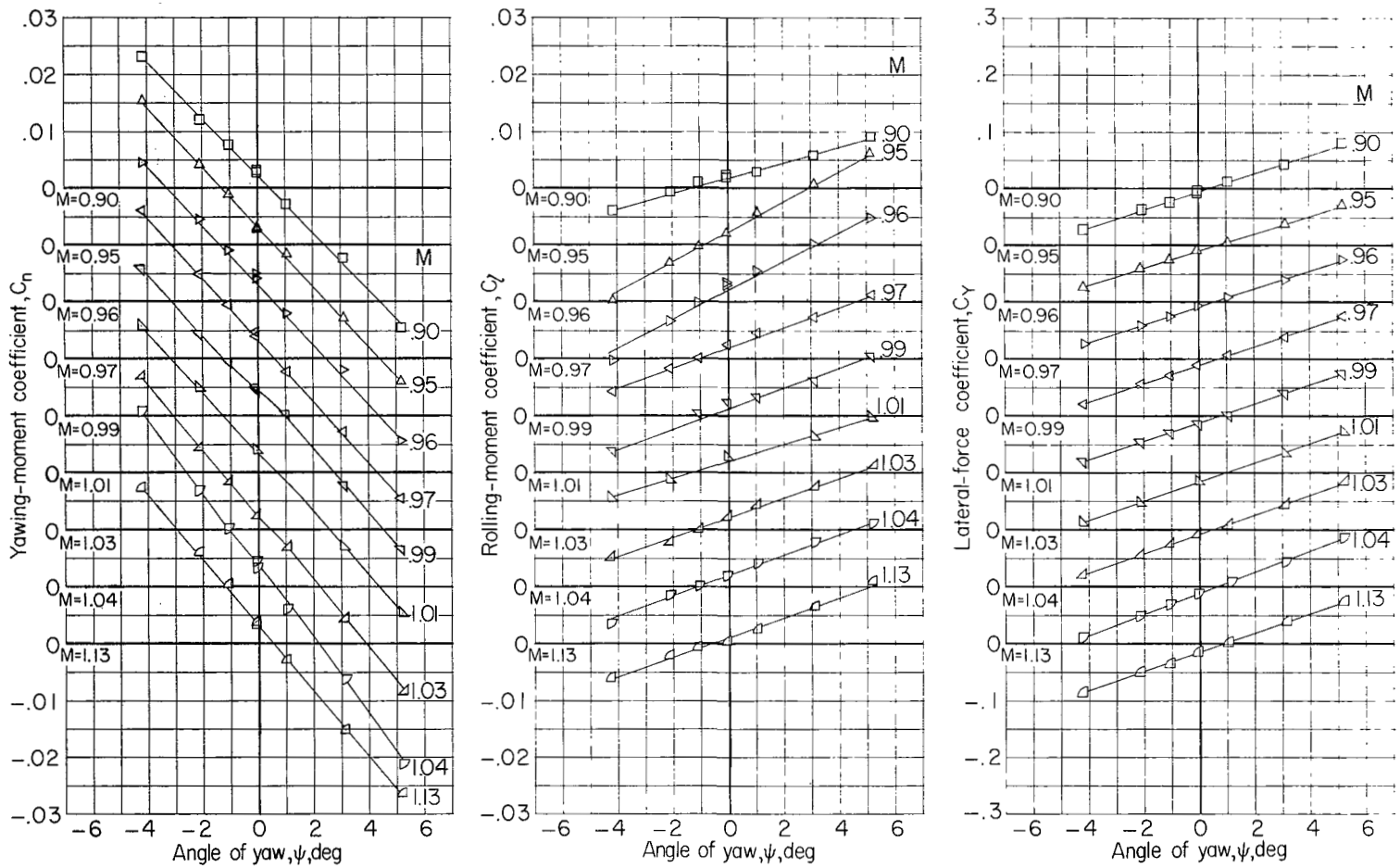


(a) Yawing-moment, rolling-moment, and lateral-force coefficients.

Figure 12.- Variation of aerodynamic characteristics with angle of yaw. Complete model plus small end plates on wing tips $\left(N^{1}B^{3}W^{1A}E^{1}H_{O}{}^{1}V\right)$; $\alpha = -0.2^{\circ}$.

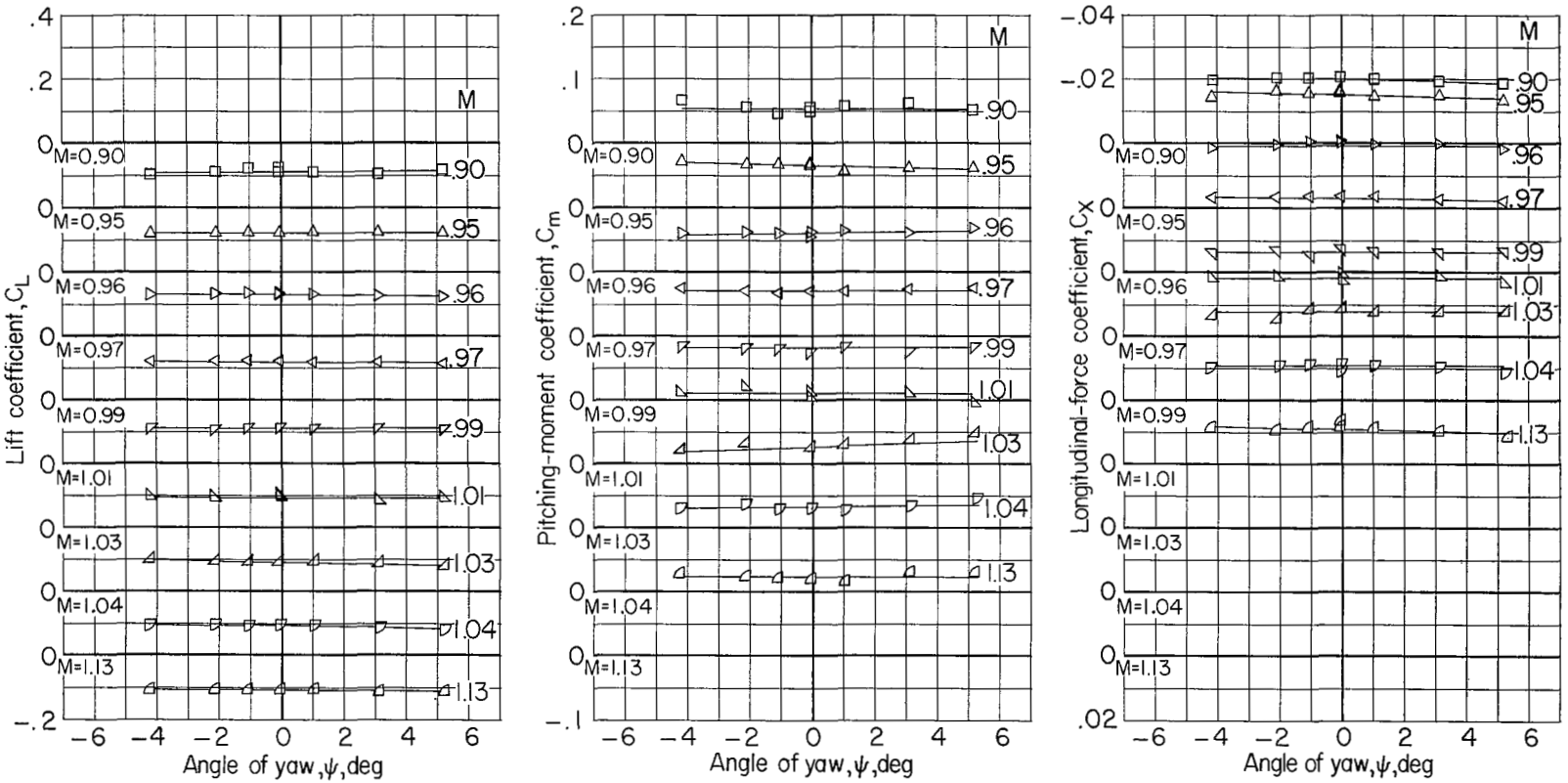


(b) Lift, pitching-moment, and longitudinal-force coefficients.

Figure 12.- Concluded.

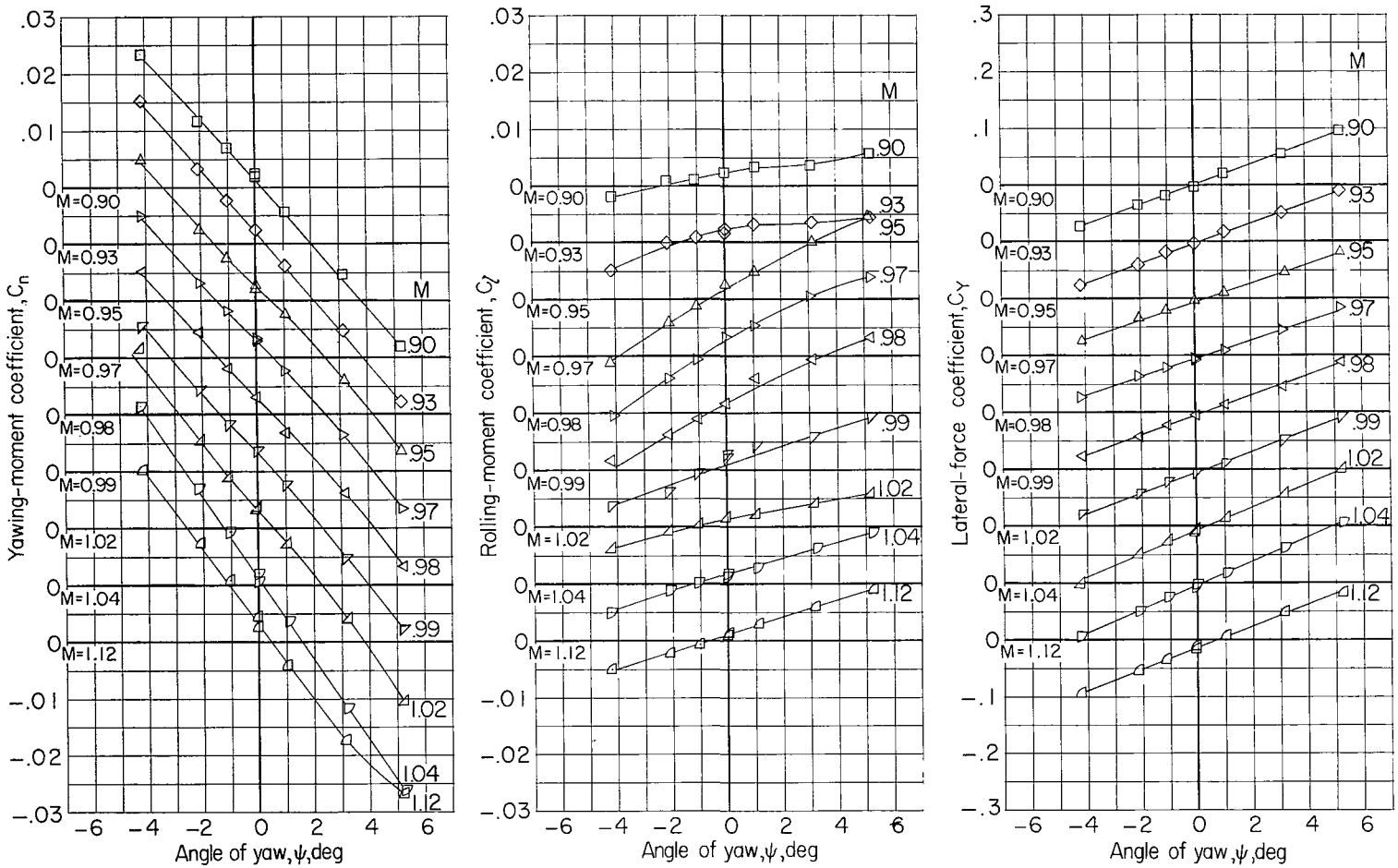


(a) Yawing-moment, rolling-moment, and lateral-force coefficients.

Figure 13.- Variation of aerodynamic characteristics with angle of yaw. Complete model plus large end plates on wing tips $\left(N^1B^3W^1A_E{}^2H_o{}^1V\right)$; $\alpha = -0.2^\circ$.

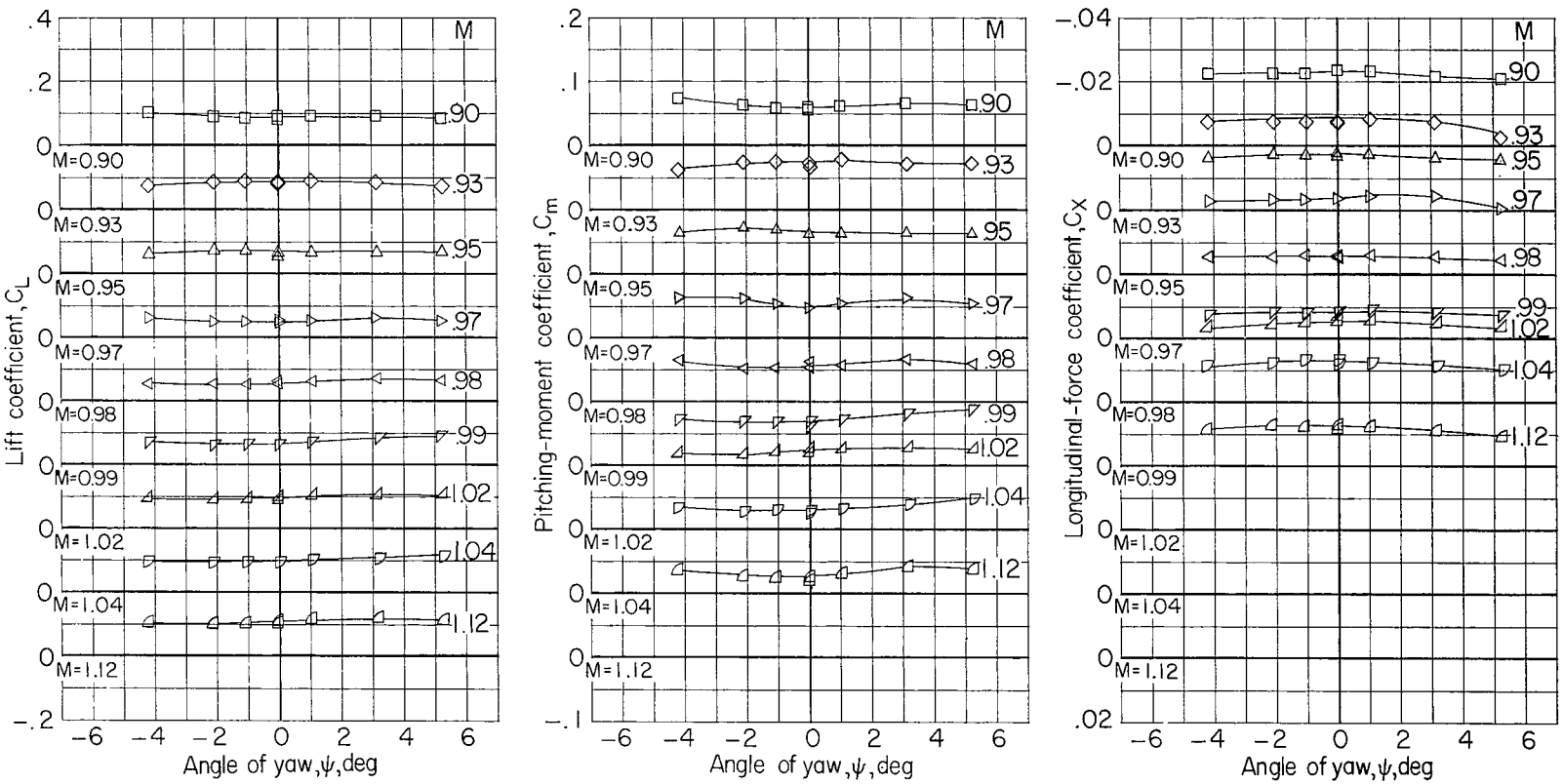


(b) Lift, pitching-moment; and longitudinal-force coefficients.

Figure 13.- Concluded.

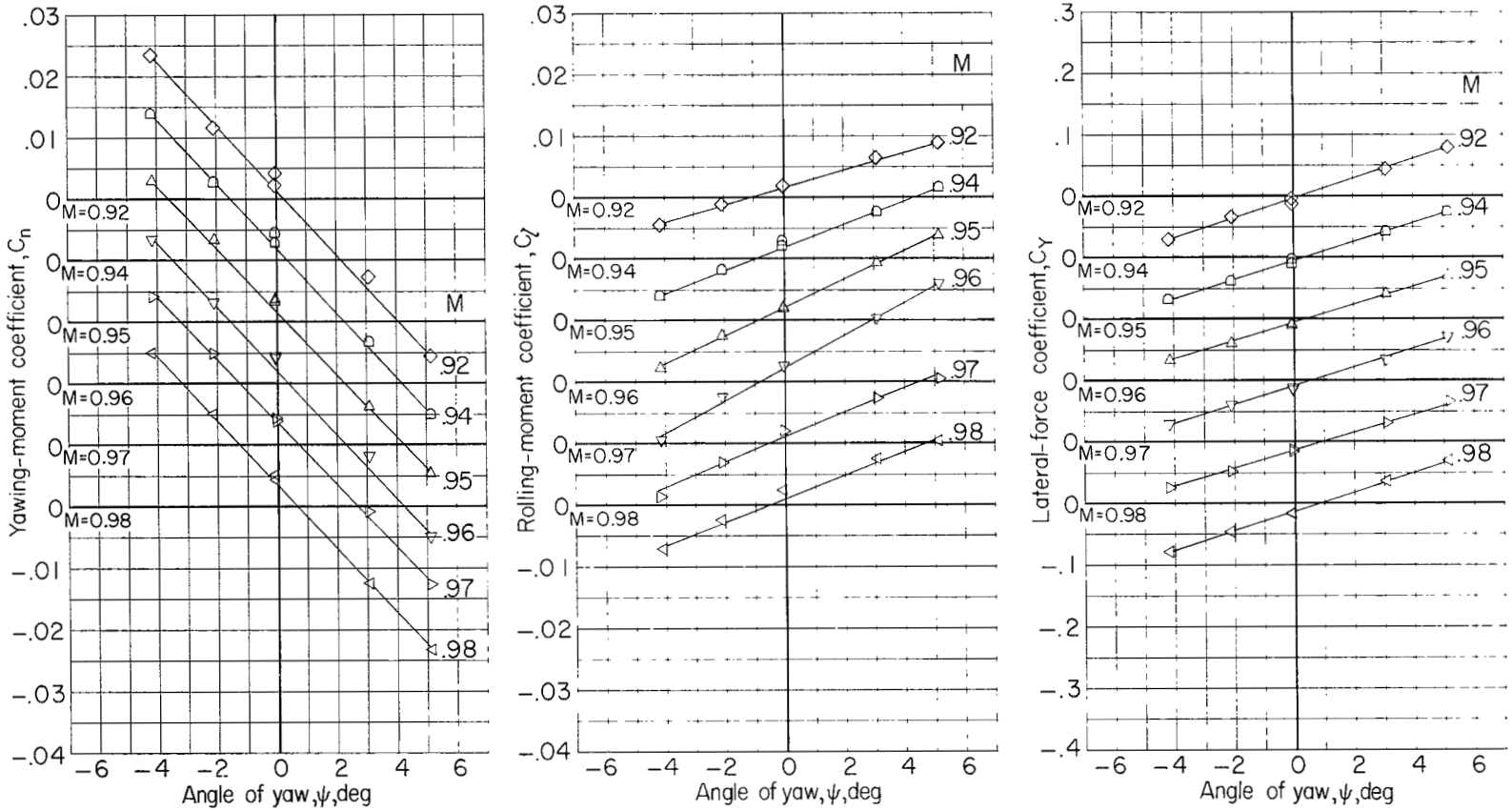


(a) Yawing-moment, rolling-moment, and lateral-force coefficients.

Figure 14.- Variation of aerodynamic characteristics with angle of yaw. Complete model less radar and control-cable housings and plus small end plates on wing tips $\left(N^1B^1W^{1A}E^1H_O{}^1V\right)$; $\alpha = -0.2^\circ$.

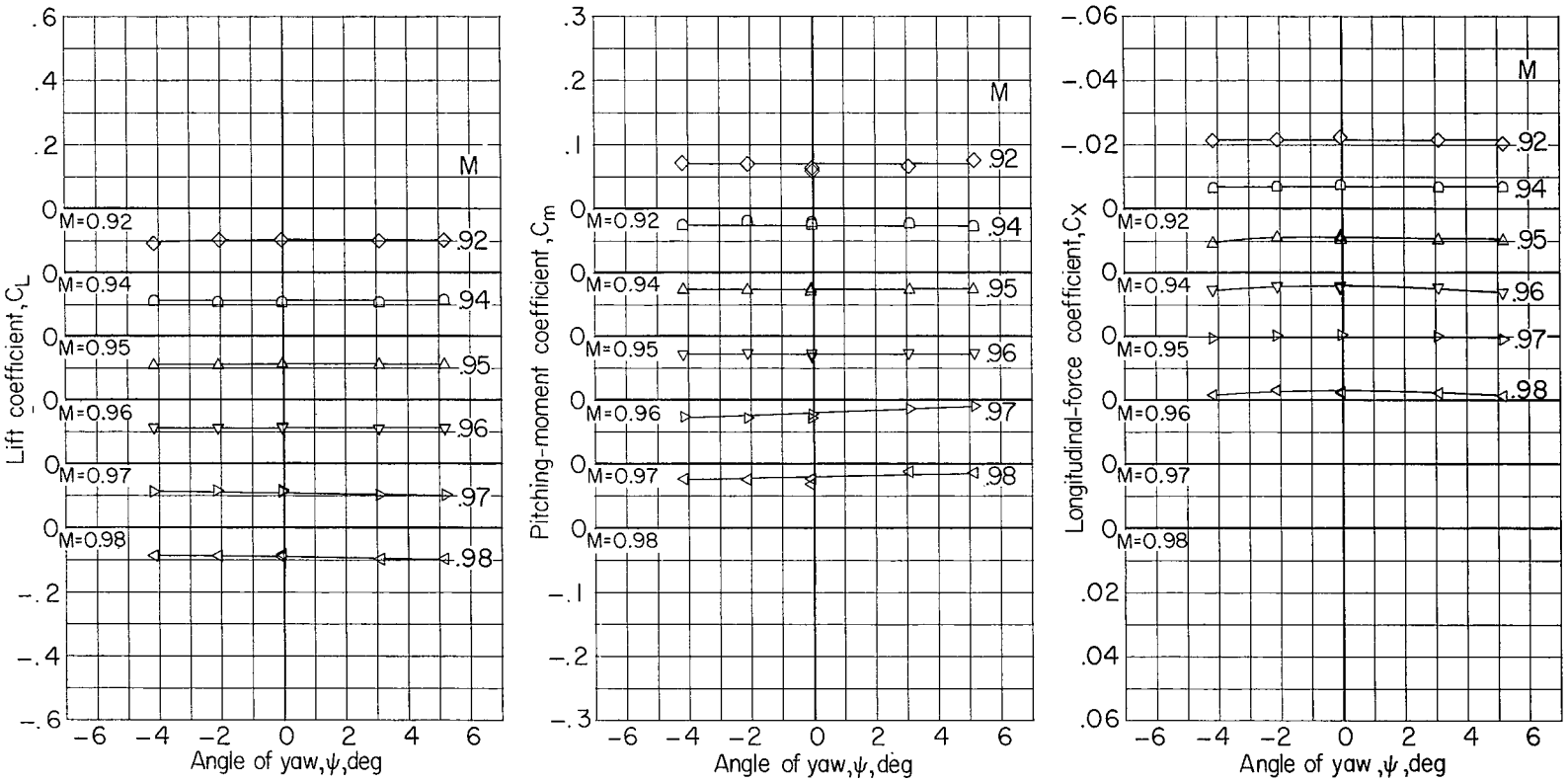


(b) Lift, pitching-moment, and longitudinal-force coefficients.

Figure 14.- Concluded.

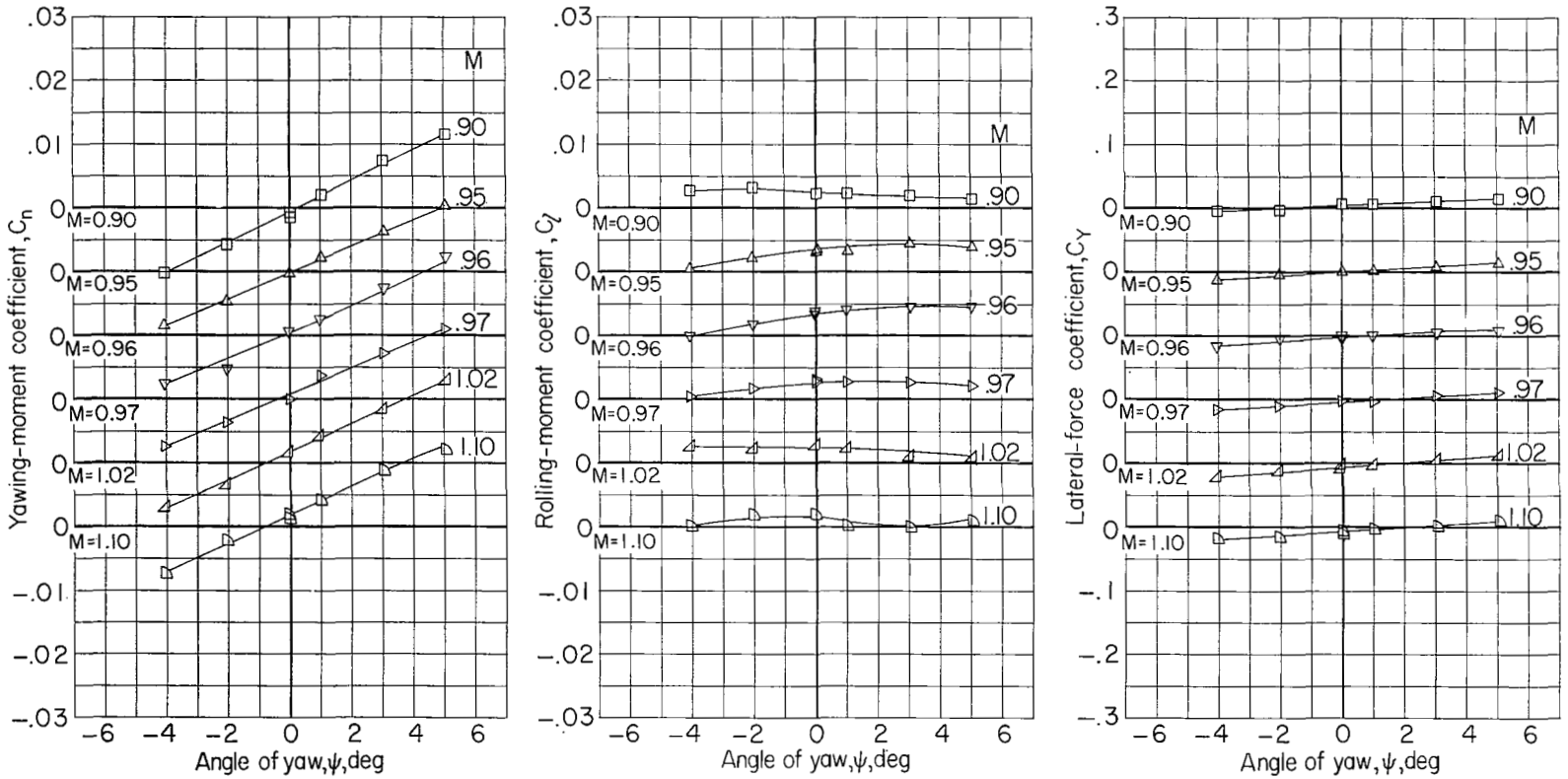


(a) Yawing-moment, rolling-moment, and lateral-force coefficients.

Figure 15.- Variation of aerodynamic characteristics with angle of yaw.

Complete model less tail and less control-cable housing $\left(N^{1}B^{2}W^{1A}\right)$; $\alpha = -0.1^{\circ}$.

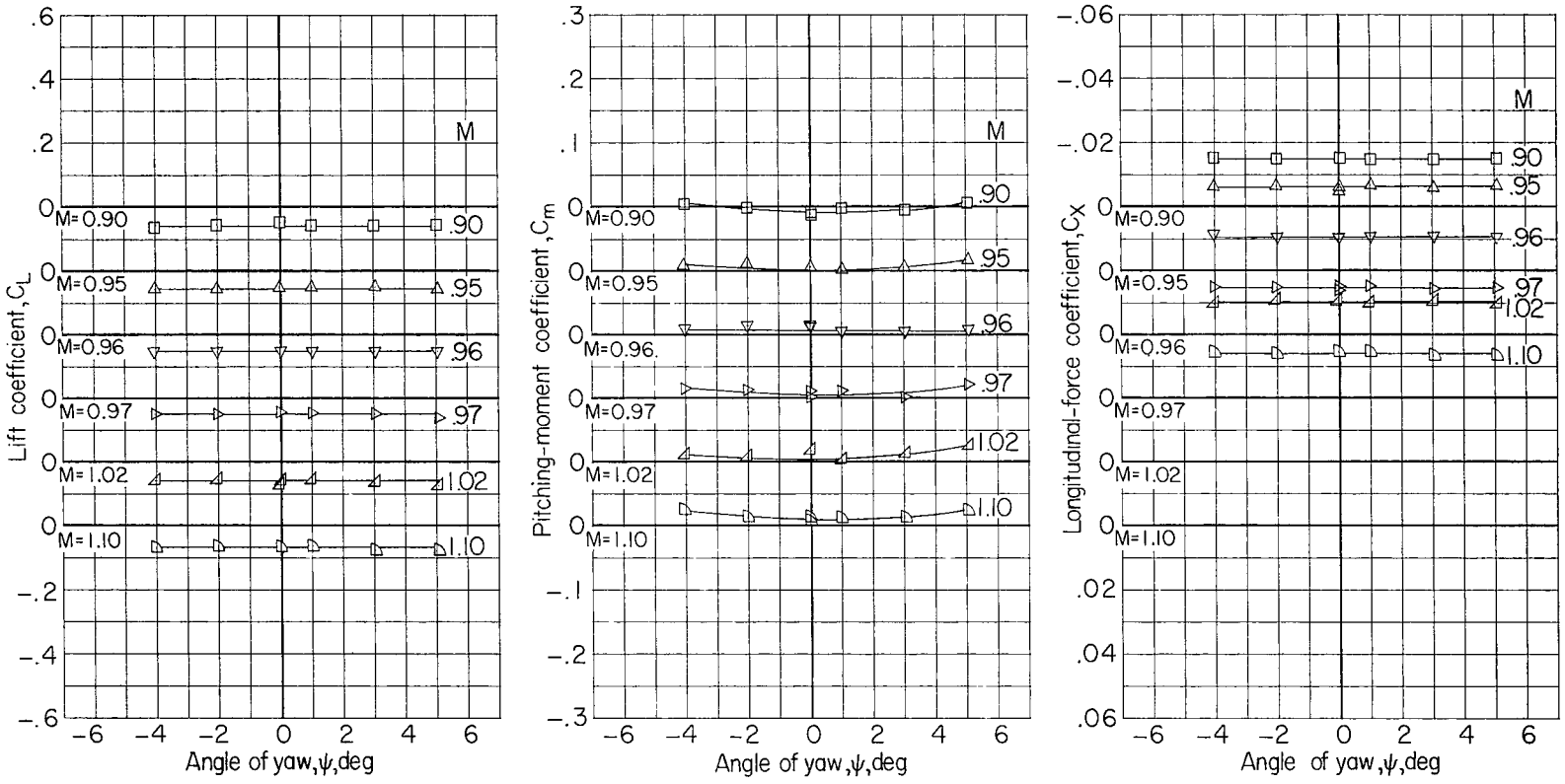


(b) Lift, pitching-moment, and longitudinal-force coefficients.

Figure 15.- Concluded.

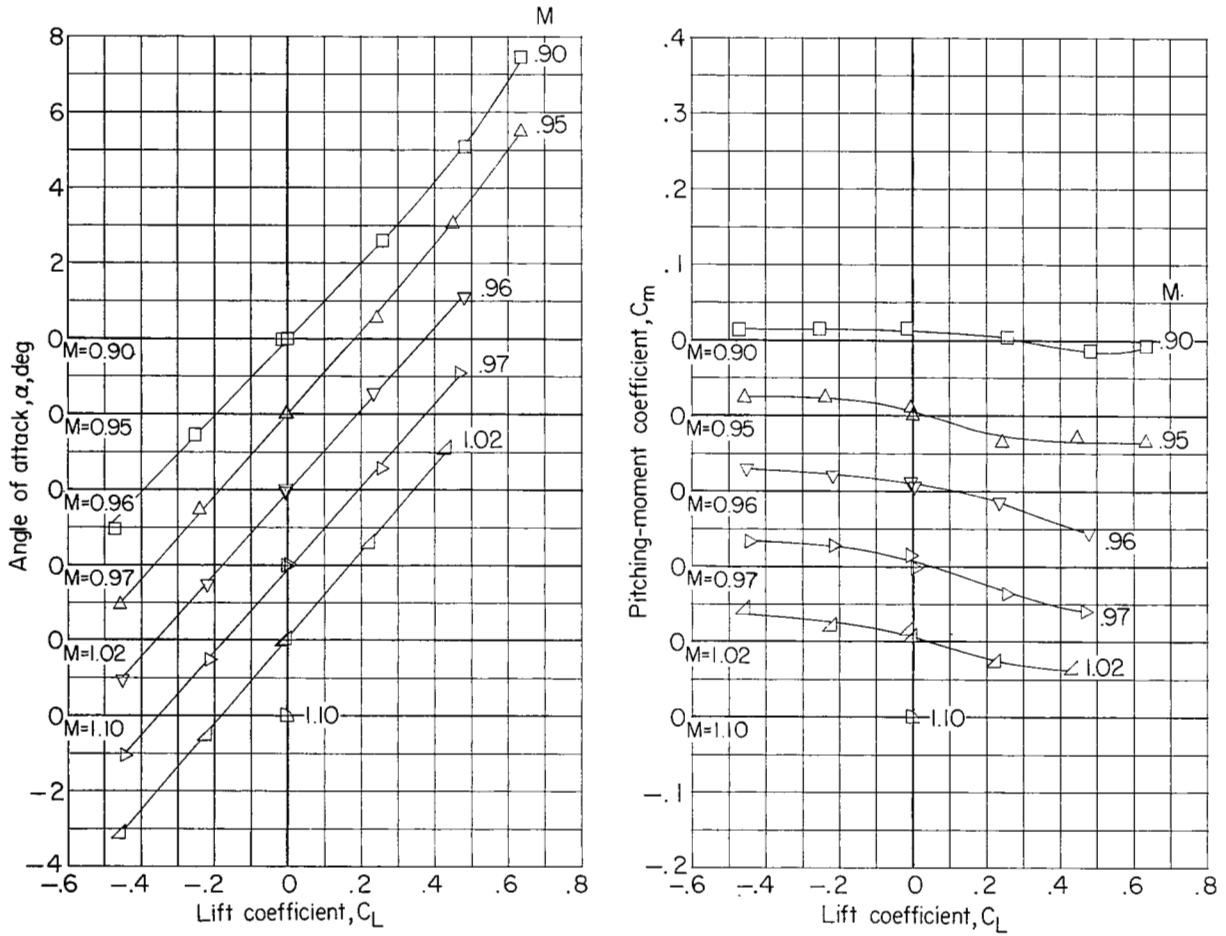


(a) Angle of attack and pitching-moment coefficient.

Figure 16.- Variation of aerodynamic characteristics with lift coefficient (or angle of attack). Complete model less tail and less control-cable housing $\left(N^1B^2W^{1A}\right)$; $\psi = 0^\circ$.

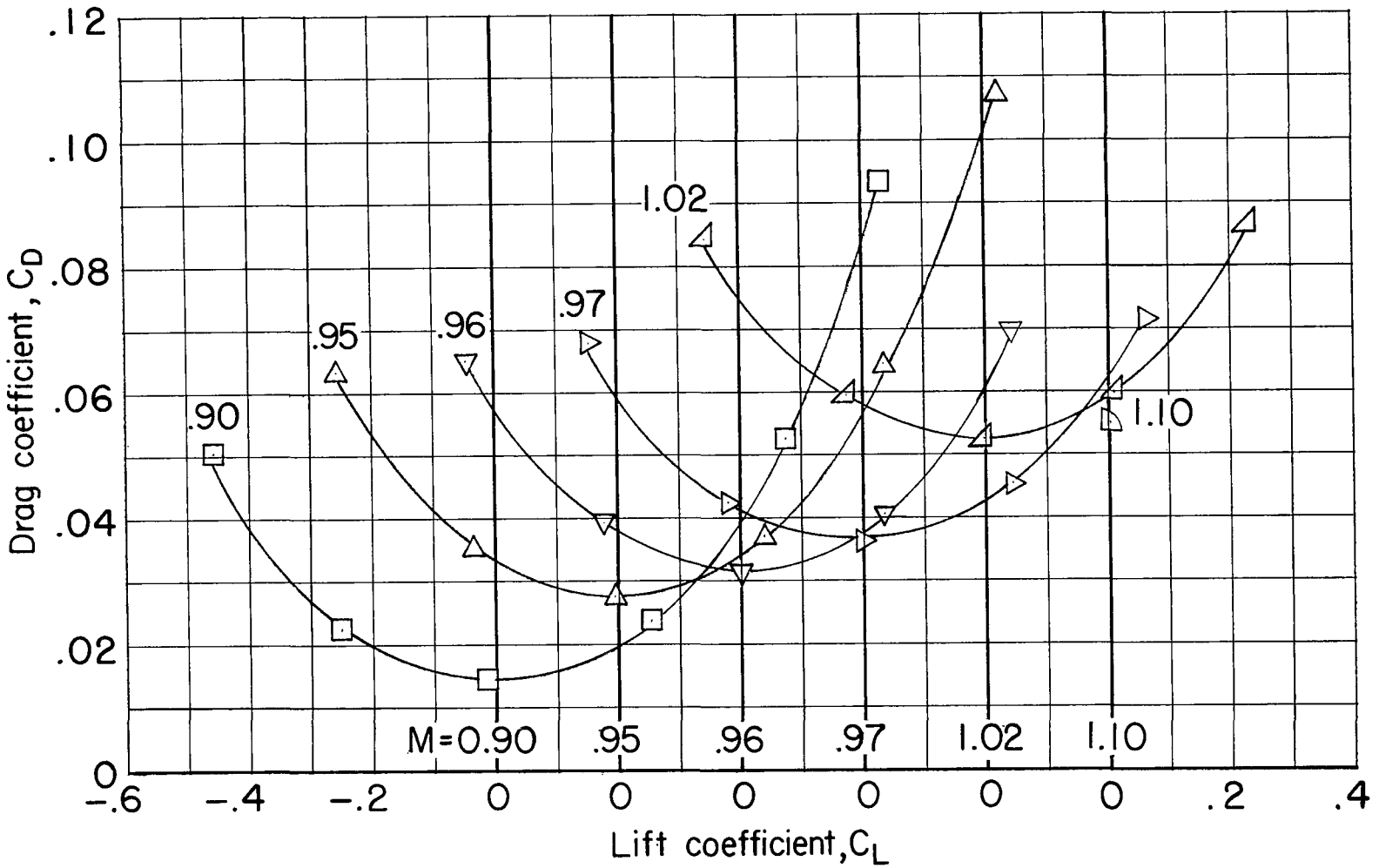


(b) Drag coefficient.

Figure 16.- Continued.

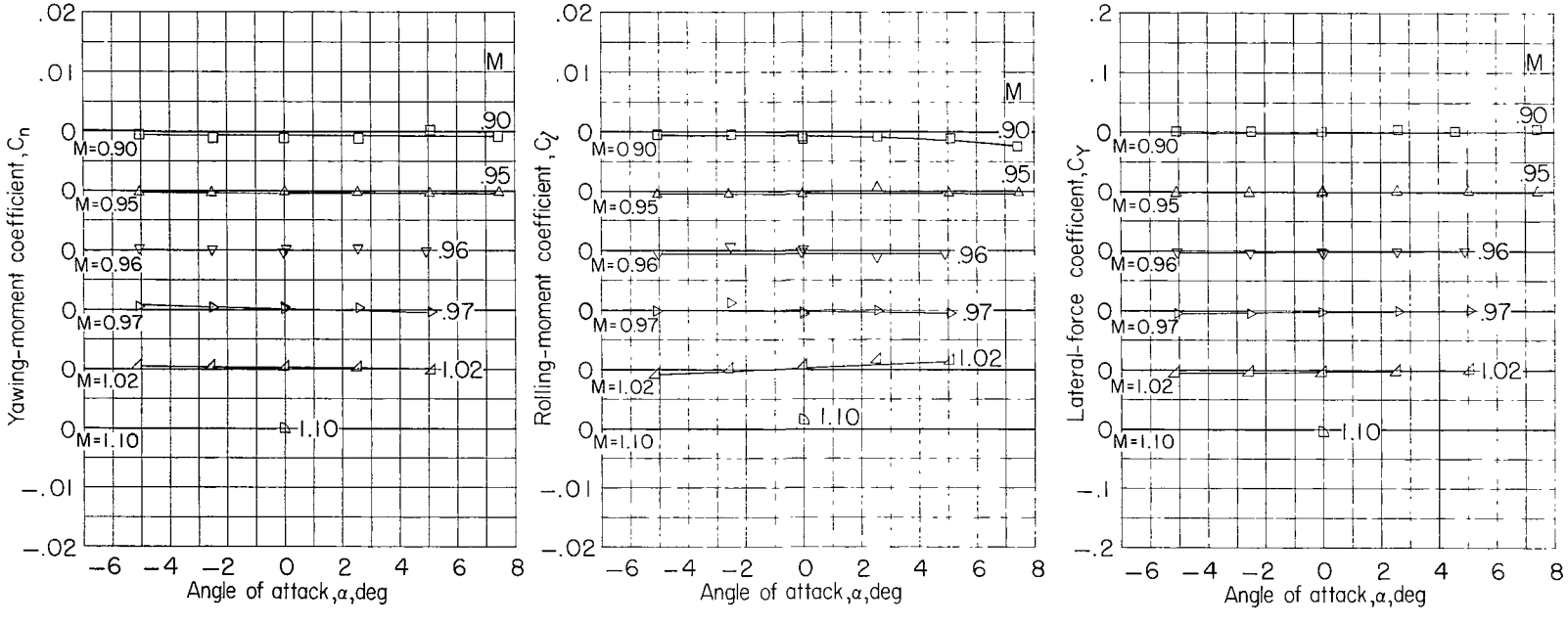


(c) Yawing-moment, rolling-moment, and lateral-force coefficients.

Figure 16.- Concluded.

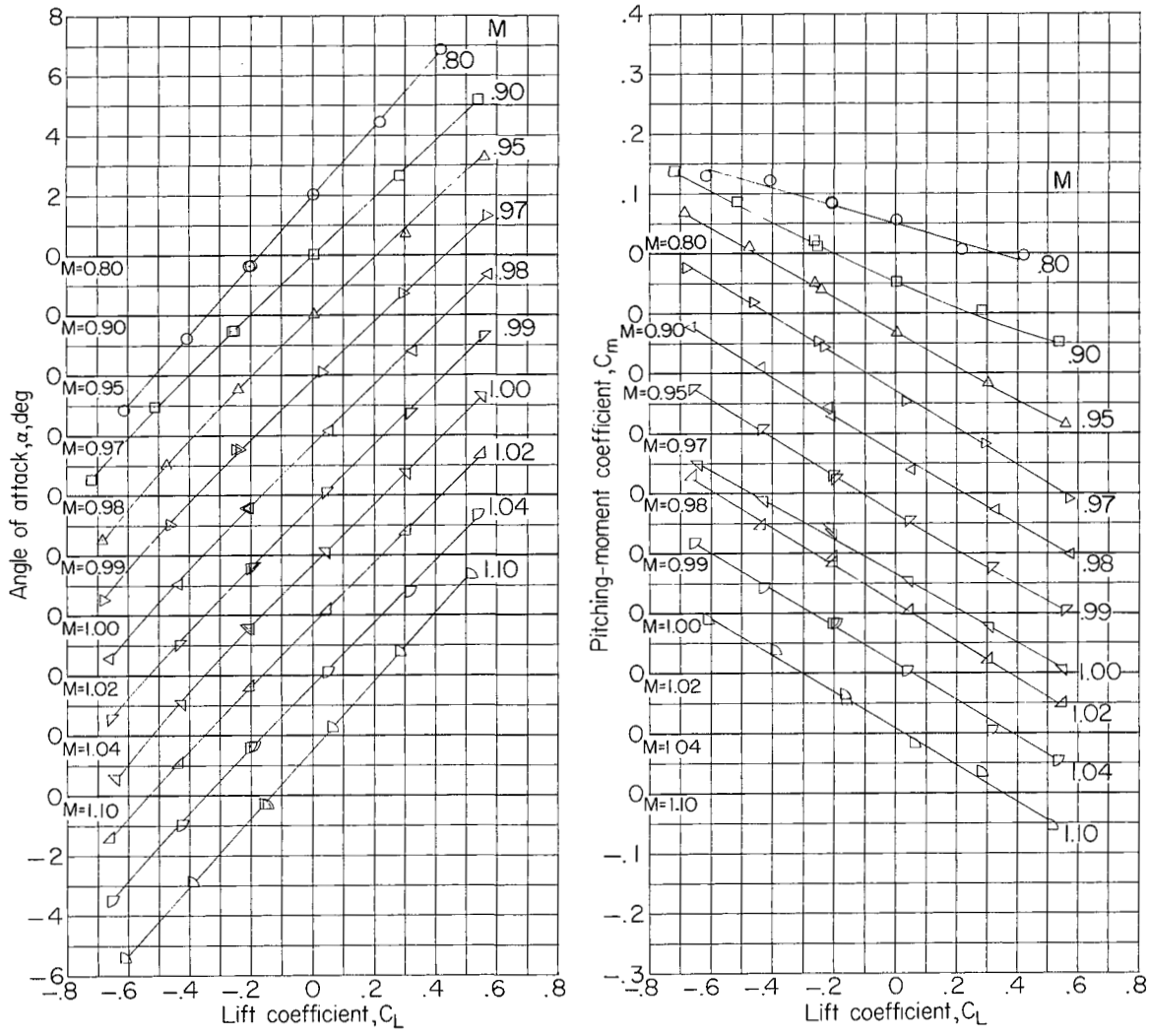


(a) Angle of attack and pitching-moment coefficient.

Figure 17.- Variation of aerodynamic characteristics with lift coefficient (or angle of attack). Complete model plus spoiler $\left(N^1B^3W^1A_{H_O}{}^1VS^1\right)$; $\psi = 0^\circ$. Spoiler mounted on upper surface of left semispan of wing.

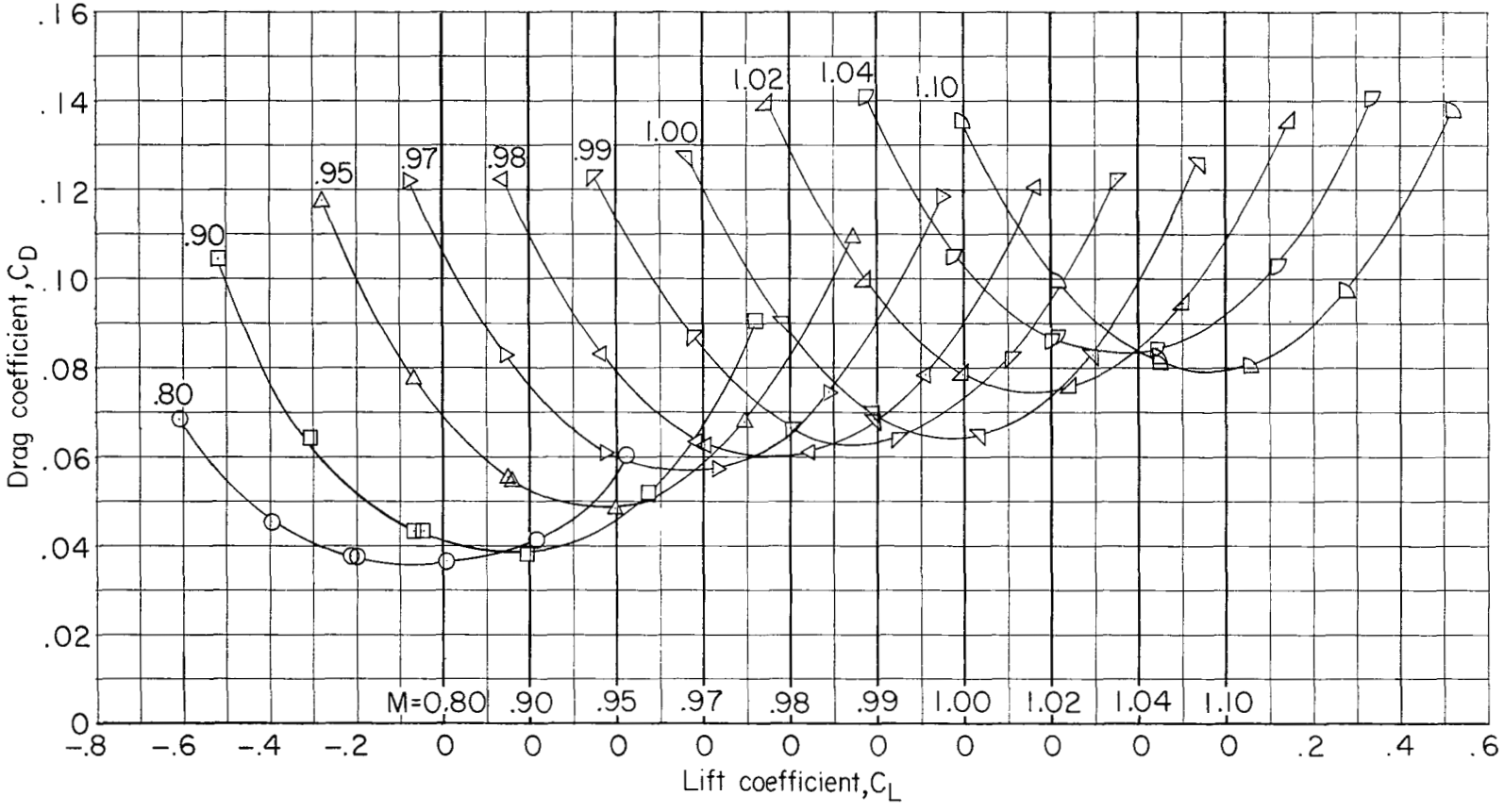


(b) Drag coefficient.

Figure 17.- Continued.

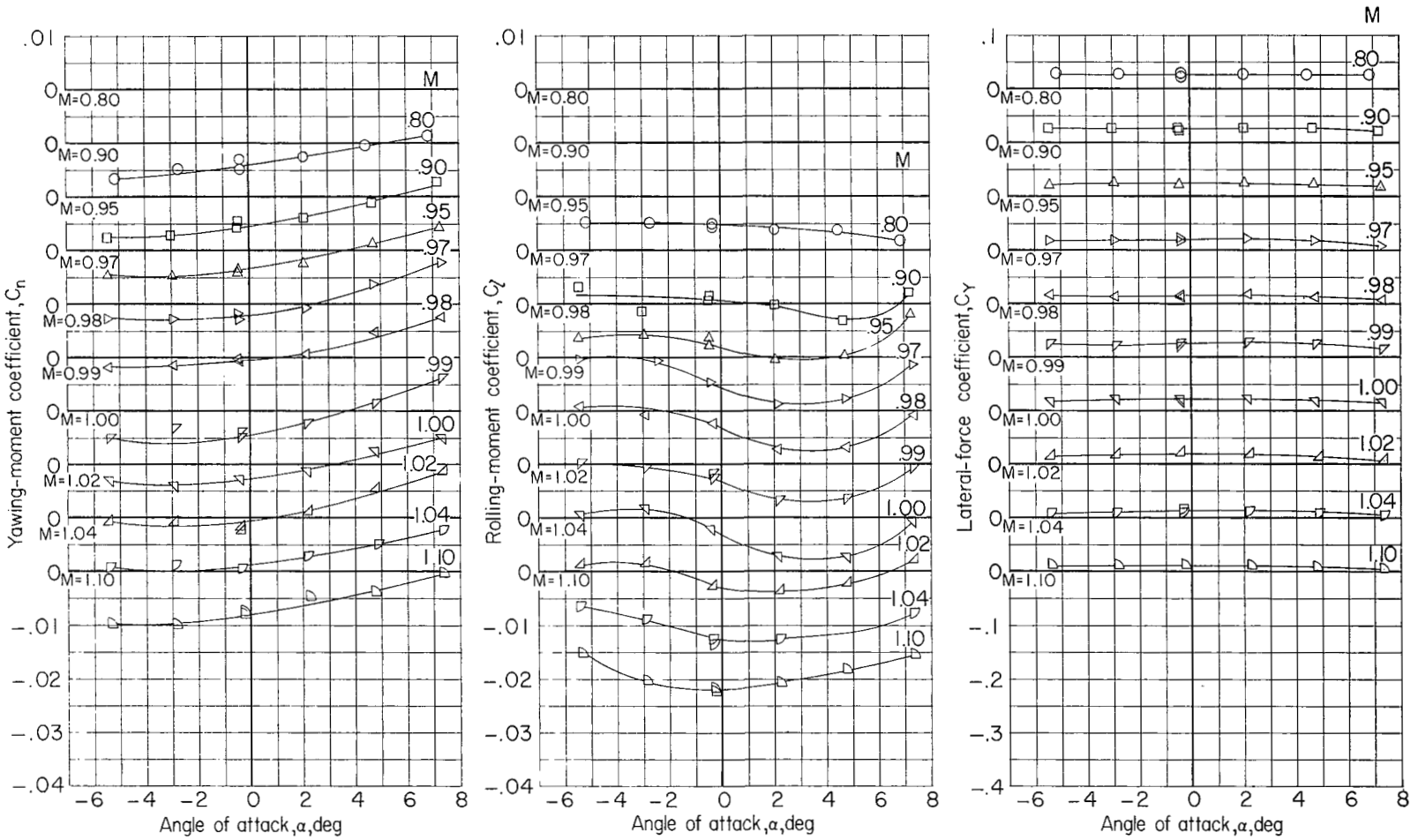


(c) Yawing-moment, rolling-moment, and lateral-force coefficients.

Figure 17.- Concluded.

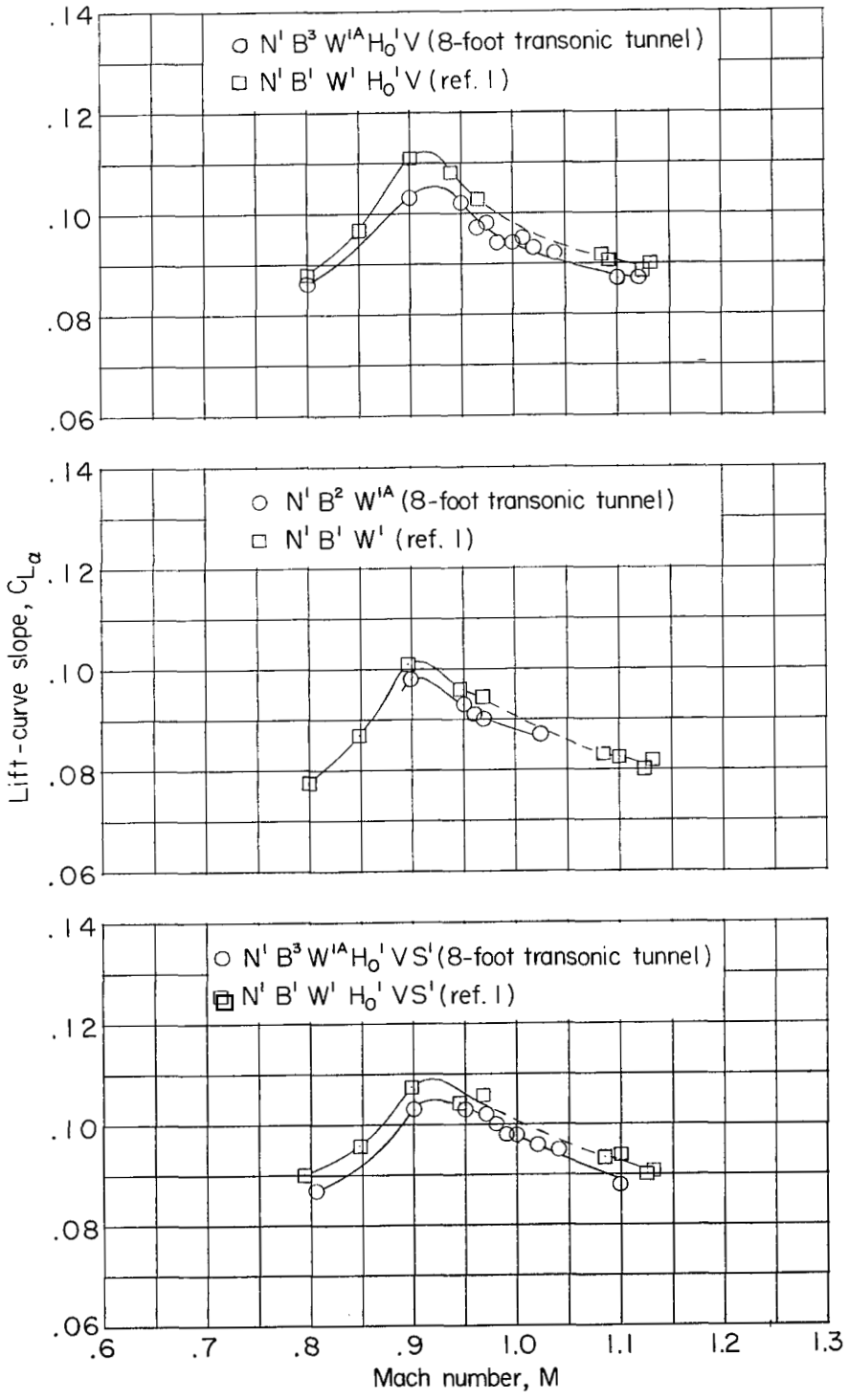


Figure 18.- Variation of lift-curve slope with Mach number. Complete model; complete model less tail and less control-cable housing; and complete model plus spoiler. $\psi = 0^{\circ}$; $\alpha \approx 0^{\circ}$.

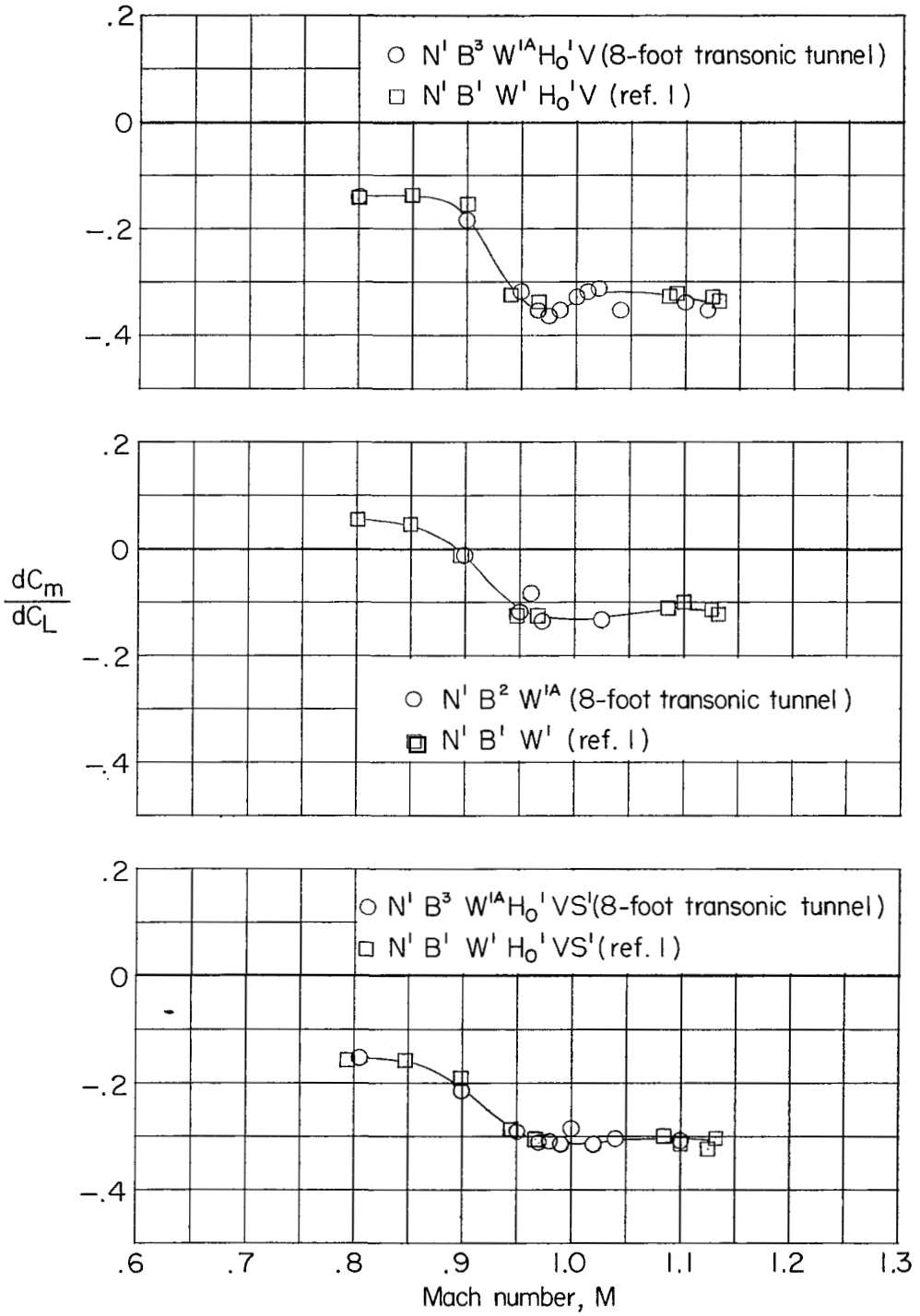


Figure 19.- Variation of static longitudinal-stability derivative with Mach number. Complete model; complete model less tail and less control-cable housing; and complete model plus spoiler. $\psi = 0^{\circ}$; $C_L \approx 0$.

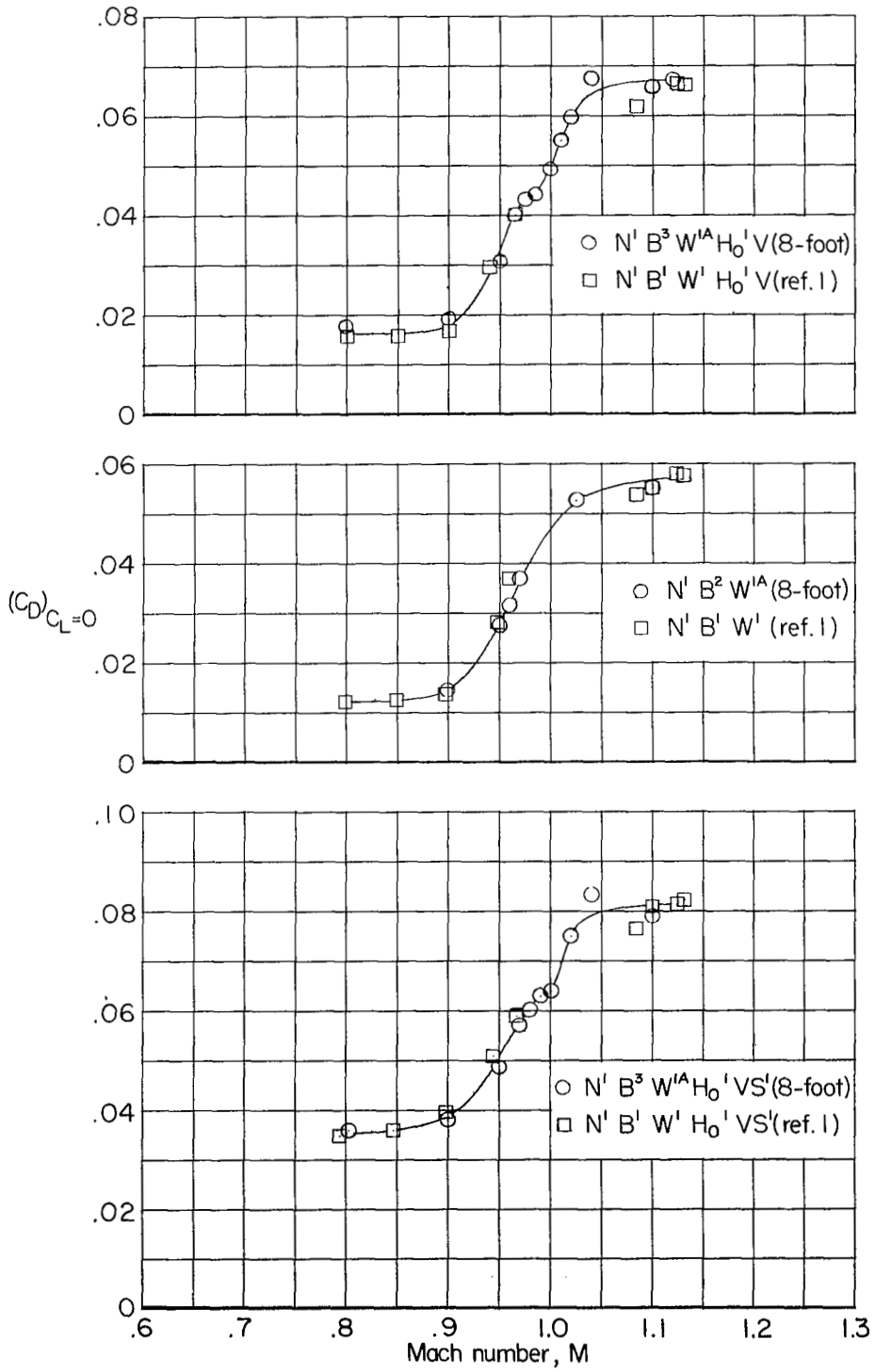


Figure 20.- Variation of zero-lift drag coefficient with Mach number. Complete model; complete model less tail and less control-cable housing; and complete model plus spoiler. $\psi = 0^{\circ}$.

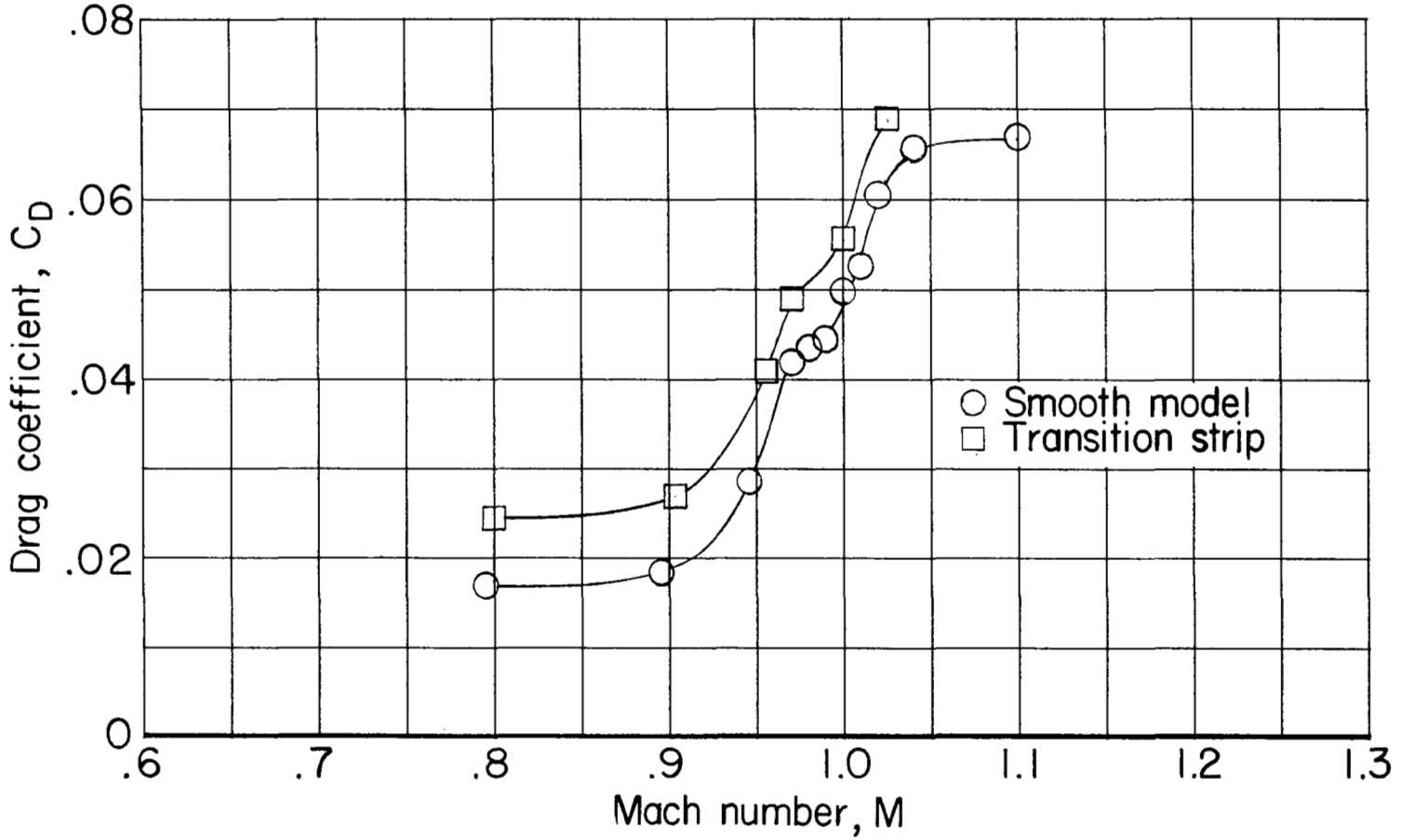


Figure 21.- Effect of transition strip on drag coefficient. Complete model $\left(N^{1}B^{3}W^{1A}H_{o}{}^{1}V\right)$. $\alpha = -0.1^{\circ}$; $\psi = 0^{\circ}$.

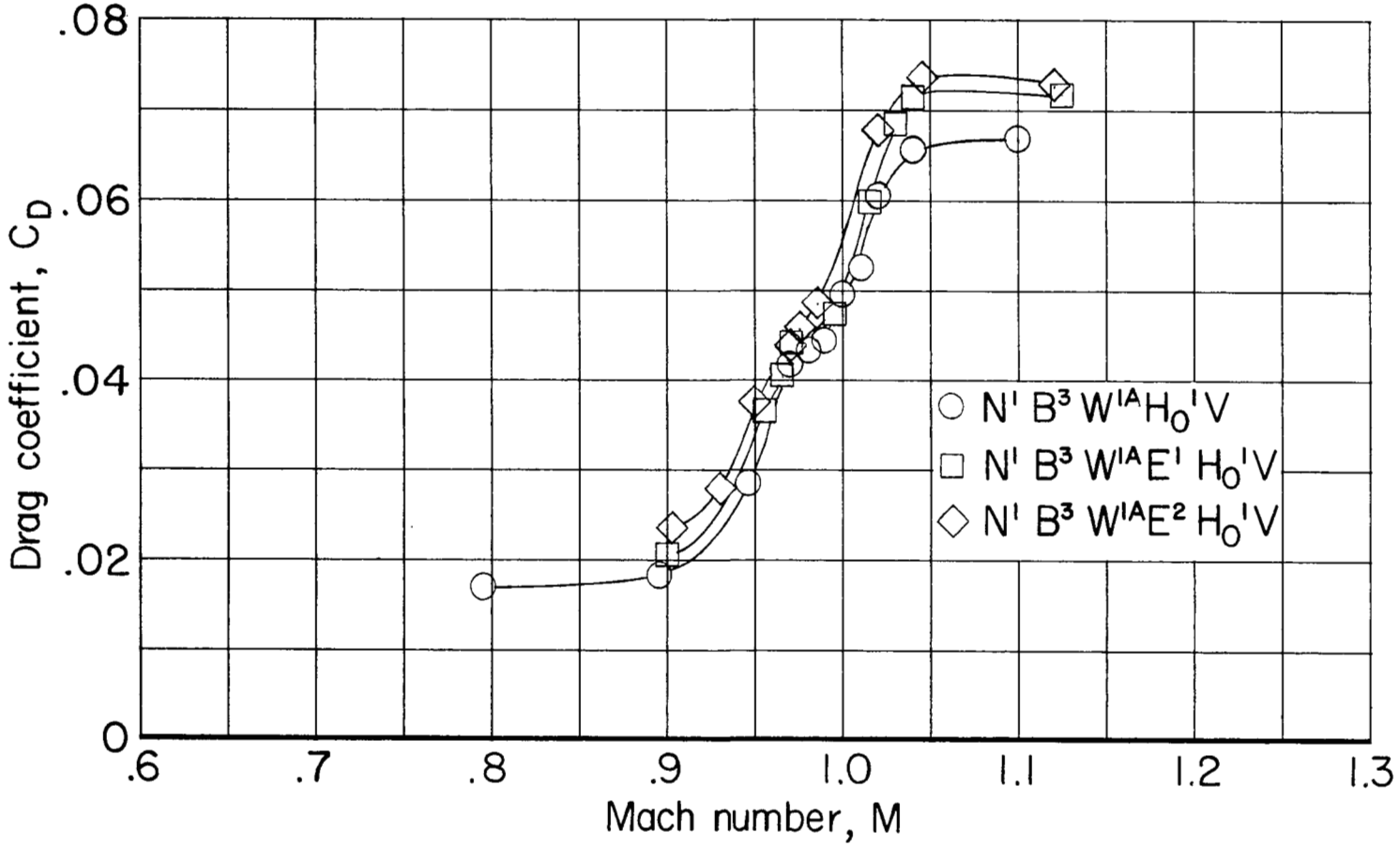


Figure 22.- Effect of end plates located on wing tips on drag coefficient. Complete model. $\alpha \approx 0^\circ$; $\psi = 0^\circ$.

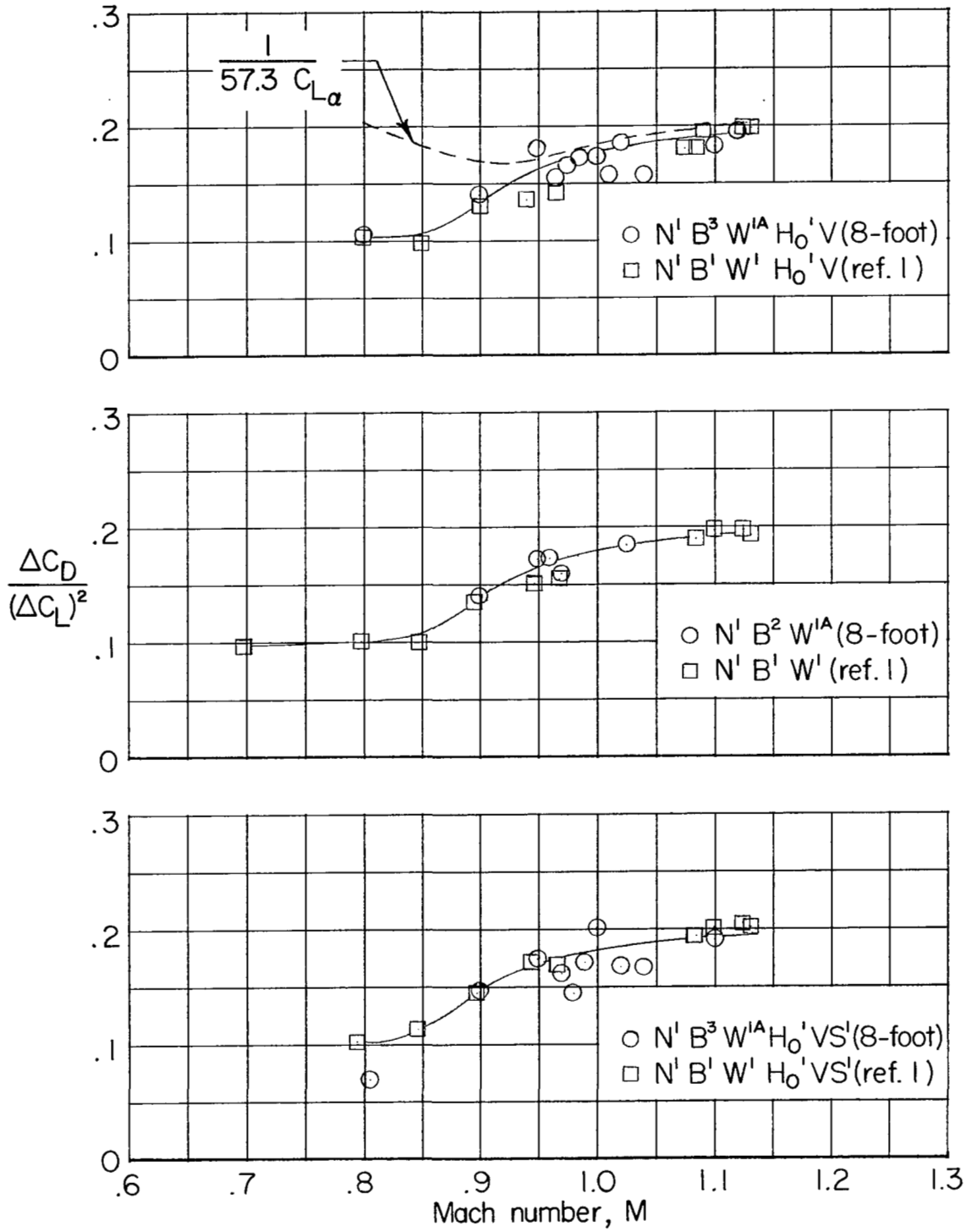


Figure 23.- Variation of drag-rise factor with Mach number. Complete model; complete model less tail and less control-cable housing; and complete model plus spoiler. $\psi = 0^{\circ}$.

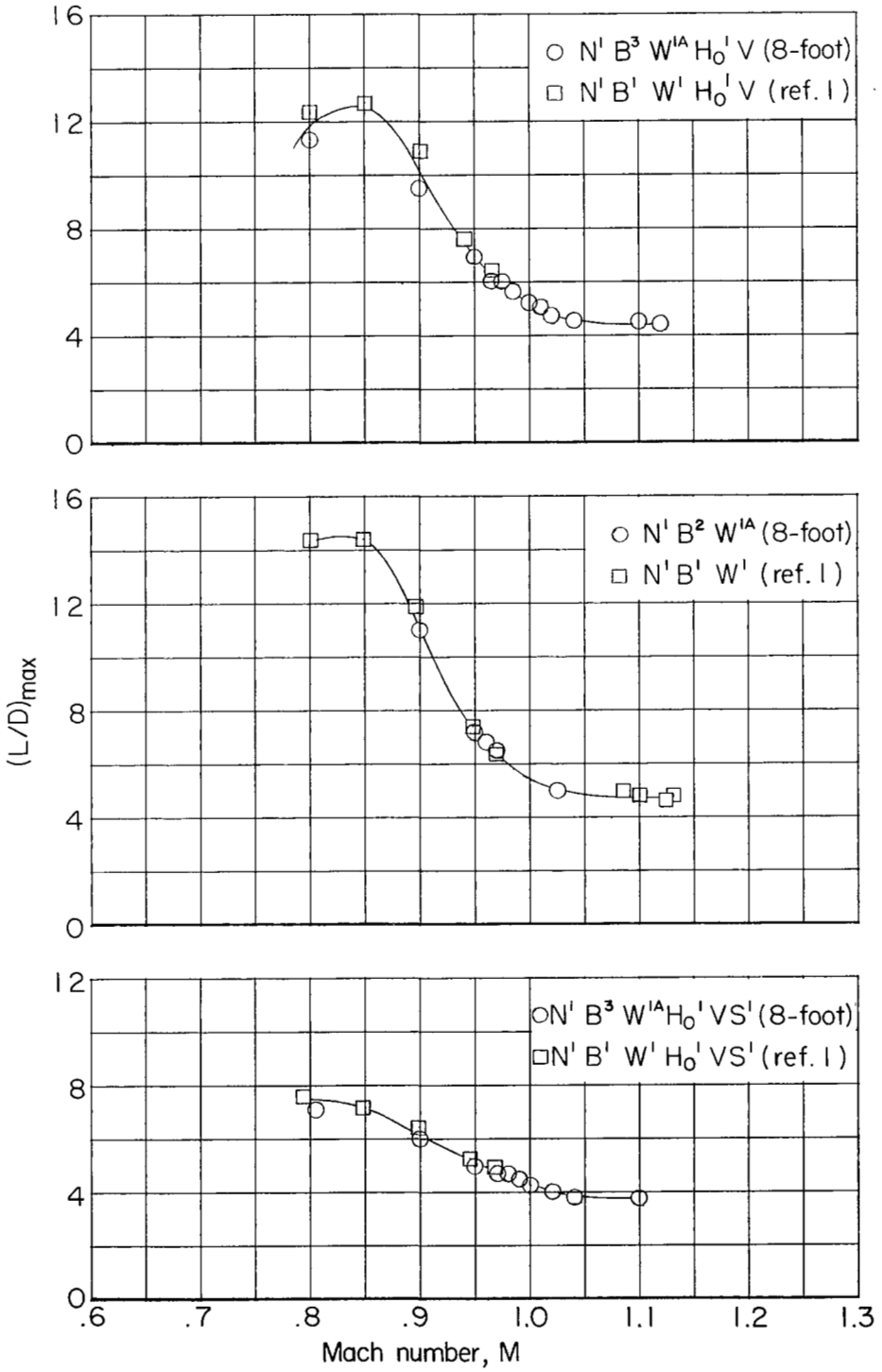


Figure 24.- Variation of maximum lift-drag ratio with Mach number. Complete model; complete model less tail and less control-cable housing; and complete model plus spoiler. $\psi = 0^{\circ}$.

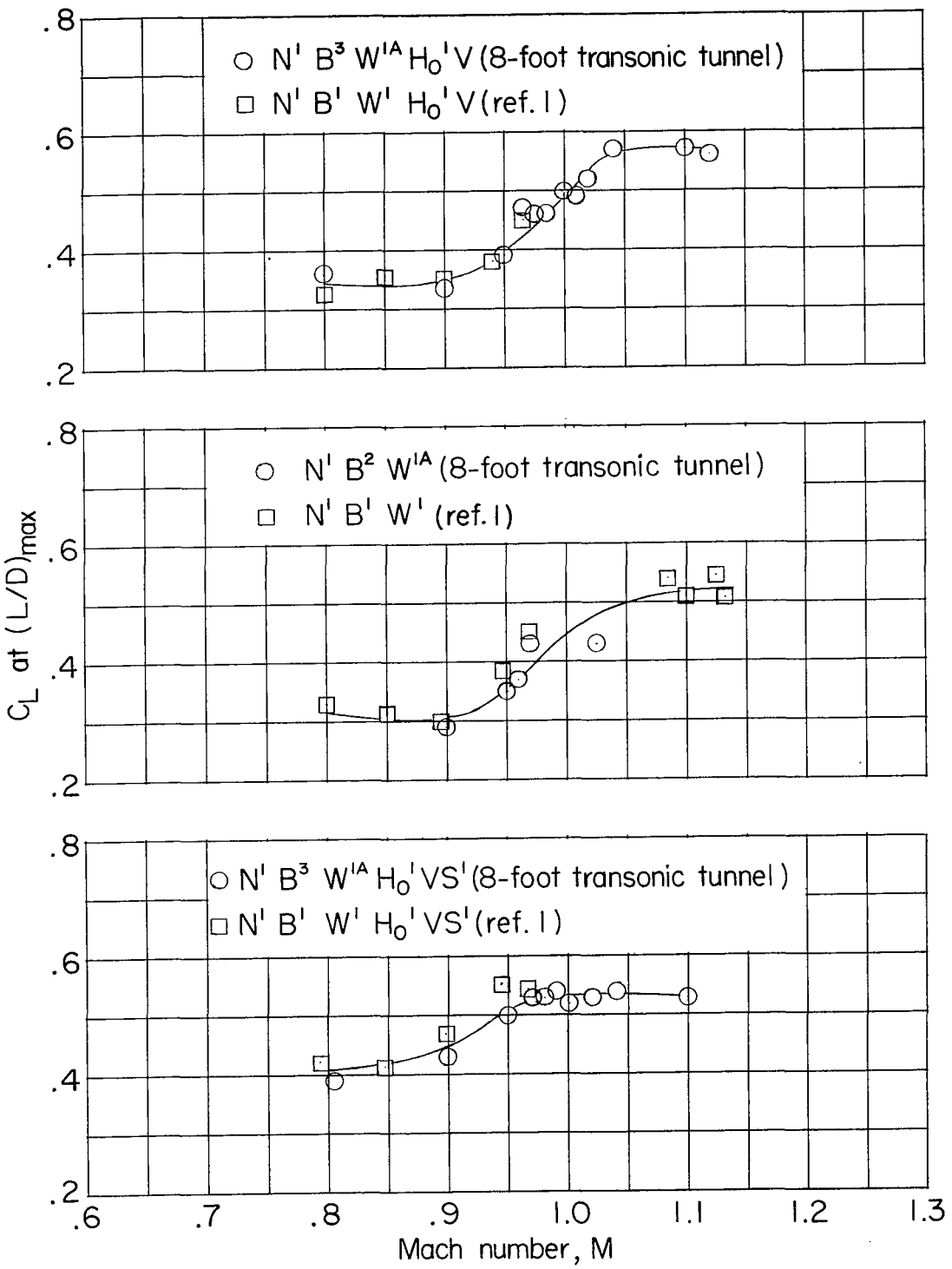


Figure 25.- Variation with Mach number of lift coefficient corresponding to maximum lift-drag ratio. Complete model; complete model less tail less control-cable housing; and complete model plus spoiler. $\psi = 0^{\circ}$.

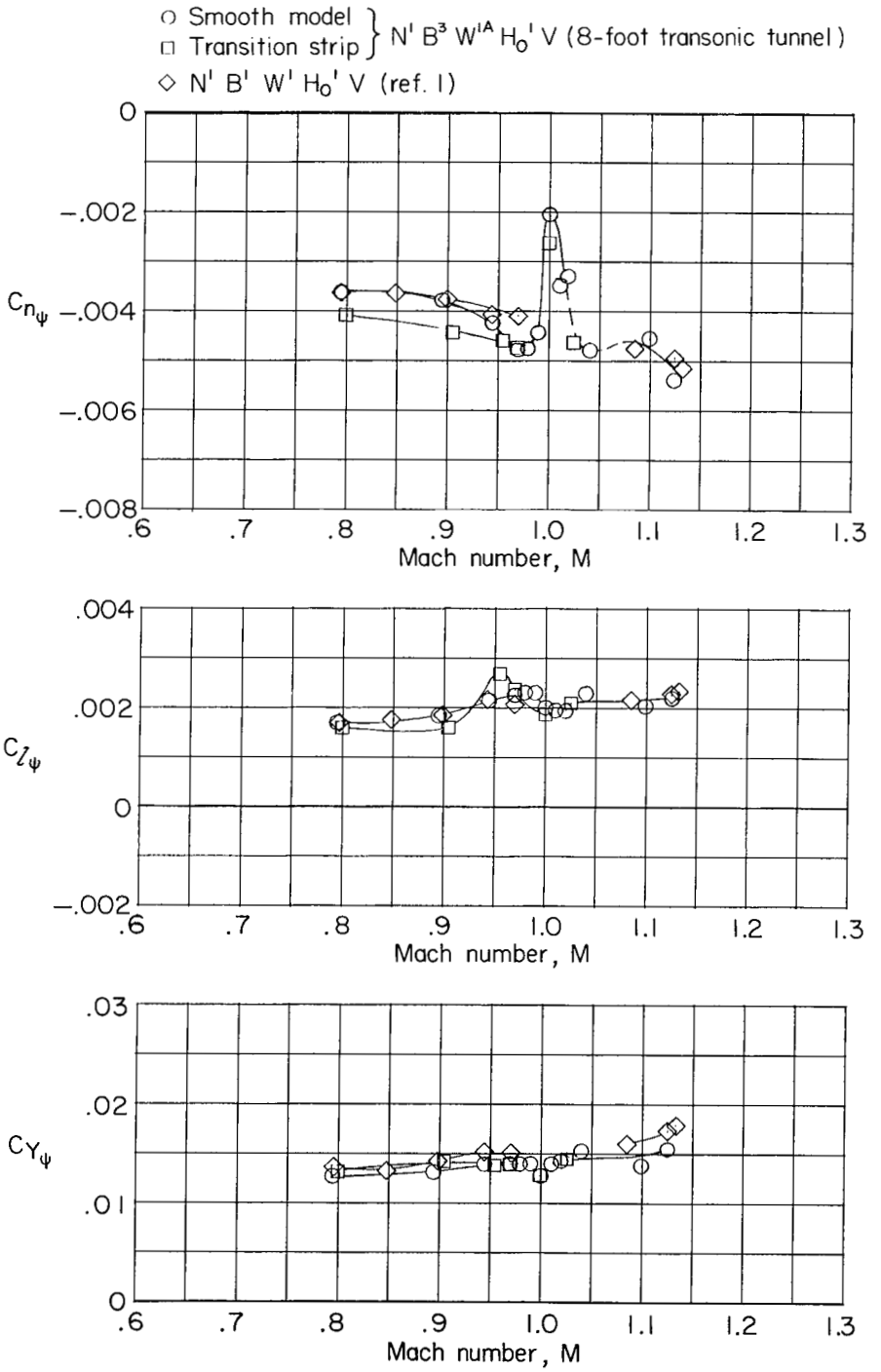


(a) $\alpha \approx 0^\circ$.

Figure 26.- Variation of lateral-stability derivatives with Mach number. Complete model; $\psi \approx 0^\circ$.

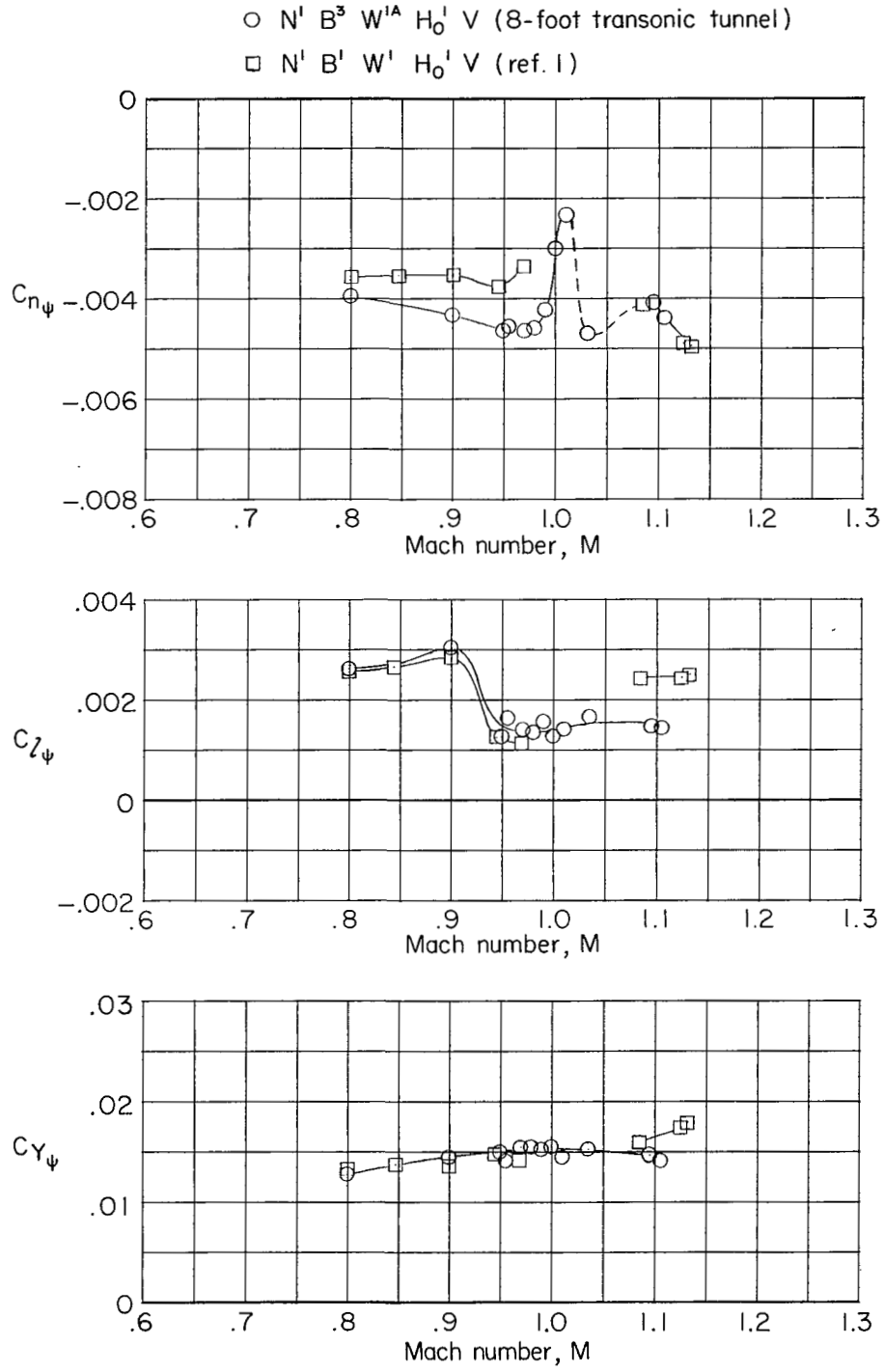


(b) $\alpha = 2.7^\circ$ for 8-foot transonic tunnel tests;
$\alpha \approx 2.2^\circ$ for reference 1 tests.

Figure 26.- Concluded.

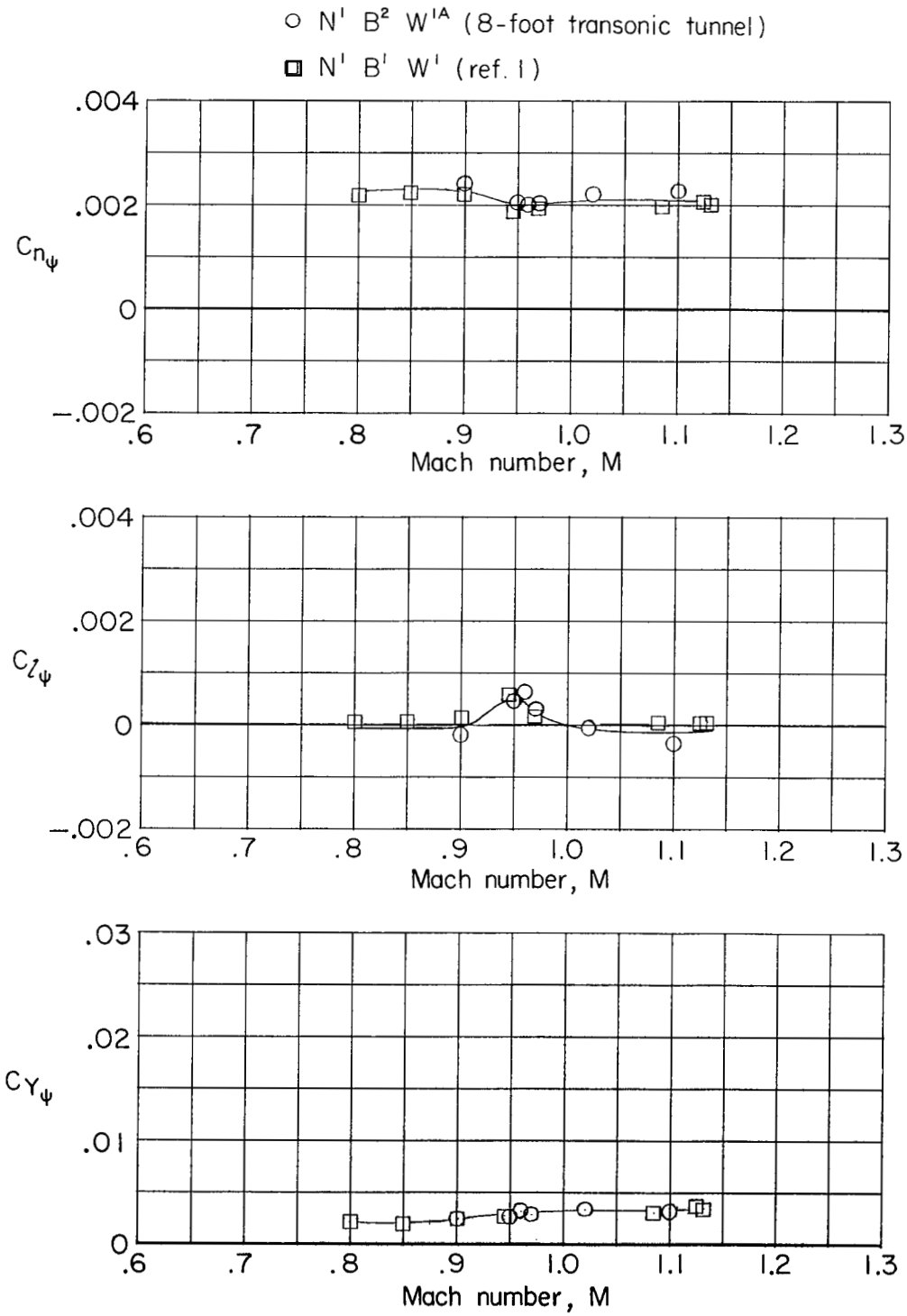


Figure 27.- Variation of static lateral-stability derivatives with Mach number. Complete model less tail and less control-cable housing. $\psi \approx 0^\circ$; $\alpha \approx 0^\circ$.

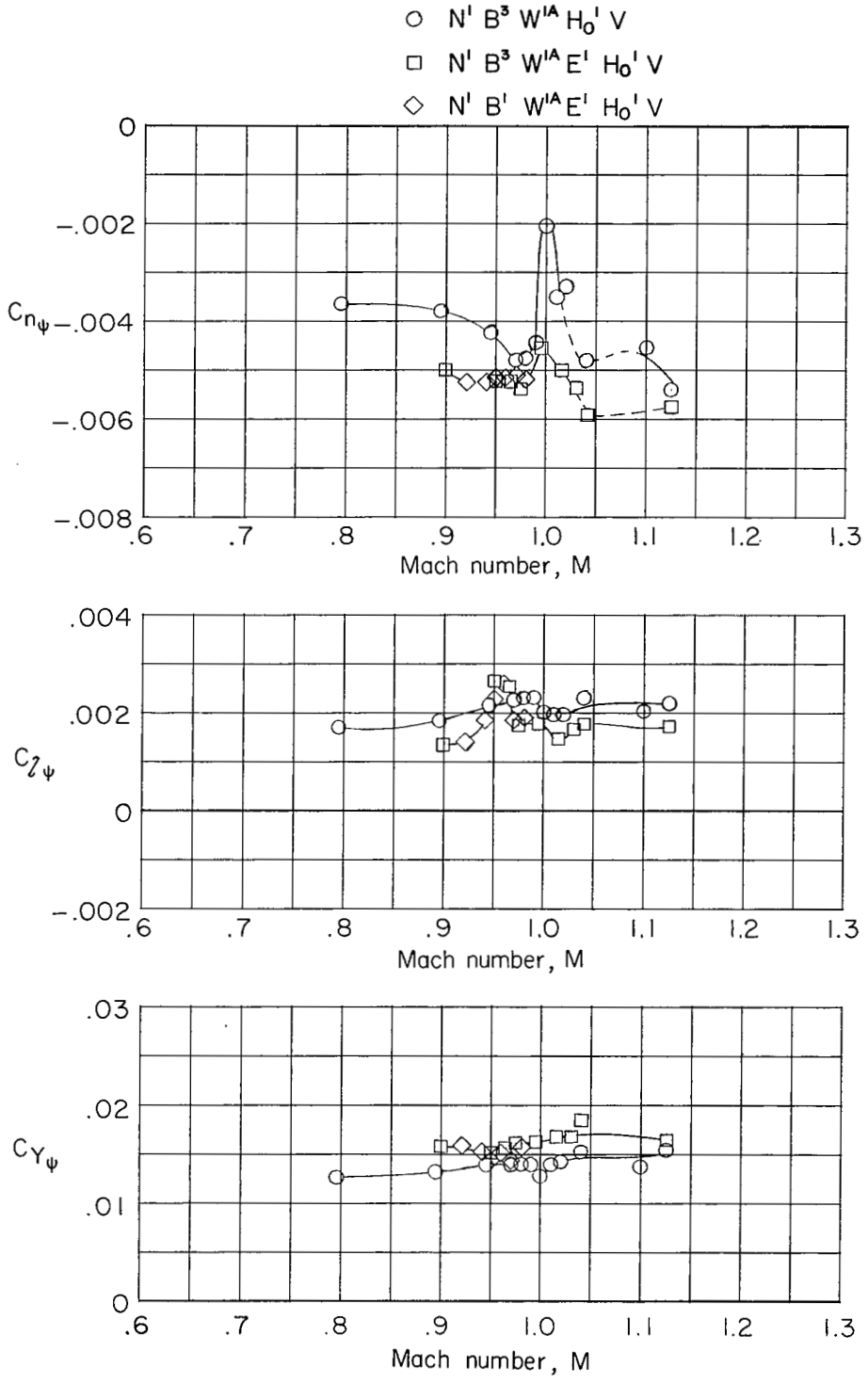


Figure 28.- Effect of small end plates located on wing tips on lateral-stability derivatives. Complete model and complete model less radar and control-cable housings. $\psi \approx 0^\circ$; $\alpha = -0.2^\circ$.

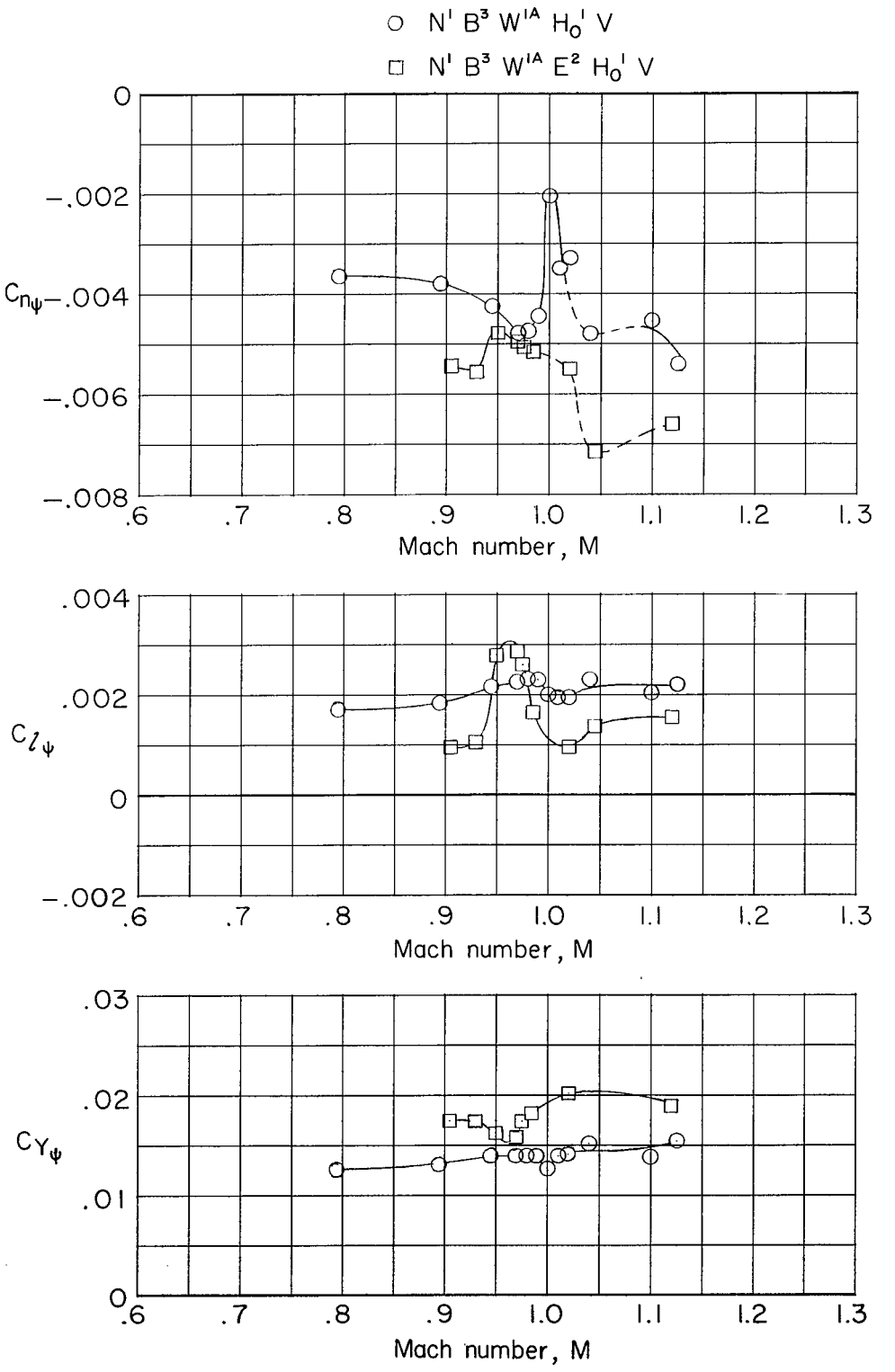


Figure 29.- Effect of large end plates located on wing tips on lateral-stability derivatives. Complete model. $\psi \approx 0^\circ$; $\alpha = -0.2^\circ$.

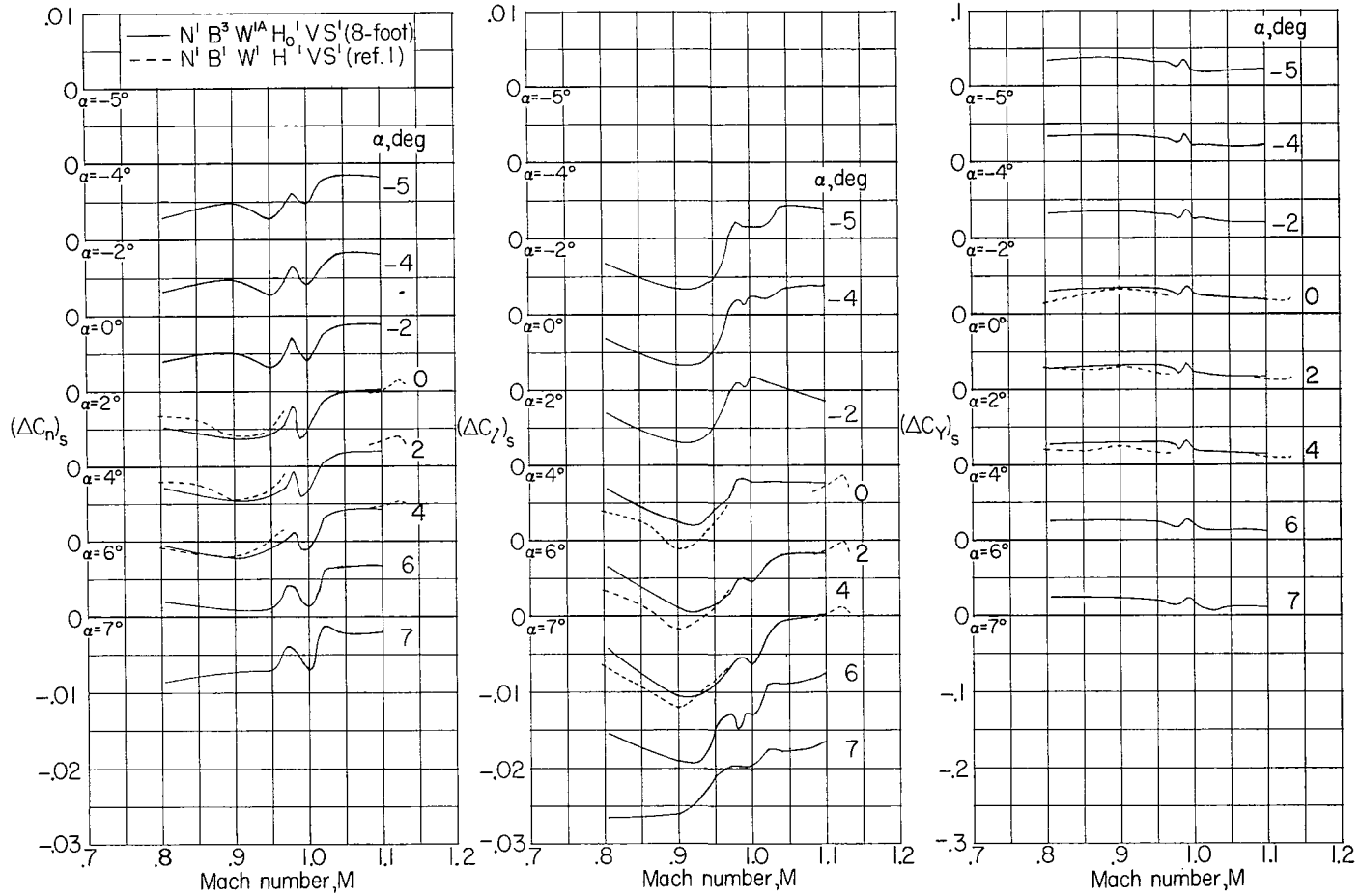


(a) Incremental yawing-moment, rolling-moment, and lateral-force coefficients.

Figure 30.- Variation with Mach number of incremental force and moment coefficients due to spoiler deflection. Spoiler mounted on upper surface of left semispan of wing. Complete model; $\psi = 0^{\circ}$.

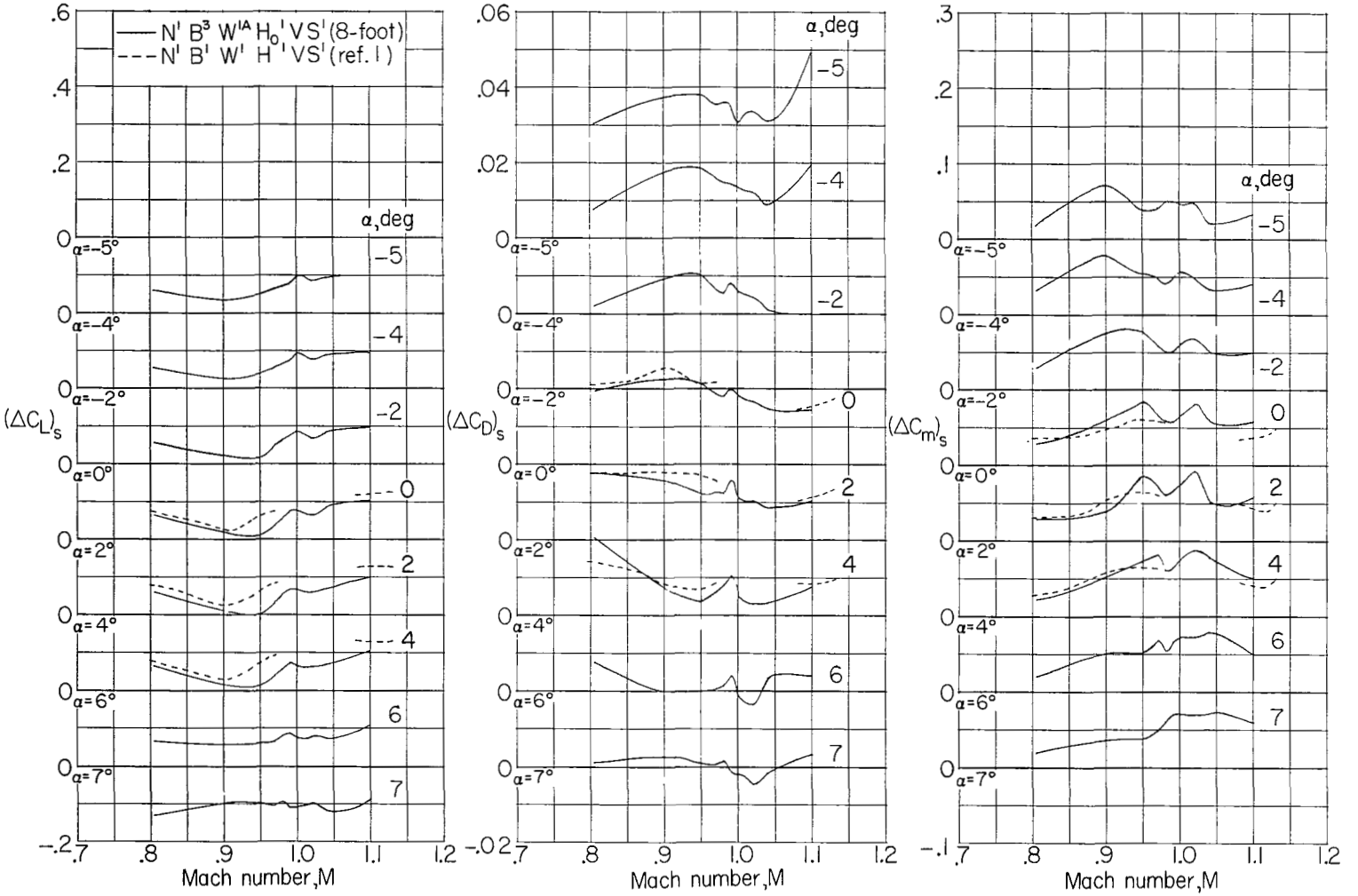


(b) Incremental lift, drag, and pitching-moment coefficients.

Figure 30.- Concluded.

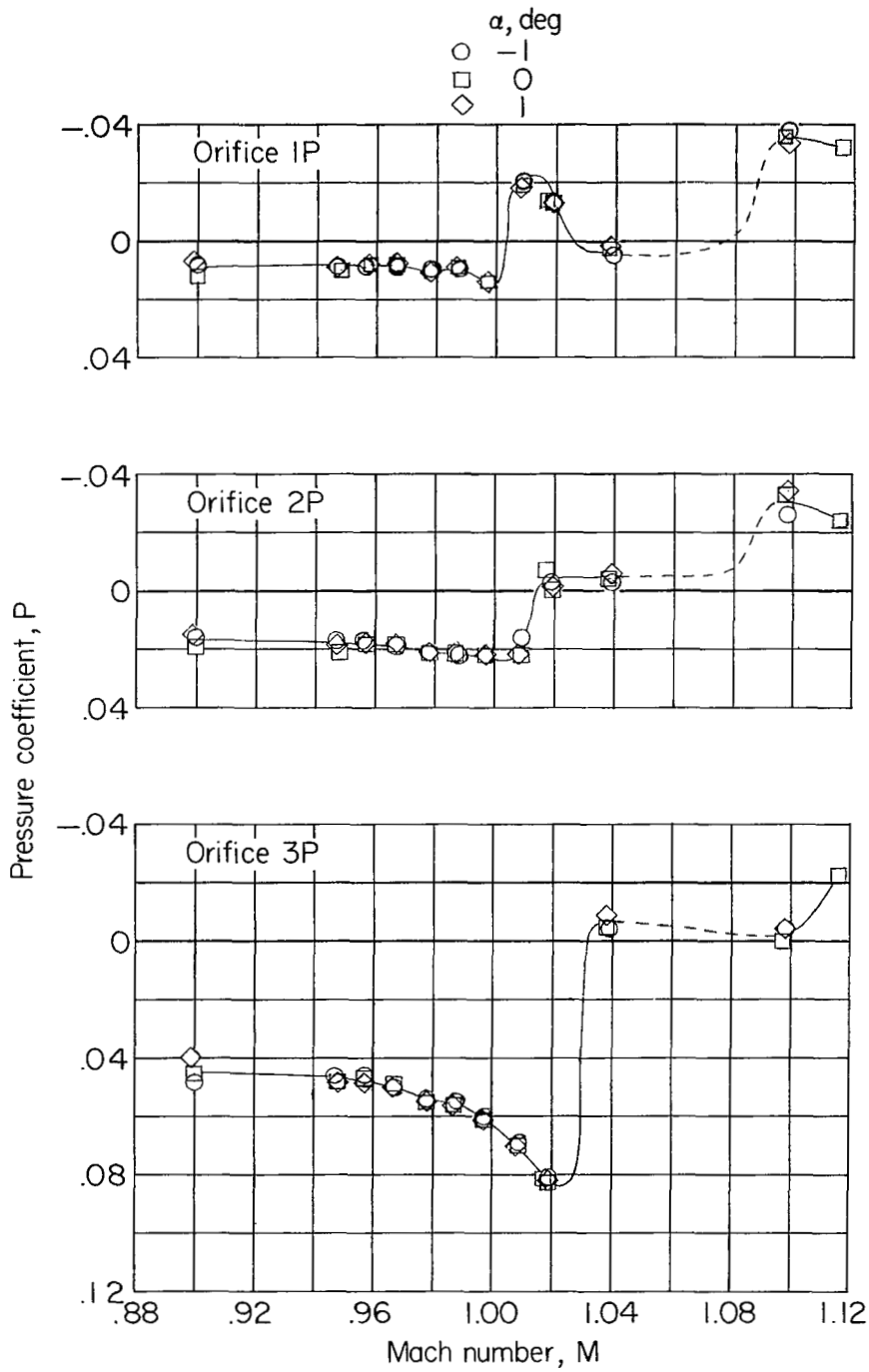


(a) Orifices 1P, 2P, and 3P.

Figure 31.- Variation of pressure coefficient with Mach number for various pressure orifices on static tube and fuselage (see fig. 5 for location of orifices). Complete model less tail, less control-cable housing, and plus static tube $\left(N^3B^2W^{1A}\right)$. $\psi = 0^\circ$.

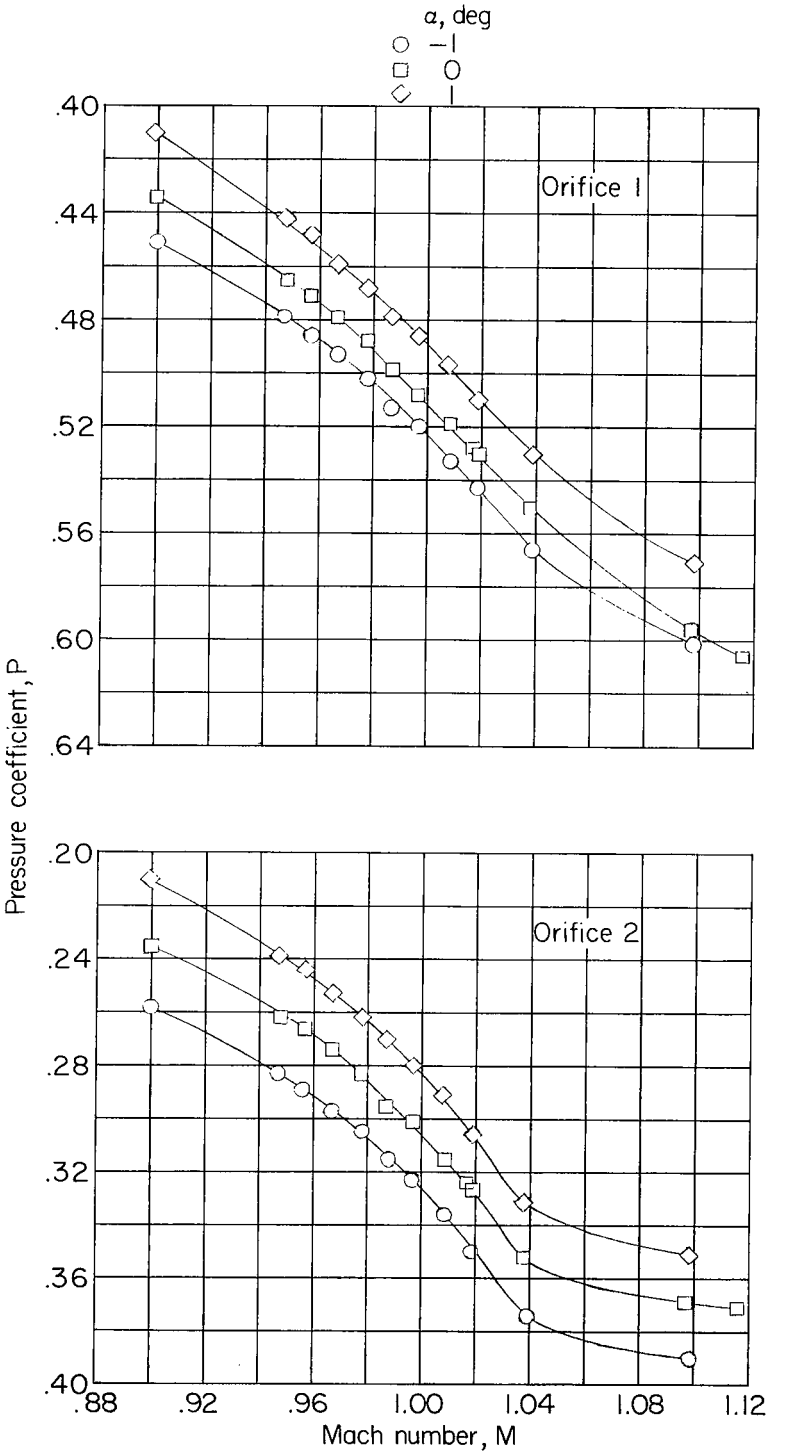


(b) Orifices 1 and 2.

Figure 31.- Continued.

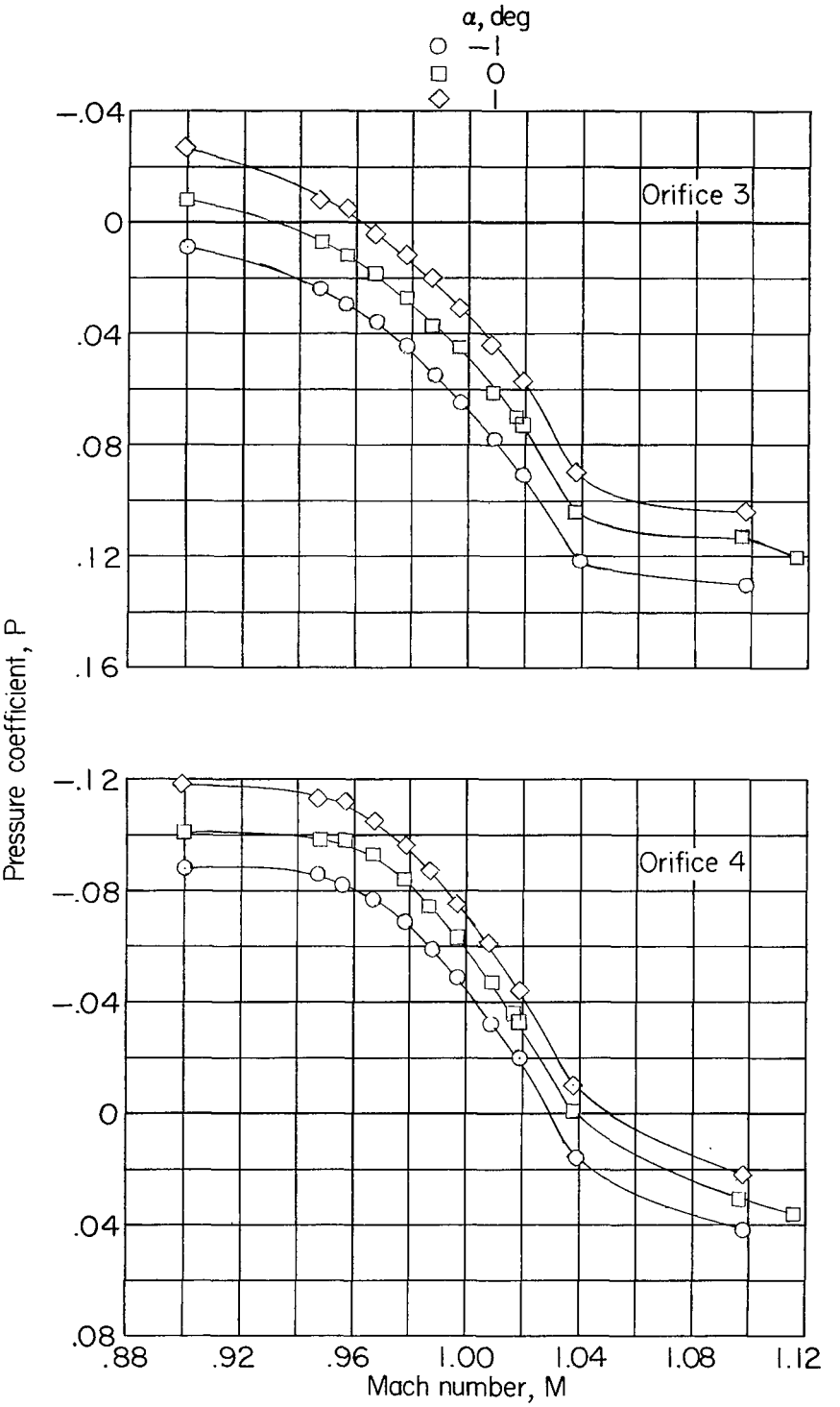


(c) Orifices 3 and 4.

Figure 31.- Continued.

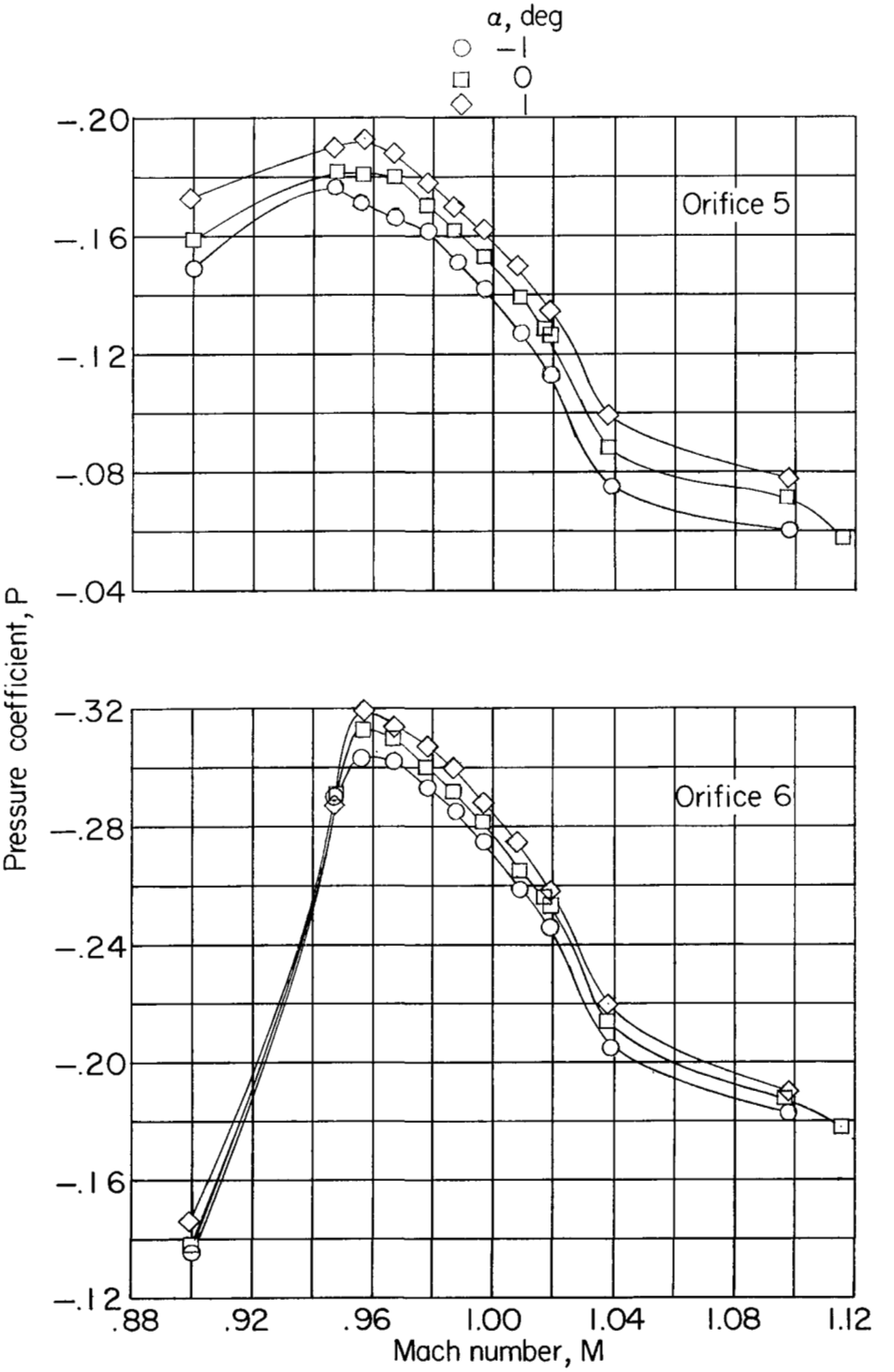


(d) Orifices 5 and 6.

Figure 31.- Continued.

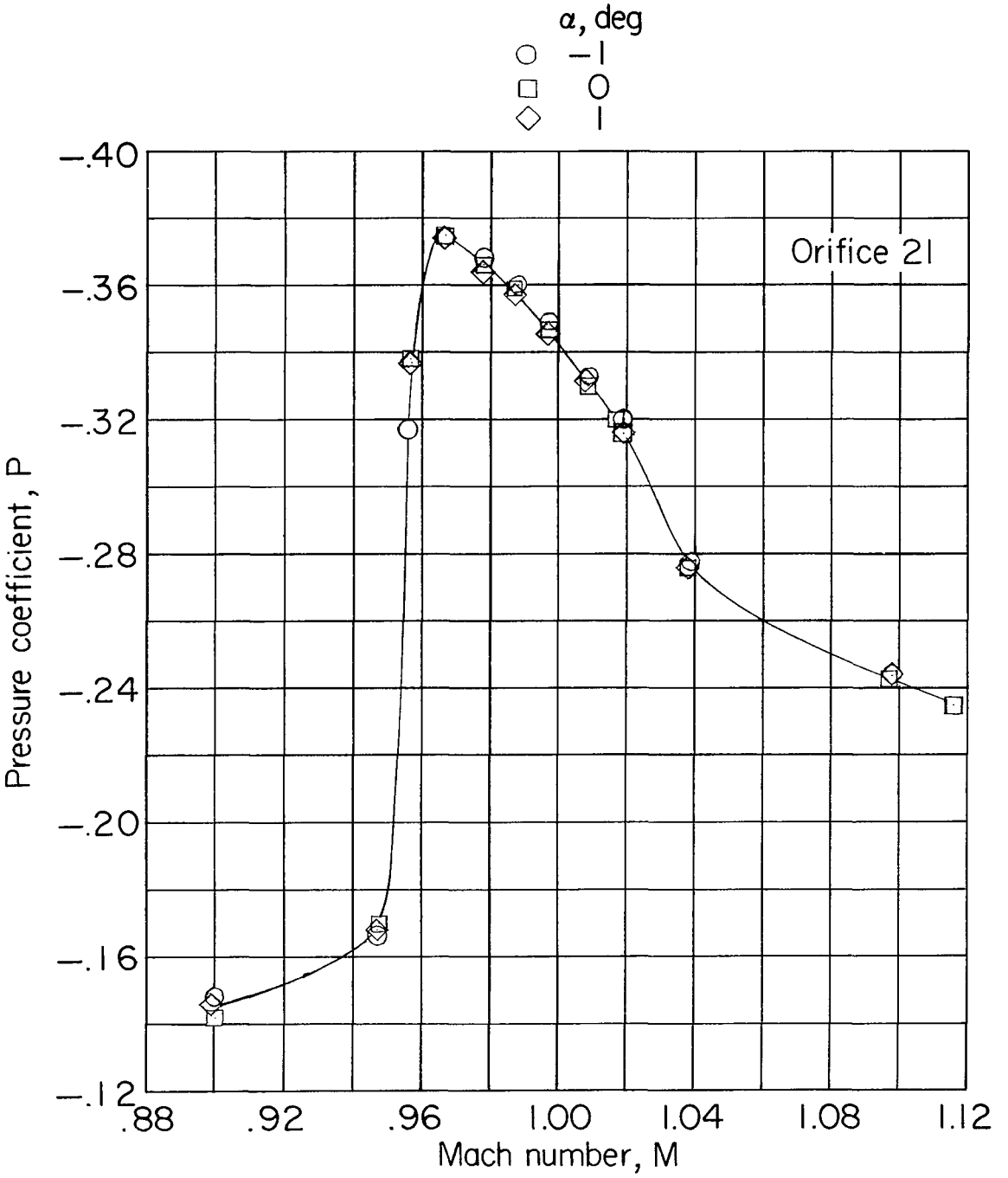


(e) Orifice 21.

Figure 31.- Continued.

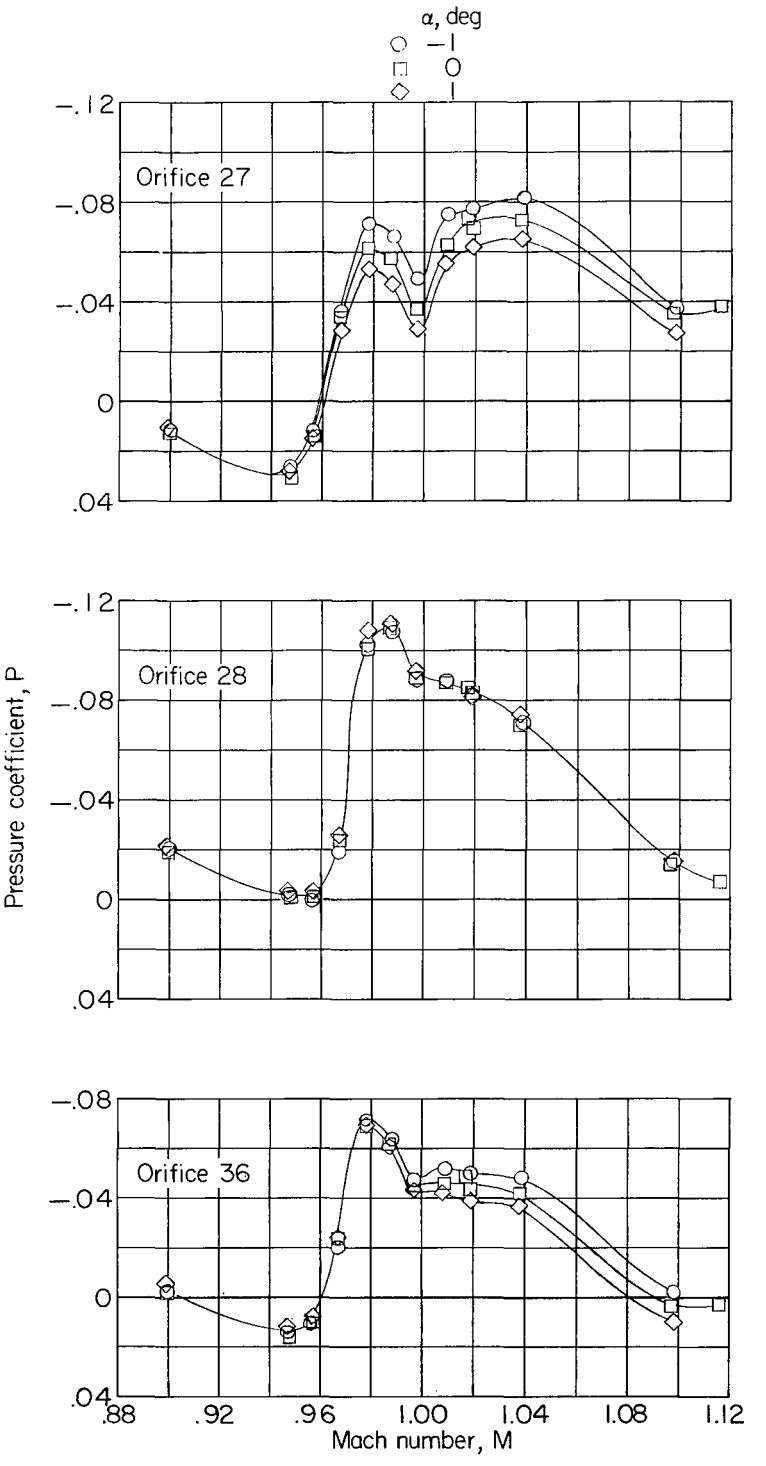


(f) Orifices 27, 28, and 36.

Figure 31.- Concluded.

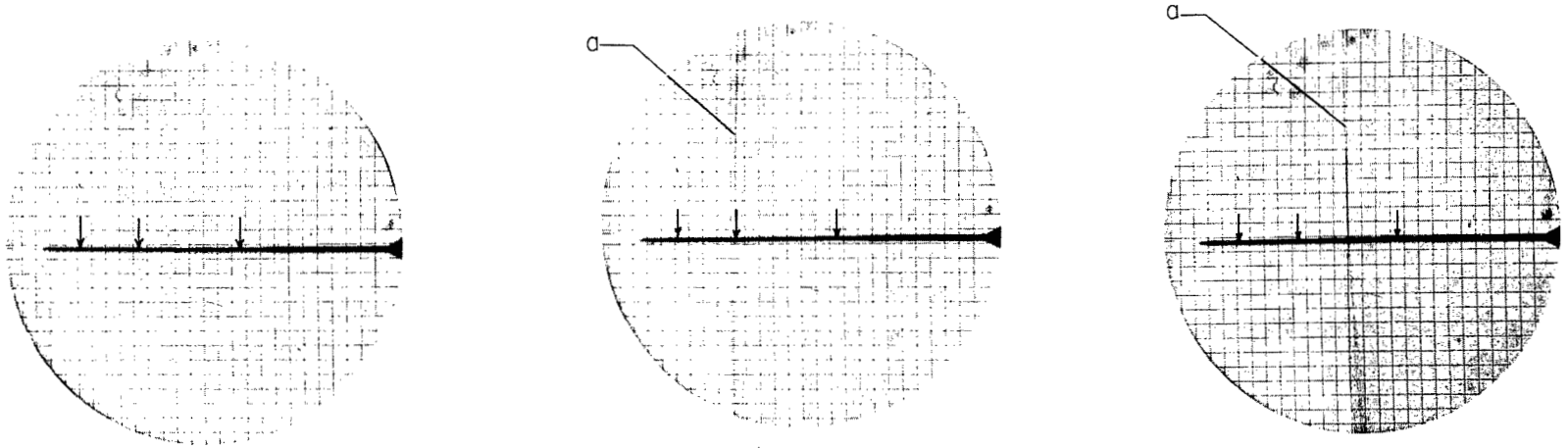


(a) M = 1.00, 1.01, and 1.02.

Figure 32.- Shock formations at transonic speeds in region of static tube. Complete model less tail, less control-cable housing, and plus static tube $\left(N^{3}B^{2}W^{1A}\right)$; $\psi = 0^{\circ}$; $\alpha = 0^{\circ}$. Arrow heads on photographs indicate longitudinal location of static orifices on static tube.

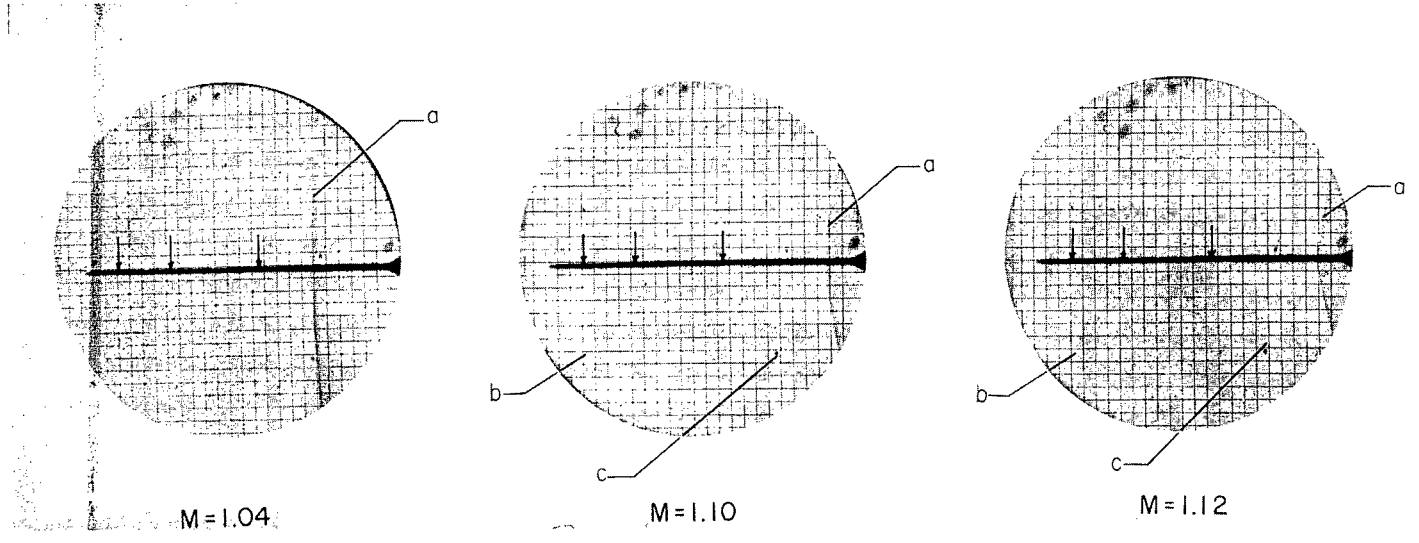


(b) M = 1.04, 1.10, and 1.12.

Figure 32.- Concluded.

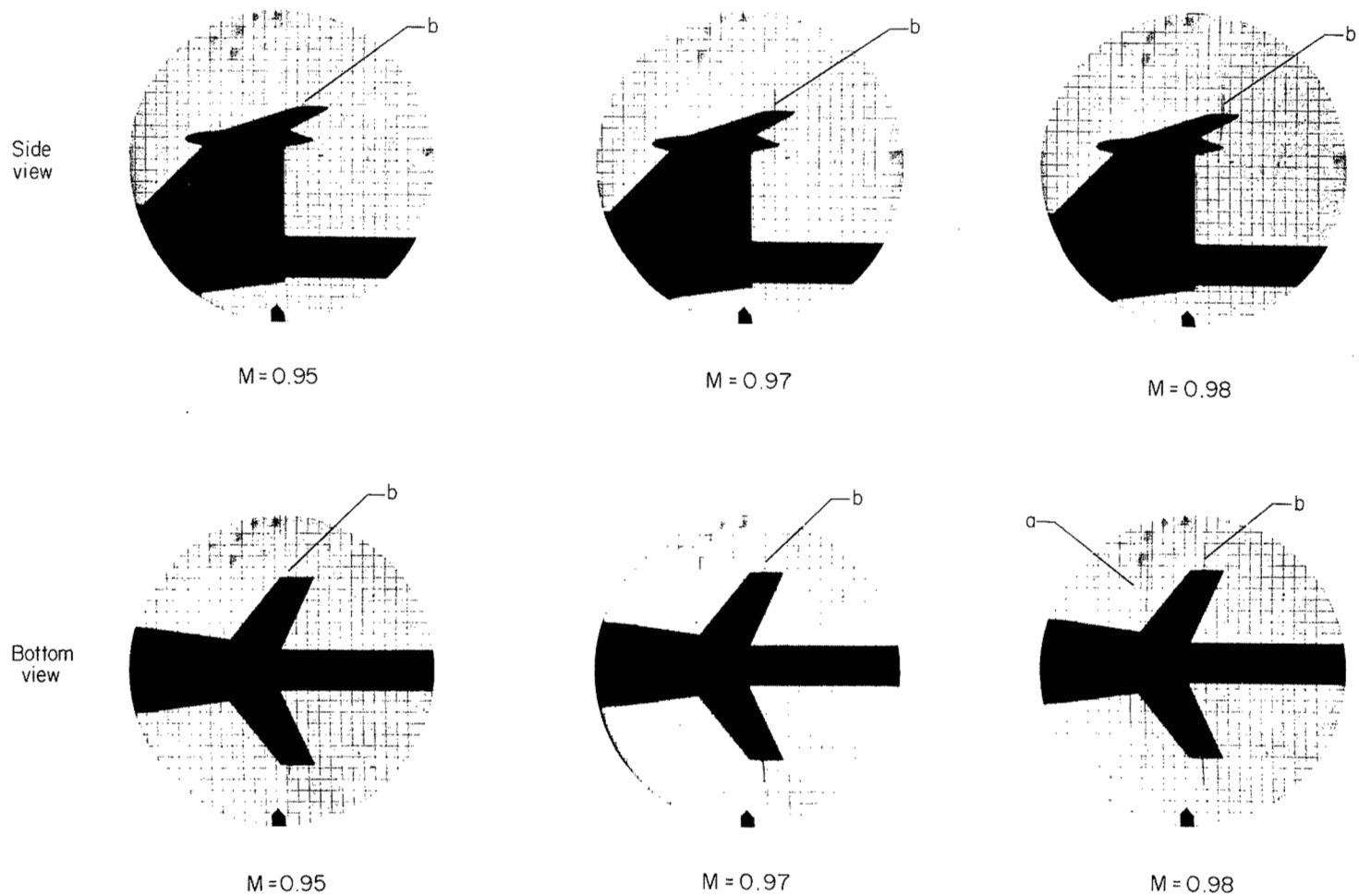


(a) M = 0.95, 0.97, and 0.98.

Figure 33.- Shock formations at transonic speeds in region of model tail. Complete model $\left(N^{1}B^{3}W^{1A}H_{o}{}^{1}V\right)$. $\psi \approx 0^{o}$; $\alpha \approx 0^{o}$ except as noted.

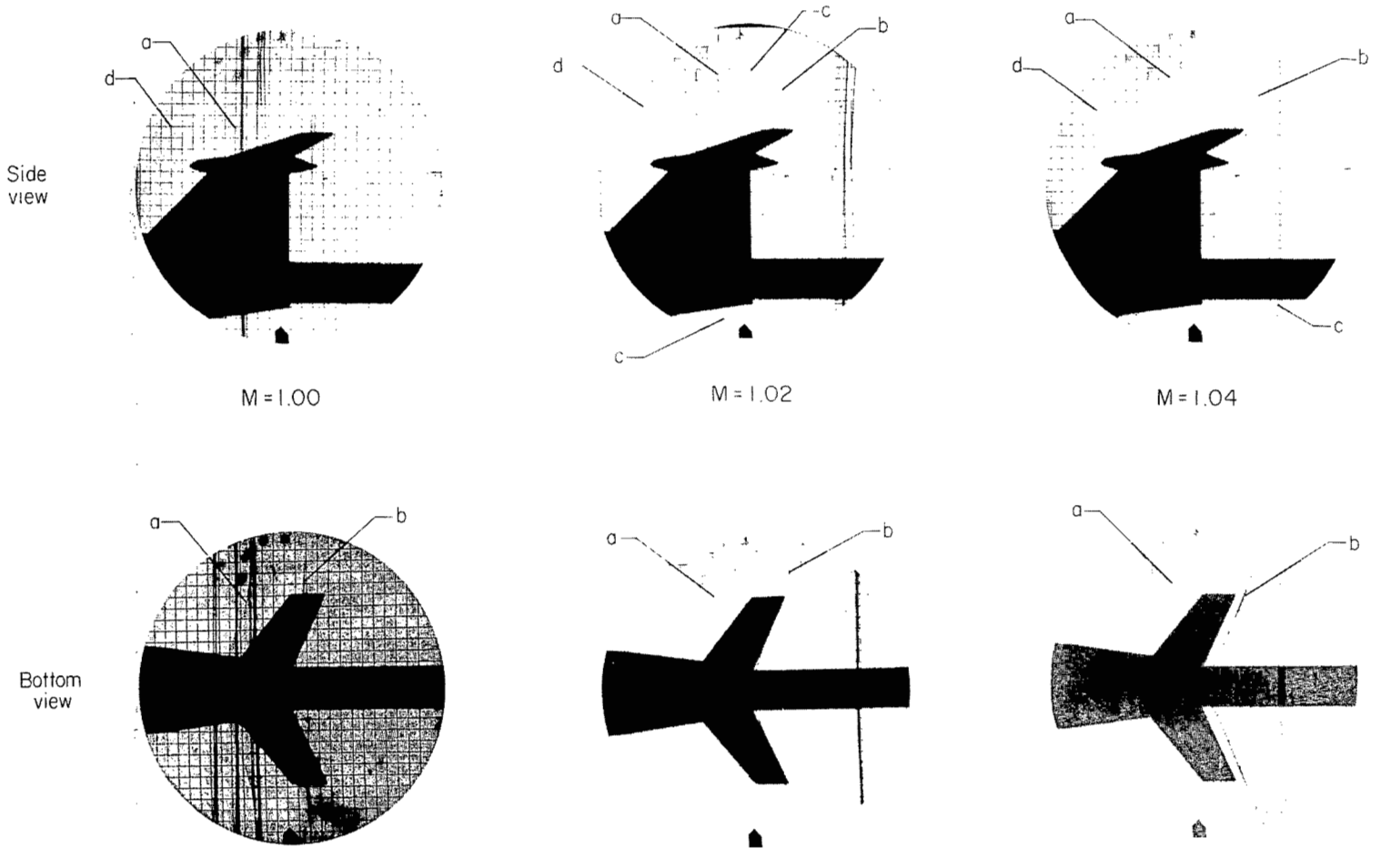


(b) M = 1.00, 1.02, and 1.04.

Figure 33.- Continued.

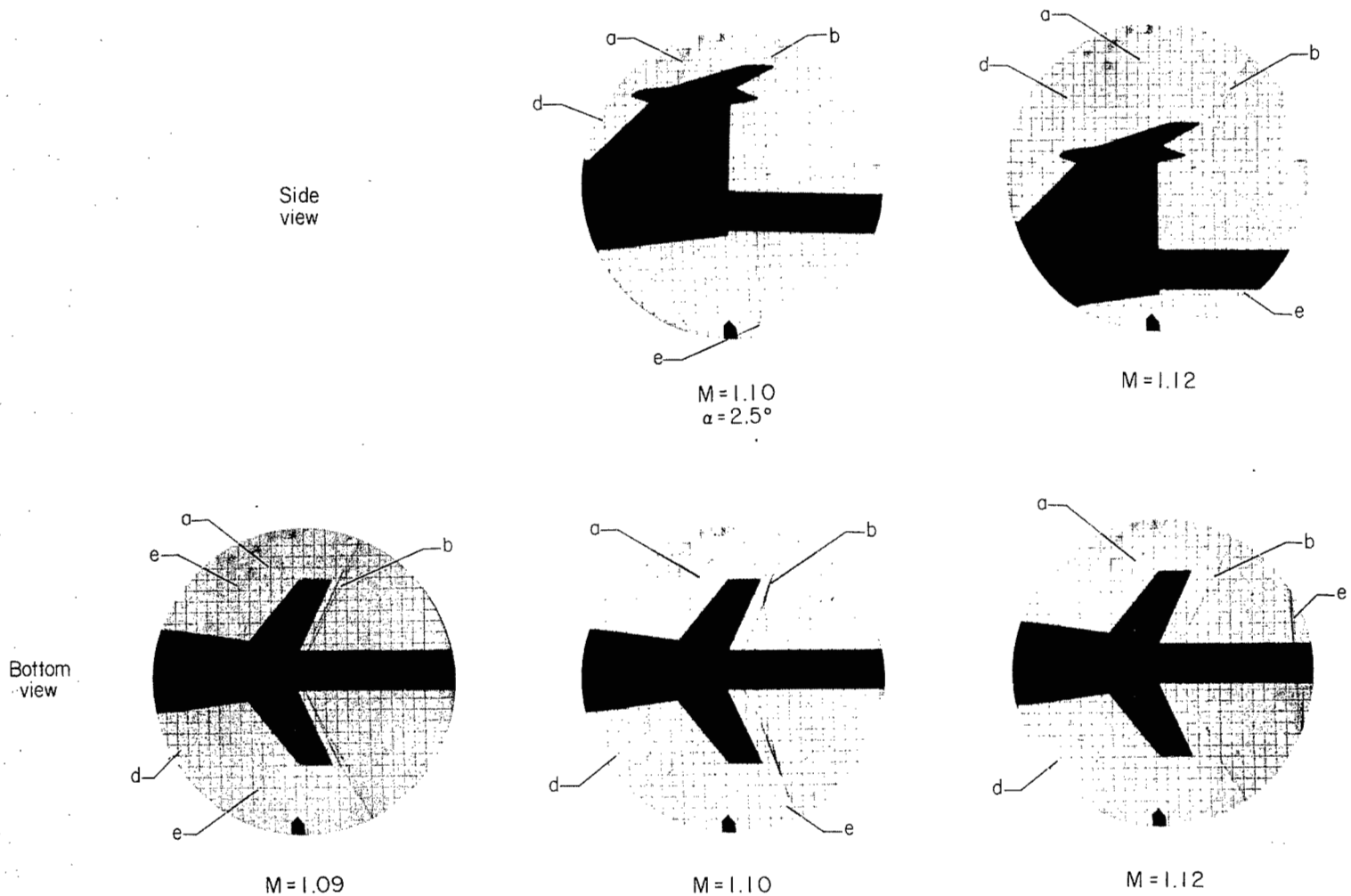


(c) M = 1.09, 1.10, and 1.12.

Figure 33.- Concluded.